4D **Dynamic Contrast-Enhanced Breast CT:** System Optimization and Quantitative Validation

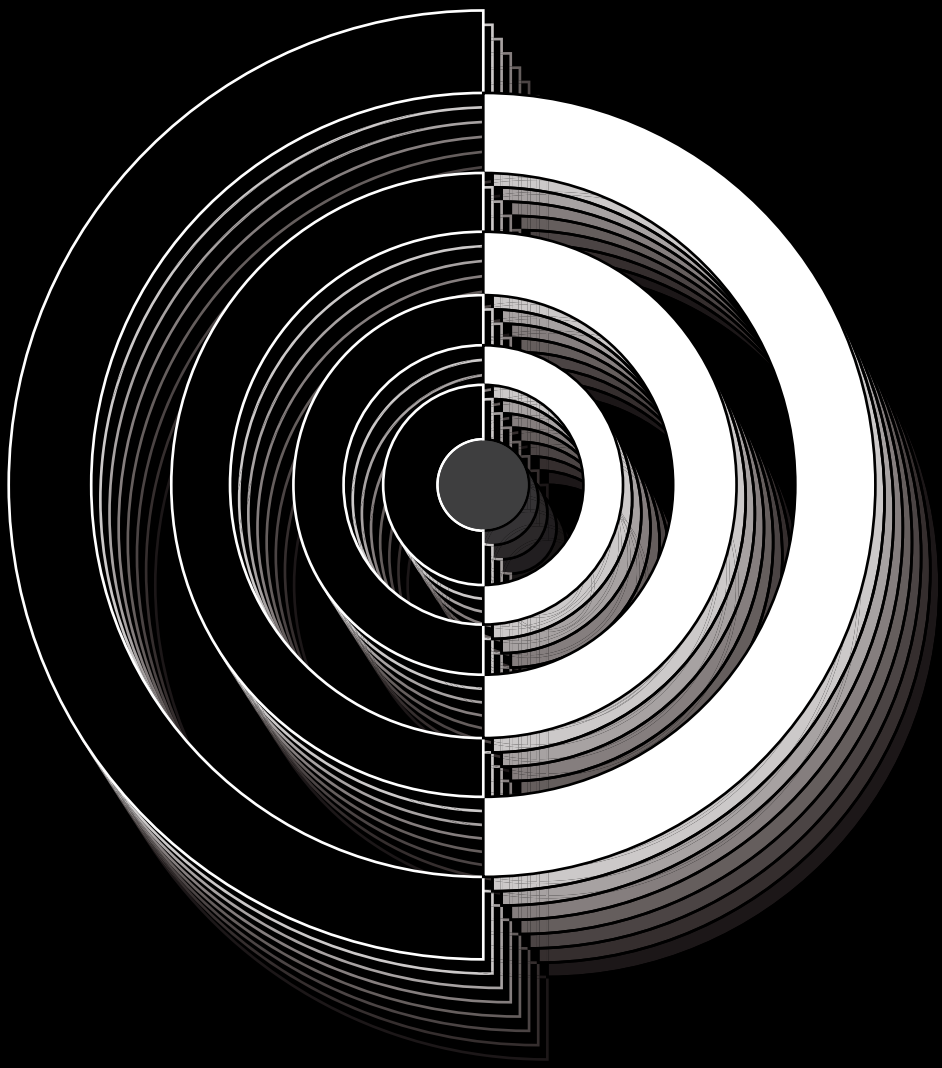

JUAN JOSÉ PAUTASSO

RADBOUD UNIVERSITY PRESS

Radboud Dissertation Series

4D **Dynamic Contrast-Enhanced Breast CT:** System Optimization and Quantitative Validation

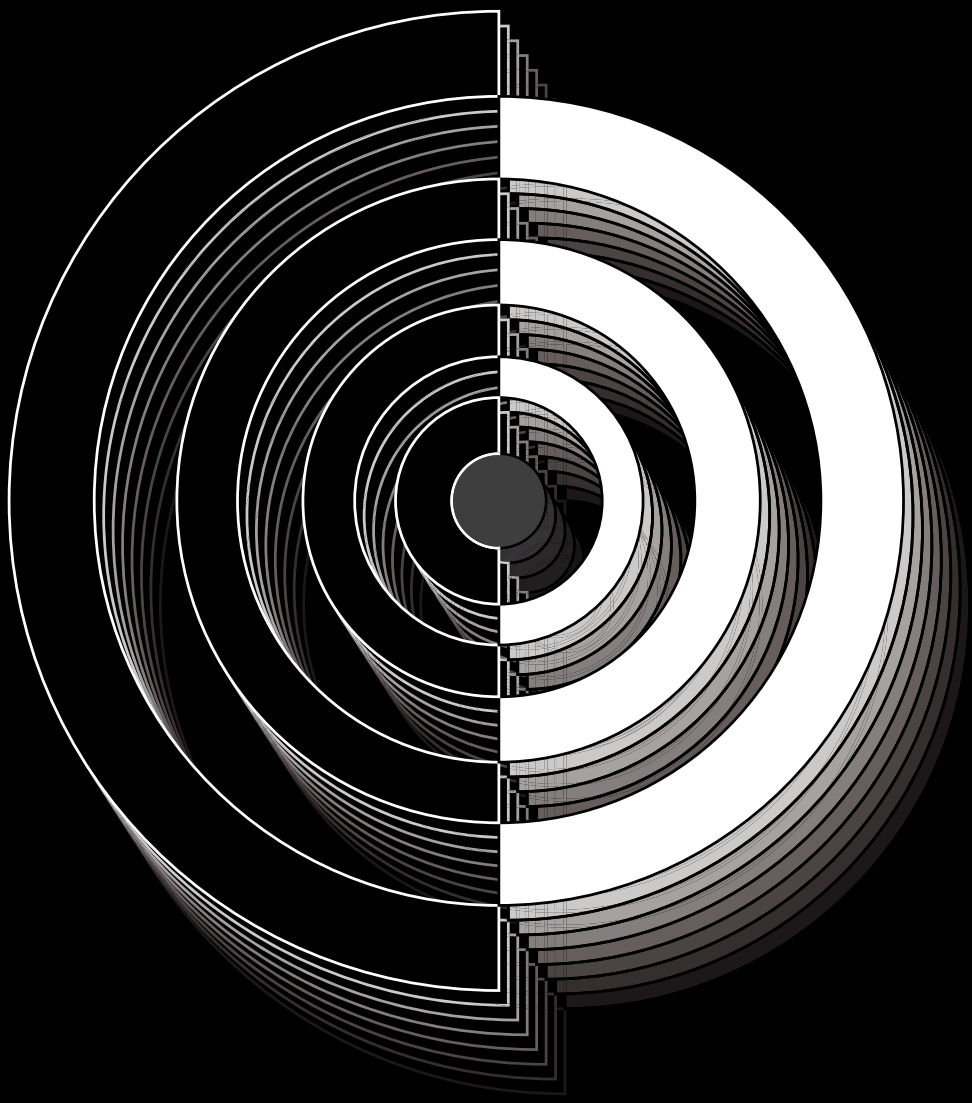

JUAN JOSÉ PAUTASSO

4D Dynamic Contrast-Enhanced Breast CT: System Optimization and Quantitative Validation
Juan José Pautasso

Radboud Dissertation Series
ISSN: 2950-2772 (Online); 2950-2780 (Print)

Published by RADBOUD UNIVERSITY PRESS
Postbus 9100, 6500 HA Nijmegen, The Netherlands
www.radbouduniversitypress.nl

Design: Proefschrift AIO | Annelies Lips
Cover: Jazmín Pautasso
Printing: DPN Rikken/Pumbo

ISBN: 9789465152356
DOI: 10.54195/9789465152356
Free download at: https://doi.org/10.54195/9789465152356

RADBOUD
UNIVERSITY
PRESS

4D Dynamic Contrast-Enhanced Breast CT

System Optimization and Quantitative Validation

Proefschrift ter verkrijging van de graad van doctor

aan de Radboud Universiteit Nijmegen

op gezag van de rector magnificus prof. dr. J.M. Sanders,

volgens besluit van het college voor promoties

in het openbaar te verdedigen op

maandag 18 mei 2026

om 10.30 uur precies

door

Juan José Pautasso

geboren op 29 juli 1992

te San Basilio, Argentinië

Promotoren:
Prof. dr. I. Sechopoulos
Dr. R.M. Mann

Copromotor:
Dr. K.J.M. Michielsen

Manuscriptcommissie:
Prof. dr. G.J.S. Litjens
Prof. dr. S. Zackrisson (Lunds Universitet, Zweden)
Dr. O. Díaz Montesdeoca (Universitat de Barcelona, Spanje)

4D Dynamic Contrast-Enhanced Breast CT

System Optimization and Quantitative Validation

Dissertation to obtain the degree of doctor

from Radboud University Nijmegen

on the authority of the Rector Magnificus prof. dr. J.M. Sanders,

according to the decision of the Doctorate Board

to be defended in public on

Monday, May 18, 2026

at 10.30 am

by

Juan José Pautasso

born on July 29, 1992

in San Basilio, Argentina

Supervisors:
Prof. dr. I. Sechopoulos
Dr. R.M. Mann

Co-supervisor:
Dr. K.J.M. Michielsen

Manuscript Committee:
Prof. dr. G.J.S. Litjens
Prof. dr. S. Zackrisson (Lund University, Sweden)
Dr. O. Díaz Montesdeoca (University of Barcelona, Spain)

"Y como no estás experimentado en las cosas del mundo, todas las cosas que tienen algo de dificultad te parecen imposibles; pero andará el tiempo, como otra vez he dicho, y yo te contaré algunas de las que allá abajo he visto, que te harán creer las que aquí he contado..."
Miguel de Cervantes, *Don Quijote de la Mancha*.

To all those who gave me an opportunity.
Thank you for believing in me and inspiring me to grow.
Your kindness and faith have shaped my journey.

Table of Contents

1 General Introduction

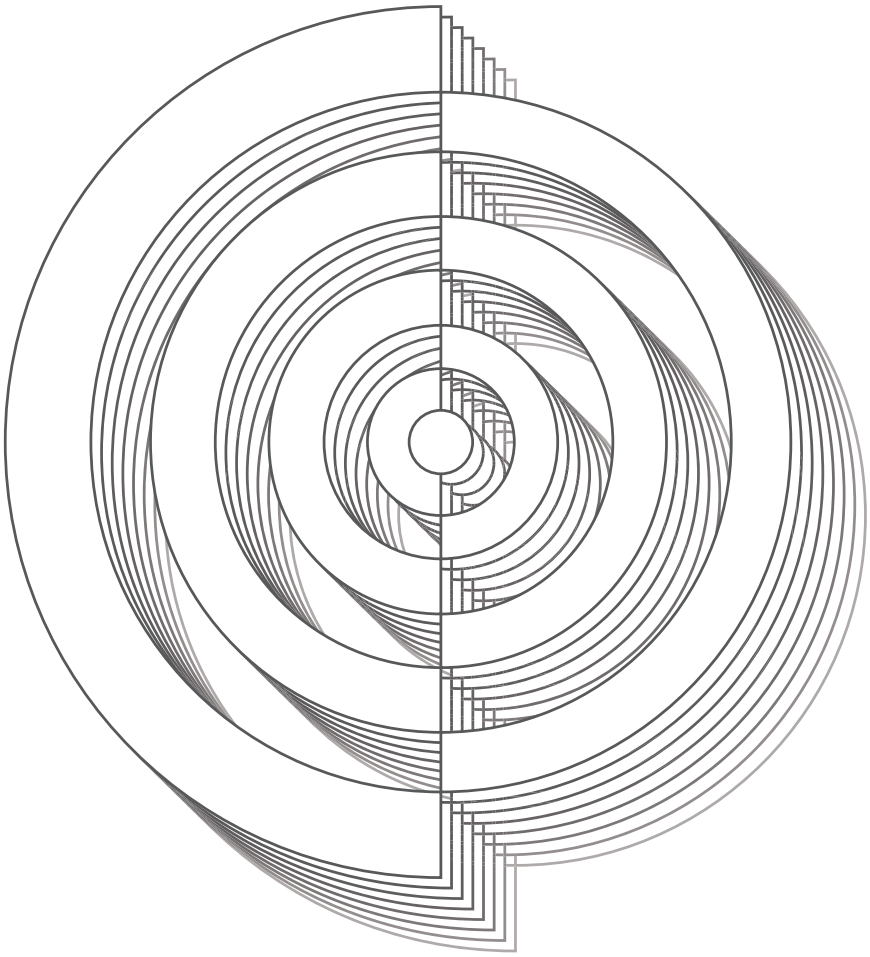

Breast Cancer: A Global Health Challenge

Breast cancer remains one of the most pressing global health challenges, affecting millions of women annually and ranking as the leading cause of cancer-related deaths among women worldwide. According to the GLOBOCAN 2022 report, there were approximately 2.3 million new cases of breast cancer diagnosed around the world, accounting for 11.6% of all cancer cases globally, with over 666,000 deaths, representing 6.9% of all cancer deaths worldwide.[1] By 2040, this burden is projected to rise substantially, with over 3 million new cases and 1 million deaths annually.[2]

This persistently high mortality rate underscores the need for improved imaging techniques that can more accurately assess treatment response, support clinical decision-making, and ultimately improve patient outcomes.

Medical Imaging in Breast Cancer

Medical imaging plays a central role in breast cancer screening and diagnosis, significantly impacting patient outcomes. The main imaging modalities, including mammography, digital breast tomosynthesis (DBT), ultrasound, and magnetic resonance imaging (MRI), each have distinct benefits and limitations.

Mammography, the cornerstone of screening, is a 2D x-ray projection imaging technique that is effective for average-risk women but struggles with early cancer detection in those with dense breast tissue.[3,4]

DBT, which provides pseudo-3D imaging, reduces the issue of overlapping structures seen in traditional mammography, improving detection rates while reducing follow-up imaging needs.[5-9] However, while some studies report clear benefits of DBT in breast cancer detection rates,[10-12] other evidence suggests minimal advantages, and concerns remain about overdiagnosis.[13,14] Moreover, findings on the impact of DBT on interval cancer rates continue to be inconsistent.[15-17]

Ultrasound, which uses sound waves to visualize tissue structures in 2D, complements mammography by enhancing sensitivity for detecting early breast masses, particularly in dense tissue.[18-22] While it improves detection, its use alongside mammography has significantly increased the number of false positives.[23,24]

MRI, unlike the previously mentioned modalities, provides high-sensitivity functional imaging, making it particularly valuable for diagnosing and staging breast cancer in high-risk patients.[25-27] Its strength lies in enhancing lesion detectability and assessing tumor vascularity through contrast dynamics. While its diagnostic benefits are well established, challenges remain, including the requirement for intravenous contrast administration, which is a major drawback, high costs and modest specificity, which increases the likelihood of unnecessary follow-ups.[28-30] Efforts to reduce costs through abbreviated protocols show promise,[31] yet MRI's role in routine screening remains limited to specific groups.[32]

Motivation for the Research

For staging and treatment planning, MRI is considered the gold standard. It is especially valuable for patients undergoing neoadjuvant chemotherapy (NAC), where it helps assess treatment response and residual disease.[33-35] Dynamic contrast-enhanced MRI (DCE-MRI) provides detailed insights into tumor shrinkage, vascular changes, and treatment response. Its high sensitivity in detecting residual disease aids clinical decision-making and helps determine the feasibility of breast-conserving therapy.[36]

Regular follow-up MRI during NAC can provide valuable insight into tumor evolution and treatment effectiveness. Although changes to the chemotherapy regimen are not routinely made based on mid-treatment imaging, MRI can help identify clear non-responders or cases of progressive disease. In such situations, reconsideration of the treatment plan may be warranted,[25] enabling timely interventions that could prevent overtreatment in good responders and avoiding delays in seeking alternatives in non-responders.[36]

However, despite its advantages, MRI has limitations that are particularly relevant for treatment monitoring. These include lower spatial resolution compared to mammography and limited temporal resolution for tracking contrast uptake. Additionally, the lack of standardization in MRI's quantitative analysis across vendors leads to variability and challenges in correcting field inhomogeneity. Differences in hardware, software, and imaging protocols further impact reproducibility, complicating consistent follow-up assessments.[36]

These challenges highlight the need for improved imaging modalities that can more effectively characterize breast tumors, reliably track treatment response,

and minimize unnecessary surgeries while remaining cost-effective. Addressing limitations in tissue differentiation, temporal resolution, and reproducibility is key to optimizing treatment planning and improving patient outcomes.

Dedicated Breast Computed Tomography

Dedicated breast computed tomography (bCT) shows promising clinical potential, offering superior mass detection compared to mammography, though with lower sensitivity for calcifications.[37-39] Given this advantage, bCT has emerged as an alternative to overcome some of the limitations of current imaging methods, particularly beneficial for women with dense breast tissue. During scanning, the patient lies prone with one breast positioned through an opening. An x-ray source and detector rotate around the breast, capturing 360-degree images reconstructed into high-resolution slices.[40-43]

The development of bCT began in the 1970s, but early technological limitations led to its discontinuation. Interest resurged in the 2000s, driven by advancements in detectors, computing, and image reconstruction. Institutions such as the University of Rochester, Friedrich-Alexander-Universität, and University of California, Davis, have played a key role in the development of commercial bCT systems. Companies like Koning and AB-CT have subsequently obtained regulatory approval for their commercial systems. More recently, Izotropic Corp., a company licensing UC Davis-developed bCT technology, has taken further steps toward commercialization.[41]

Challenges in Breast CT

Despite its potential, bCT remains an emerging technology with challenges in accessibility, specialized training, and technical factors such as radiation scatter and dose optimization. While its radiation dose is comparable to a diagnostic mammography examination,[44-46] optimizing dose remains challenging, especially with repeated scans. Minimizing radiation exposure while maintaining image quality requires dose-reduction strategies, such as advanced reconstruction algorithms, refined imaging protocols, and optimized x-ray detectors.

Refining imaging protocols plays a key role in improving bCT's imaging performance. Spectral optimization, including tube voltage and x-ray filtration adjustments, enhances tissue differentiation and reduces noise, leading to more accurate

projection data for reconstruction. Reconstruction optimization further improves noise reduction and image sharpness while maintaining a reasonable radiation dose.

However, these optimizations are application-specific. For instance, iodine quantification requires precise material differentiation, whereas screening prioritizes high sensitivity and lower radiation dose over material-specific accuracy, necessitating different optimization strategies.

Radiation scatter also poses a challenge, as x-ray beams travel through a larger volume of breast tissue. The resulting scatter can degrade image quality and reduce diagnostic contrast. While generally manageable for diagnostic purposes, it becomes more problematic for quantitative accuracy, introducing unwanted low-frequency noise, reducing contrast, and distorting signal intensities in reconstructed images. These effects cause systematic measurement errors, making reliable and consistent quantification challenging.

Functional Imaging on Breast CT

Contrast-enhanced bCT (CE-bCT) builds on bCT by using iodine-based contrast agents to improve the visualization of tissue vascularization and lesion characterization and make it a true competitor for breast MRI. Unlike MRI, which relies on gadolinium-based agents to highlight vascular enhancement through magnetic properties, CE-bCT uses iodine, which directly increases x-ray attenuation and enables quantitative assessment of iodine concentration through a linear dose-response relationship.

By enhancing lesion visibility, CE-bCT significantly improves diagnostic accuracy and may support surgical planning. Studies have shown that CE-bCT more effectively identifies and characterizes malignant lesions, including ductal carcinoma in situ (DCIS), compared to imaging methods like mammography and unenhanced bCT.[47-49]

Temporal subtraction allows for the quantitative analysis of contrast enhancement, which can distinguish malignant from benign lesions.[50] Malignant masses typically show greater enhancement, and this quantitative approach improves diagnostic accuracy by enabling more precise lesion characterization based on size, shape, margins, and internal enhancement patterns.[51] Features such as irregular shape, spiculated margins, and heterogeneous internal enhancement are strong indicators of malignancy.[52-55]

However, CE-bCT's reliance on single-acquisition protocols limits its ability to capture the dynamic temporal information of contrast uptake and washout, which are valuable for assessing tumor perfusion and vascularity.[56] To address this, 4D dynamic contrast-enhanced bCT (4D DCE-bCT) has been proposed. By incorporating a temporal dimension, 4D DCE-bCT enables detailed analysis of iodine uptake and washout rates, providing insights into tumor vascular characteristics. Additionally, faster imaging improves spatio-temporal resolution, while the linear relationship between x-ray attenuation and iodine concentration facilitates contrast quantification.[57]

4D DCE-bCT was initially introduced as a simulation pipeline to explore its feasibility and potential for capturing temporal contrast dynamics. Building on this foundation, this thesis focuses on key technical limitations and advances the modality towards experimental clinical application, supporting its potential as a personalized, cost-effective imaging approach for breast cancer care.

Thesis Outline

This thesis addresses the challenges of optimizing and validating 4D DCE-bCT to help bring the concept into practical application. Its primary goals are to improve imaging performance, optimize reconstruction parameters, and evaluate the modality's quantitative accuracy.

The technical chapters detail the contributions made in this field. *Chapter 2* focuses on developing a deep learning-based scatter correction method for bCT. Using Monte Carlo-simulated patient-based phantom data, the model estimates and corrects scatter in projection images, with validation on internal and external datasets demonstrating its effectiveness.

Chapter 3 compares first- and second-generation bCT systems, evaluating imaging quality and dose efficiency to highlight advancements and key differences.

Chapter 4 addresses spectral optimization and second-generation system characterization. A parallel-cascaded model is developed to optimize parameters such as tube voltage and x-ray filtration to enhance iodine signal detection. Experimental validation demonstrates the model's ability to optimize projection data quality, which is crucial for accurate reconstruction.

Expanding on the findings of the previous chapter, *Chapter 5* focuses on optimizing reconstruction parameters for 4D DCE-bCT to achieve high spatio-temporal resolution during dynamic contrast-enhanced scans while maintaining a reasonable radiation dose. The reconstruction method employed in this work is derived from another PhD thesis in our lab, titled *Reconstruction for four-dimensional dynamic contrast-enhanced dedicated breast computed tomography (4D DCE-bCT)*. These refinements significantly enhance the modality's ability to detect subtle changes in contrast uptake, improving its diagnostic potential.

In *Chapter 6*, quantitative accuracy is evaluated through phantom-based experiments using a custom-designed breast phantom with controlled iodine perfusion. These experiments validate the system's accuracy in measuring iodine concentrations during wash-in and wash-out phases, with the aim of ensuring the reliability of reconstructed data for clinical use.

The thesis concludes with a *General Discussion* of the findings, their relevance, and recommendations for future research.

Funding Statement

This thesis is part of a research project that has received funding from the European Research Council (ERC) under the European Union's Horizon 2020 research and innovation programme (grant agreement No 864929).

2 AI-Based Scatter Correction in Breast CT

Original title: Deep learning for x-ray scatter correction in dedicated breast CT

Juan J. Pautasso, Marco Caballo, Mikhail Mikerov, John M. Boone, Koen Michielsen, and Ioannis Sechopoulos

Published in Medical Physics 2023; 50(4):2022-2036. https://doi.org/10.1002/mp.16185

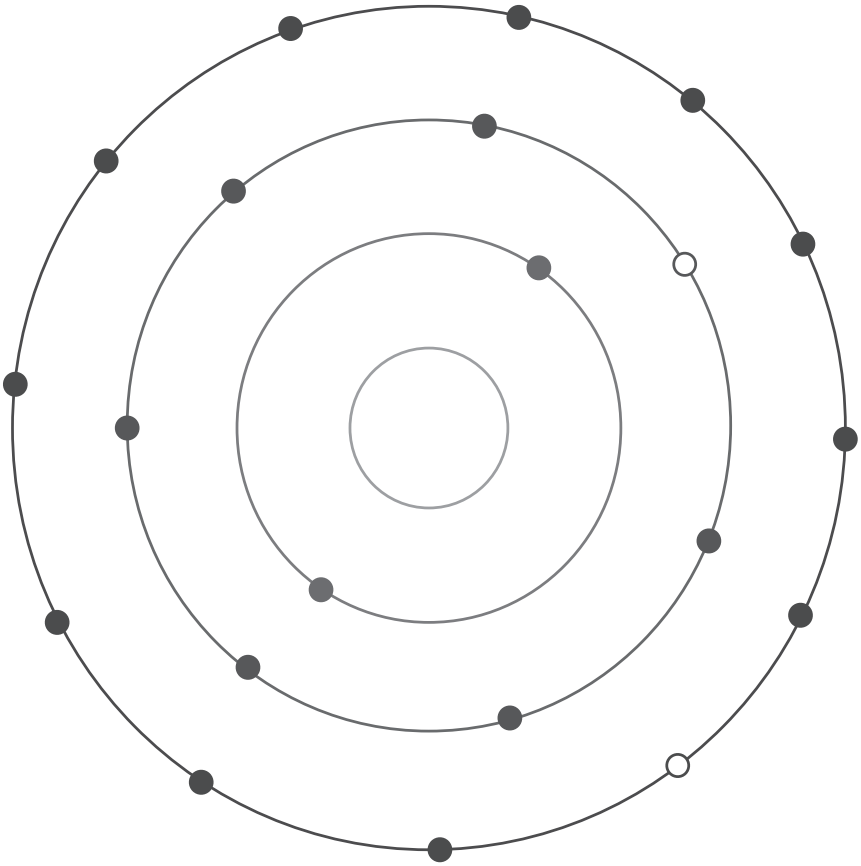

Abstract

Background

Accurate correction of x-ray scatter in dedicated breast computed tomography (bCT) imaging may result in improved visual interpretation and is crucial to achieve quantitative accuracy during image reconstruction and analysis.

Purpose

To develop a deep learning (DL) model to correct for x-ray scatter in bCT projection images.

Methods

115 patient scans acquired with a bCT clinical system were segmented into the major breast tissue types (skin, adipose, and fibroglandular tissue). The resulting breast phantoms were divided into training (n = 110) and internal validation cohort (n = 5). Training phantoms were augmented by a factor of four by random translation of the breast in the image field of view. Using a previously validated Monte Carlo (MC) simulation algorithm, 12 primary and scatter bCT projection images with a 30-degree step were generated from each phantom. For each projection, the thickness map and breast location in the field of view were also calculated.

A U-Net based DL model was developed to estimate the scatter signal based on the total input simulated image and trained single-projection-wise, with the thickness map and breast location provided as additional inputs. The model was internally validated using MC-simulated projections and tested using an external data set of 10 phantoms derived from images acquired with a different bCT system. For this purpose, the mean relative difference (MRD) and mean absolute error (MAE) were calculated. To test for accuracy in reconstructed images, a full bCT acquisition was mimicked with MC-simulations and then assessed by calculating the MAE and the structural similarity (SSIM).

Subsequently, scatter was estimated and subtracted from the bCT scans of three patients to obtain the scatter-corrected image. The scatter-corrected projections were reconstructed and compared with the uncorrected reconstructions by evaluating the correction of the cupping artifact, increase in image contrast, and contrast-to-noise ratio (CNR).

Results

The mean MRD and MAE across all cases (min, max) for the internal validation set were 0.04% (-1.1%, 1.3%) and 2.94% (2.7%, 3.2%), while for the external test set they were -0.64% (-1.6%, 0.2%) and 2.84% (2.3%, 3.5%), respectively. For MC-simulated reconstruction slices, the computed SSIM was 0.99 and the MAE was 0.11% (range: 0%, 0.35%) with a single outlier slice of 2.06%. For the three patient bCT reconstructed images, the correction increased the contrast by a mean of 25% (range: 20%, 30%), and reduced the cupping artifact. The mean CNR increased by 0.32 after scatter correction, which was not found to be significant (95% confidence interval: [-0.01, 0.65], p=0.059). The time required to correct the scatter in a single bCT projection was 0.2s on an NVIDIA GeForce GTX 1080 GPU.

Conclusion

The developed DL model could accurately estimate scatter in bCT projection images and could enhance contrast and correct for cupping artifact in reconstructed patient images without significantly affecting the CNR. The time required for correction would allow its use in daily clinical practice, and the reported accuracy will potentially allow quantitative reconstructions.

1 Introduction

When not addressed, x-ray scatter can be one of the main causes of degradation of image quality in x-ray imaging. For example, in tomographic imaging, it can be observed as a cupping artifact that affects the accuracy of the measured signal intensity. Its consequences are even more noticeable in cone beam computed tomography (CBCT), due to the large area of irradiation.[58-60] X-ray scatter not only results in a potentially suboptimal visual interpretation by radiologists, but also in quantitative inaccuracies that can affect image analysis.

Different methods have been proposed to correct the x-ray scatter signal in acquired images. In general, these can be divided into two groups: scatter suppression and scatter estimation.[61] In body CBCT, the former combines the use of an anti-scatter grid or collimation with software post-processing;[62-65] the latter consists of post-processing approaches that aim to estimate the scatter, and then correct the images by subtraction.[66-70]

The gold standard for scatter estimation is Monte Carlo (MC) simulation.[59] However, although it can provide accurate estimates, its disadvantage lies in the time required to obtain such results, which hinders its application in clinical practice.[61] For this reason, to estimate the scatter in body CBCT images, algorithms based on deep learning (DL) trained with MC-simulated patient data have been developed.[61,71-74]

In breast imaging, dedicated breast computed tomography (bCT)[42,44,45,75] is not exempt from the effect of scatter.[76-78] In this modality, typically based on a CBCT system, the patient lies prone on a table with an opening through which the breast is placed. The x-ray tube and the detector are mounted on a rotating gantry, and a complete set of projections is obtained in a single revolution around the pendant breast. These projections are then reconstructed to obtain a 3D image capable of providing information about the anatomy of the breast and the presence of lesions, optionally with iodine contrast enhancement.[47,48,57,79]

As with body CBCT, several approaches have been proposed to avoid the undesirable effects of x-ray scatter in bCT. Most of them suppress the scatter signal by using anti-scatter grids or collimation, also combined with software postprocessing.[80-82] Moreover, solutions were also proposed in which specific hardware was developed and integrated into the bCT system to mitigate the effect of x-ray scatter.[83-85] Similarly, fully software-based solutions were also proposed to correct for scatter in bCT images.[86,87]

However, most previous methods developed to correct for the scatter signal in bCT either required the acquisition of an additional scan with an x-ray beam blocker (resulting in the need for additional hardware and yielding an increased dose and possibility of motion artifacts),[87] or they assumed the prior knowledge of breast shape and tissue composition, possibly leading to simplifications that may affect the accuracy of scatter estimation.[86]

Therefore, in this work we propose and validate a software-based solution to estimate and correct the x-ray scatter present in bCT images. The developed method consists of a DL model for scatter estimation trained on MC-simulated primary and scatter bCT projections performed using patient-based breast phantoms. The method is devised to estimate the scatter directly from the input bCT projection image, which is then subtracted from the acquired projection, resulting in the desired correction.

2 Materials and methods

2.1 Patient-based phantom generation

A total of 115 previously-created patient-based phantoms[88,89] were used in this work. These were obtained from patient scans acquired with a clinical Koning breast CT (Koning Corp., Norcross, GA, USA) installed at Radboud University Medical Center, which were automatically segmented into the main tissues present in the breast: adipose tissue, fibroglandular tissue, and skin. The x-ray tube with a tungsten anode was set to 49 kV. An aluminum filter of 1.6 mm (1.39 mm Al 1st HVL) was used. Dose was set by the system automatic exposure control.

Due to the artifacts inherent to the modality that made the inclusion of information from the chest wall unfeasible during segmentation,[88] a total of 15 rows in which the pectoralis muscle was present had to be removed. However, a simplified version of the chest wall was added back during the MC simulations. To make sure that the phantom dimensions and location in the field of view matched the original patient scans, we compensated for this missing part by adding 15 slices (thickness per slice 0.273 mm) of homogeneous tissue, with each slice consisting of a dilation of the preceding slice. Since no information about the tissue type present in this region was available, this homogeneous breast tissue was modelled as a mixture of 80% adipose and 20% fibroglandular tissue, by mass. The added tissue ensures that the resulting scatter estimate from the MC simulations is correct, including any backscatter onto the detector from the patient's chest. This extrapolated region,

unusable even uncorrected, was excluded when measuring performance. An example of a patient-based phantom is shown in Figure 2.1.

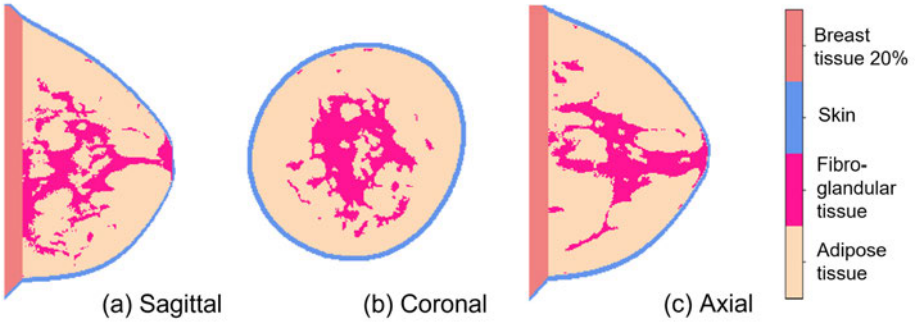

Figure 2.1: Example of a bCT patient-based phantom shown in the (a) sagittal, (b) coronal, and (c) axial views. Breast tissue 20% represents the 15 slices (4.1 mm) of added tissue near the chest wall, composed of a homogeneous mixture of 80% adipose and 20% fibroglandular tissue, by mass. This added tissue was inserted to compensate for the missing slices in the segmented breast CT phantoms, due to image artifacts in the region close to the chest wall.

To increase the number of phantoms available to train and validate the developed DL model (described in Section 2.4), the initial number of patient-based phantoms was increased fourfold by random translation and then separated to devote for either training the model (n = 440 samples) or for validation (n = 20 samples). To achieve realistic augmentations, each phantom was translated up to 40 mm in a random direction along the coronal plane, to account for different possible breast positions in the field of view.

In addition, for independent testing, a set composed of another ten previously generated patient-based phantoms was collected. For this, ten patient scans acquired with a completely different bCT system named Doheny, developed and installed at the University of California, Davis, were retrieved. The system was equipped with an x-ray tube was set at 60 kV. To filter the x-ray spectrum, a 0.2 mm copper filter (1.5mm Al 1st HVL) was used.[45] A breast phantom was generated from each of these patient scans using the same method as that used for the first 115 phantoms.[88,89]

2.2 Monte Carlo primary and scatter image simulation

The obtained samples were used to generate primary and scatter projection images using a previously-validated MC simulation algorithm based on the Geant4 toolkit (v10.07, December 2020).[90,91] All simulations were performed to replicate the

geometry and acquisition settings of the clinical bCT system installed at Radboud University Medical Center. A 49 kV spectrum filtered with 1.6 mm Al was modeled[92] to match the 1st half value layer of 1.39 mm Al previously reported.[89] For each MC simulation, 2×10^8 x-rays were tracked. This number of primary histories results in an estimated maximum uncertainty lower than 10% in MC-simulated images, based on the uncertainty estimation method proposed by *Sempau et al*.[93]

During simulation, to recreate the geometry of the bCT system, a 397 mm × 248 mm bCT indirect flat panel detector was modelled as a 600 µm thick CsI scintillator layer and a pixel size of 3.104 mm to obtain images of 128 × 80 pixels in size.

The measured distance from the source to the detector was 923 mm, while the isocenter was located at 650 mm from the source. The type of x-ray field used was isotropic.

For each simulation, two outputs were obtained: the primary projection and the scatter projection, the latter involving the photons subjected to one or more interactions before reaching the detector. For each sample, a total of 12 simulations were performed, from 0° to 360° with a 30° step, to cover a complete gantry revolution.

Consequently, a total of 5460 primary and scatter projections of size 128 × 80 pixels were generated. To obtain the images representing the total x-ray energy absorbed in the detector, primary and scatter projections were summed.

2.3 Data preprocessing and deep learning model inputs

All MC-simulated projection images were individually normalized to the 95th percentile of pixel intensity of the entire image. The DL model was trained single-projection-wise, i.e., single total projection input, single scatter projection output, to maximize the ratio between ease of learning and computational efficiency.

However, only including 2D projection images as network input would result in the lack of any information in the third dimension, which can affect the scatter magnitude and distribution. To account for this, and still maintain a single projection-wise approach, two additional parameters were calculated for each MC simulated projection and provided as extra inputs to the model. The first was the breast location, for which the horizontal distance was calculated from the breast center of mass to the center of the projection image orthogonal to the view being processed. This input addresses the effect on the scatter distribution of the breast location along the direction orthogonal to the projection being processed.

The second additional input was the breast thickness map associated with each projection image, which was obtained by reconstructing the acquired images and measuring the intersection length of the ray going from the source to each pixel of the imaged breast at the detector. This additional input provides information on the third dimension of the breast regarding its size and shape. To ease the training of the model for scatter estimation, the thickness maps were normalized to a similar range of pixel values as the original simulated projections, by applying the negative exponential thickness, as follows:

$$normalized\ thickness\ map = exp\ (-thickness\ map/100) \tag{2.1}$$

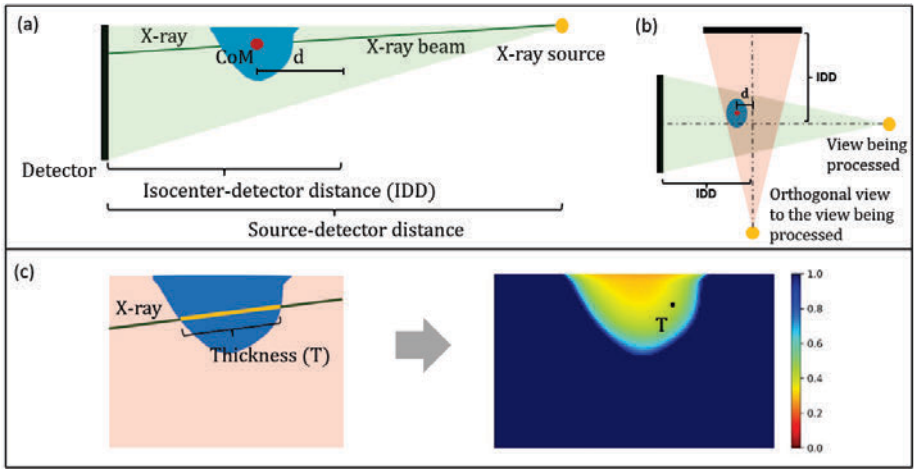

Figure 2.2: Example calculation of the two additional inputs: (a) shows a typical acquisition scenario where the source-detector and isocenter-detector distances are known. The center of mass (CoM) of the breast is at a distance d from the isocenter. The x-ray beam (light green) irradiating the breast and, as an example, a given x-ray beam (dark green line) are also shown. (b) shows how the horizontal distance from the center of mass of the breast to the center of the orthogonal projection image (x-ray beam in light red) is calculated. In addition, in (c), on the left, an example of the calculation of the intersection length of the beam from the source to one pixel of the imaged breast at the detector. The thicknesses obtained for each of the pixels of the breast imaged on the detector form the thickness map. Equation (2.1) is applied to normalize the map and the result is the image shown on the right.

Figure 2.2 shows an example for both additional inputs.

2.4 Deep learning model architecture and training parameters

A U-Net-based[94] convolutional neural network (CNN) was developed as shown in Figure 2.3. The architecture consists of a contracting path and an equally-formed expansion path. In the contracting path, the number of feature channels was

doubled at each downsampling step, with the input spatial dimensions being halved by using 2 × 2 max pooling layers. In the expansion path, the number of feature channels was doubled, as each step consists of a resampling of the feature map through 2 × 2 up-sampling layers.

The total images were set as the main input at the first block of the contraction path, while the scatter projection images were given to the network as pixelwise labels for learning.

The output of each block from the contraction path was concatenated to the corresponding up-sampling block in the expansion path. The final layer was implemented with 1 × 1 convolutions to map the channels to the desired output.

For each convolutional layer of the network, padded 2D convolutions (padding='*same*') with filter size 64, kernel size 3 × 3 and He Uniform initialization were implemented. Each convolution layer was followed by batch normalization (momentum = 0.99, epsilon = 0.001) and ReLU activation functions, except for the last layer. This layer consisted of a 2D convolutional filter with kernel size 1 × 1, and sigmoid activation. At the network bottleneck, both additional inputs (breast location and thickness map) were concatenated with the projection image features obtained from the contraction path. Specifically, the breast location was concatenated directly to the deepest network layer, as typically performed for the merging of scalar and convolutional features.[95]

The thickness map was concatenated at the same network depth, but, prior to concatenation, was further processed with an additional downsampling block, acting as a feature extractor.[94] The thickness map was concatenated at this location, instead of being given as a second channel to the original input (breast projection), to avoid replicating high-resolution features related to breast thickness from the contraction to the expansion path. Since information on breast thickness is useful only to provide extra three-dimensional information to the network, concatenating it in the network bottleneck (i.e., without replicating the thickness features between the encoder and the decoder) allows to maximize the training efficiency by making the learning of high-resolution features only from the input breast projection easier. Adam optimizer was used for training the model (batch size = 8, learning rate = 10^{-4}, 2000 epochs).

The loss function (L) consisted of a weighted mean squared error. For this, the square error was calculated by subtracting the ground truth MC-simulated image

(y) from the DL-estimated scatter image ($\hat{y}$). The loss was weighted ten times more within the breast than in the open field. The breast area was identified in each projection by global thresholding. The equation L can be written as follows:

$$L = \frac{1}{n}\sum_{i=0}^{n}\left(10 * \left(y_{breast}^{(i)} - \hat{y}_{breast}^{(i)}\right)^2 + \left(y_{open\ field}^{(i)} - \hat{y}_{open\ field}^{(i)}\right)^2\right) \quad (2.2)$$

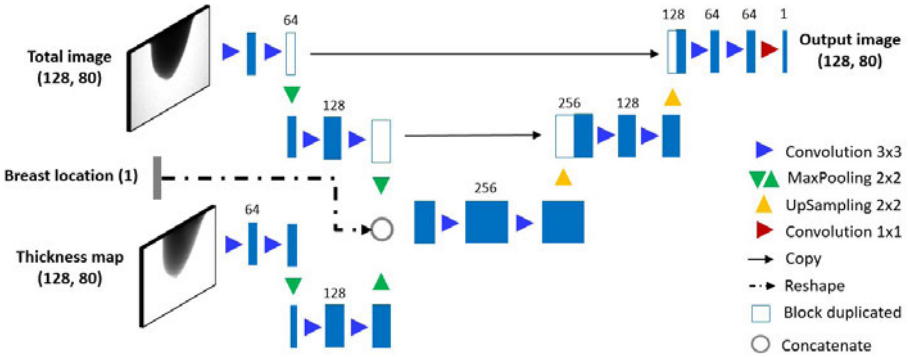

Figure 2.3: Schematic overview of the DL architecture used for scatter estimation. The total projection images of size 128 × 80 pixels were defined as the main input, while the respective thickness maps and the breast center of mass distance were included at the network bottleneck.

2.5 Deep learning model validation

DL-estimated scatter images were obtained from the MC-simulated total images of the validation (n = 60 projections from 5 breast samples) and test set (n = 120 projections from 10 breast samples), and then compared with the MC-simulated scatter images in the projection domain. Comparison was also performed by stratifying the validation and test set cases according to breast thickness, breast density (calculated, by mass, in the original breast phantoms), and breast location, to evaluate the potential correlation of these factors on the scatter estimation error.

For model accuracy evaluation, the mean relative difference (MRD) and mean absolute error (MAE), both in percentages, were computed for all comparisons only considering the projected breast area (i.e., excluding the open field). The MAE in percentage was calculated as follows:

$$MAE\ (\%) = \frac{100\%}{n}\sum_{i=1}^{n}\left|\frac{y_{i_{true_{MC}}} - y_{i_{estimated_{DL}}}}{y_{i_{true_{MC}}}}\right| \quad (2.3)$$

Where $Y_{true_{MC}}$ and $Y_{estimated_{DL}}$ are vectors containing all n pixels that conform the breast in the MC-simulated and the DL-estimated scatter images, respectively.

In a previous work[86] the effect of ignoring the chest wall was evaluated and found to have a negligible impact on the effectiveness of scatter correction (in addition to the fact that, as already mentioned, this part of the image is typically non-diagnostic due to image artifacts). Consequently, to calculate MRD and MAE in both sets (validation and test), the pixels of homogenous breast tissue (see Section 2.1) added at the chest wall in each projection were ignored.

2.5.1 Effect of additional input parameters

Next, the benefit of the additional inputs (breast location and thickness map) was evaluated, by retraining the network with only the input MC projection, and with each of the extra inputs included. This comparison was performed retrospectively, i.e., the architecture, hyperparameters, and training conditions were not modified. The error was calculated in each setting and plotted as a function of mean breast thickness.

2.5.2 MC-simulated bCT acquisition

For a single phantom of the test set, MC simulations were repeated to generate 300 projections with an angular step of 1.2° (instead of a 30° step), to mimic a complete bCT acquisition. From this MC-simulated dataset, consisting of 300 primary (P_{MC}) and scatter (S_{MC}) projections, and their corresponding 300 total ($T_{MC} = P_{MC} + S_{MC}$) projections, three reconstructions were obtained and compared: the total uncorrected reconstruction using the T_{MC} projections, the primary-only reconstruction from the P_{MC} projections (or MC ground truth), and the corrected reconstruction from the T projections after DL-correction ($P' = T_{MC}-S_{DL}$). Image reconstruction was performed in all cases using a maximum likelihood in transmission method (ML-TR).[48] The structural similarity (SSIM) obtained with the "structural_similarity" function of the skimage metrics module (with sliding windows size = 7) and the MAE between 100 slices (of the total ~500 slices) of the DL-corrected (P') and MC ground truth (P_{MC}) reconstructions were calculated.

2.6 Application on Clinical Data

In addition to the tests performed on MC simulations, the scatter was corrected on three bCT patient images. These images were acquired with the bCT system installed at Radboud University Medical Center for an unrelated, ethics-approved trial.

To estimate the scatter present in these images, the bCT projections were resized to 128×80 and the model was applied. Then, the estimated scatter of the complete set was

again resized to match the bCT acquisition dimensions. Finally, the estimated scatter was subtracted from the uncorrected images, and the results used for reconstruction.

To evaluate the reduction of the cupping artifact due to the scatter correction, visual and quantitative comparisons of the corrected and uncorrected bCT images were performed. For the former, 10 × 300 pixel profiles through specific axial slices were plotted. For the latter, ten ROIs of 20 × 20 pixels were placed on different regions of fibroglandular and adipose tissues in the reconstructed images, and the ROI mean values were measured and quantitatively compared. These ROIs were also used to calculate the local contrast as the difference of the measured fibroglandular and adipose divided by the adipose values, for both uncorrected and corrected images.

Furthermore, the obtained mean values from the different ROIs were compared to the theoretical linear x-ray attenuation values for adipose and fibroglandular tissues, to evaluate the recovery of voxel values compared to the theoretical attenuation values.[96-98] Linear attenuation coefficients were calculated for an x-ray energy of 27.8 keV, the average x-ray energy of the spectrum used for image acquisition. Reconstructed patient images were obtained by using ML-TR[99] with beam hardening correction to the mean energy of the spectrum.[100]

As a result, a range of x-ray linear attenuation values between 0.279 - 0.318 cm^{-1} and 0.385 - 0.416 cm^{-1} for adipose and fibroglandular tissues was used, considering the variability of x-ray attenuation properties reported for breast tissues across patients and publications.[96-98]

2.7 Noise effect evaluation after scatter correction

After scatter correction by subtraction, an increase in the magnitude of high frequency noise in the reconstructed CBCT images could be expected.[101] This could yield a reduction in the contrast-to-noise ratio (CNR) of the scatter-corrected image, which may negatively impact the benefit of scatter removal.[102] Therefore, the effect of noise after scatter correction was evaluated. For this, the ROIs for the local contrast calculation, described in the previous section, were used to calculate the CNR according to the following equation:

$$CNR = \frac{\left|\bar{\mu}_{fibroglandular} - \bar{\mu}_{adipose}\right|}{\sqrt{\frac{\sigma^2_{figroglandular} + \sigma^2_{adipose}}{2}}} \tag{2.4}$$

Where $\bar{\mu}$ and σ^2 are the mean and variance, respectively, measured in each ROI. The CNR was calculated for the three uncorrected and DL-corrected bCT patient images, separately. To avoid the influence of the ROI location on the CNR calculation, the CNR was calculated between all 100 pairs of fibroglandular and adipose ROIs per bCT patient image. The CNR difference measured at the same ROI location pairs before and after correction was tested for significance using a mixed effects 2-way ANOVA with the scatter correction as fixed effect and the ROI locations as random effect.

3 Results

Figure 2.4 shows the distribution (in percentage) of the mean thicknesses of the breast samples that formed the training, validation, and tests sets, for all simulated projections.

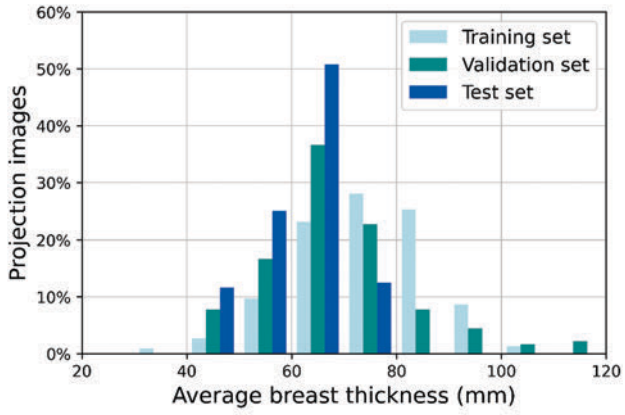

Figure 2.4: Histogram indicating average breast thickness distribution for the training (light blue), validation (dark cyan) and test (blue) sets. The number of projections in the training set (5280), validation set (60) and the test set (120) is expressed as a percentage with respect to the total number of cases in each dataset.

In the training set, the model achieved a mean MRD and MAE between MC-simulated and DL-estimated scatter projections of 0.1% (range: -0.5%, 0.5%) and 3.1% (range: 2.5%, 3.4%), respectively. The calculated mean MRD and MAE across all cases for the validation set was 0.04% (range: -1.1%, 1.3%) and 2.94% (range: 2.7%, 3.2%), respectively. One sample in the validation set was found to have thickness along the direction of x-rays outside the range of 27 mm – 108 mm defined by the training set, as shown in Figure 2.4. Therefore, the mentioned sample was

considered an outlier and excluded from the calculation of these average errors. For the test set, the MRD and MAE were -0.64% (range: - 1.6%, 0.2%) and 2.84% (range: 2.3%, 3.5%), respectively. Individual errors on a projection level are shown in Figure 2.5, as a function of the mean breast thickness.

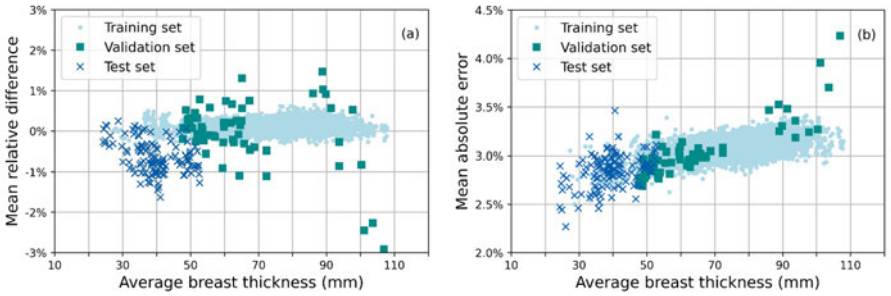

Figure 2.5: The (a) mean relative difference and (b) mean absolute error, in percentage, between the MC-simulated and DL-estimated scatter images, as a function of breast thickness for each projection in the training, validation, and test set.

Figure 2.6 shows the mean relative difference, in percentage, plotted as a function of breast density and of breast location, for the validation and test sets. The obtained Pearson's correlation coefficients calculated with the MRD as a function of breast location and breast density (by mass) were: 0.05, and -0.122 for the validation set; while for the test set, the computed values were: -0.217 and -0.190.

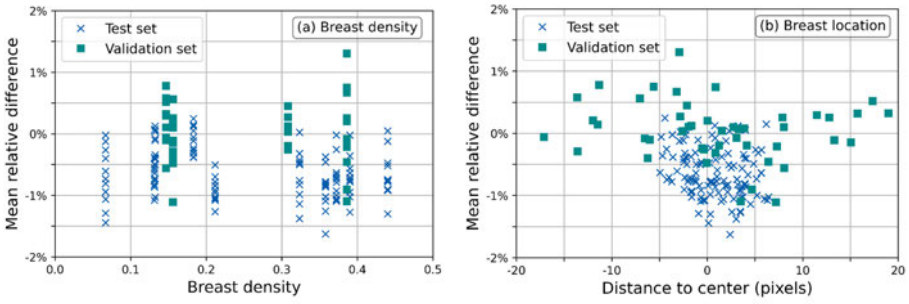

Figure 2.6: Mean relative difference, in percentage, between the MC-simulated and DL-estimated scatter images, plotted as a function of (a) breast density, and (b) breast location, to evaluate the effect of these factors on the scatter estimation error for the validation and test sets.

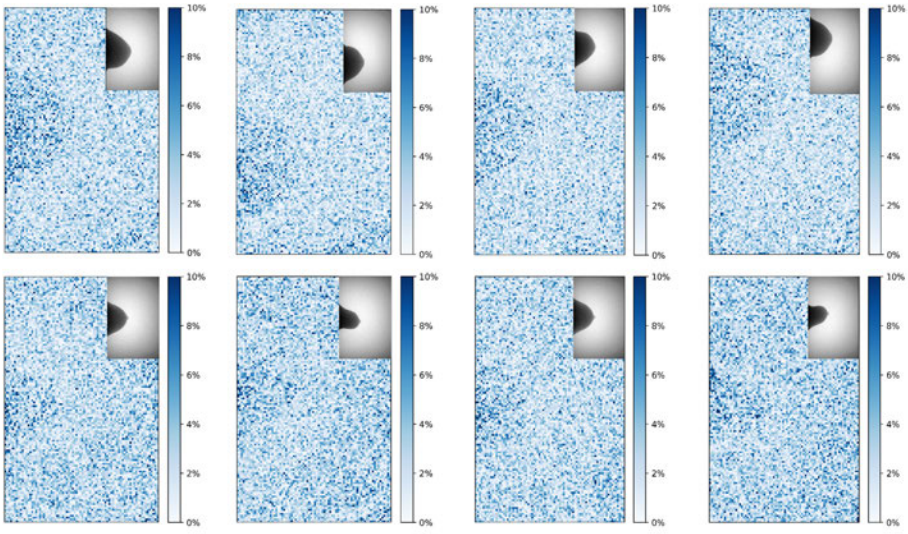

Figure 2.7: Example of error map between the MC-simulated and DL-estimated scatter images for two samples (in rows, one per acquisition system) at different acquisition angles (in columns, 0°, 90°, 180°, and 270°). Error maps show the relative absolute percent error (range: 0% to 10%) calculated pixelwise.

Figure 2.7 shows some example error maps between the MC-simulated and DL-estimated scatter projections obtained for two samples, one per bCT system (and therefore one for the internal validation, and one for the external test set). Error maps show the relative absolute percent error calculated pixelwise.

3.1 Extra inputs effect

Figure 2.8 shows the effect of the two additional parameters used as input to the model on the validation and test performance. Numerical results are listed in Table 2.1.

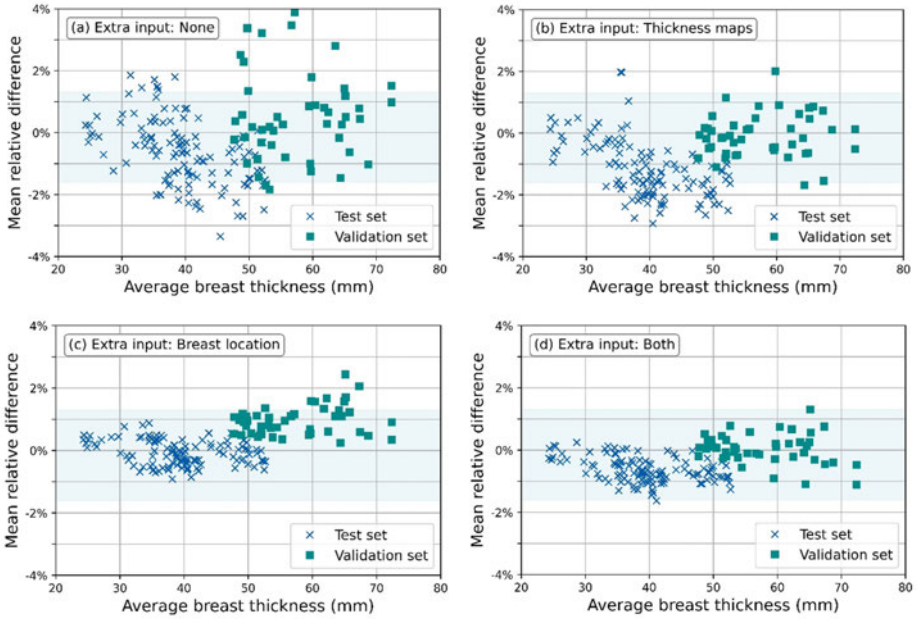

Figure 2.8: Mean relative difference plotted as a function of average breast thickness from the validation and test set for the model trained: (a) without extra inputs, (b) with only the thickness maps added as extra input, (c) with only the breast location information added as extra input; and (d) with both the thickness maps and the breast location information added as extra inputs (equal to Figure 2.5(a) after removing outlier). The light blue band in each panel represents the range of values (min, max) of the data in panel (d).

Table 2.1: Achieved accuracy for each of the evaluated combinations: no extra inputs (None), only thickness maps as extra input, only breast location as extra input and then, both extra inputs (thickness maps and breast location). The calculated MRD and MAE (min, max) were listed for the validation and the test set.

Extra inputs to the network			None	Thickness maps	Breast location	Both
Validation set	**MRD**	Mean	0.51%	-0.09%	0.96%	0.04%
		Min.	-1.84%	-1.69%	0.24%	-1.11%
		Max.	3.88%	2.00%	2.44%	1.30%
	MAE	Mean	3.19%	3.28%	3.03%	2.94%
		Min.	2.75%	2.89%	2.75%	2.69%
		Max.	4.45%	3.86%	3.52%	3.21%
Test set	**MRD**	Mean	-0.64%	-1.20%	-0.08%	-0.64%
		Min.	-3.35%	-2.93%	-0.92%	-1.63%
		Max.	1.86%	1.97%	0.87%	0.24%
	MAE	Mean	3.00%	3.86%	2.89%	2.84%
		Min.	2.27%	2.39%	2.36%	2.27%
		Max.	4.03%	5.01%	3.24%	3.46%

3.2 Monte Carlo simulated bCT acquisition

The SSIM computed over the evaluated set of 100 reconstructed slices was 0.99 and the MAE was 0.11% (range: 0%, 0.35%) with a single slice outlier of 2.06%. For that specific reconstructed slice where the outlier was found, the pixelwise difference between the reconstructed image of the ground truth and the estimated by DL was calculated, as shown in Figure 2.9.

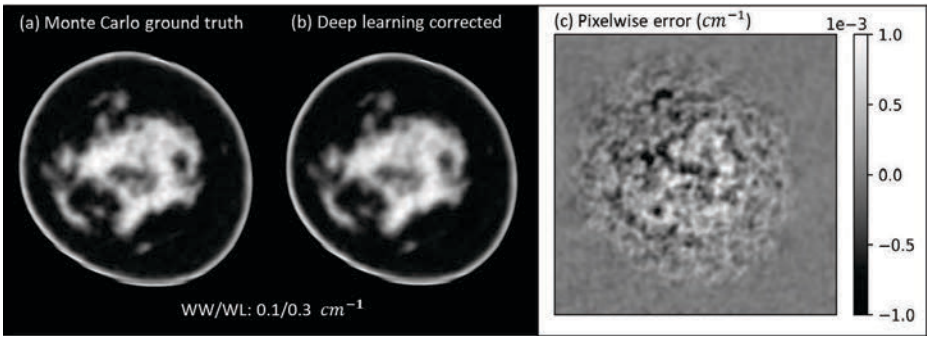

Figure 2.9: Reconstructed slice with outlier value: (a) Monte Carlo ground truth, (b) deep learning corrected and (c) pixelwise error, in units cm^{-1}, obtained by subtracting both images.

In Figure 2.10, profiles were plotted for a single reconstruction slice from a full MC simulation 300 projection set.

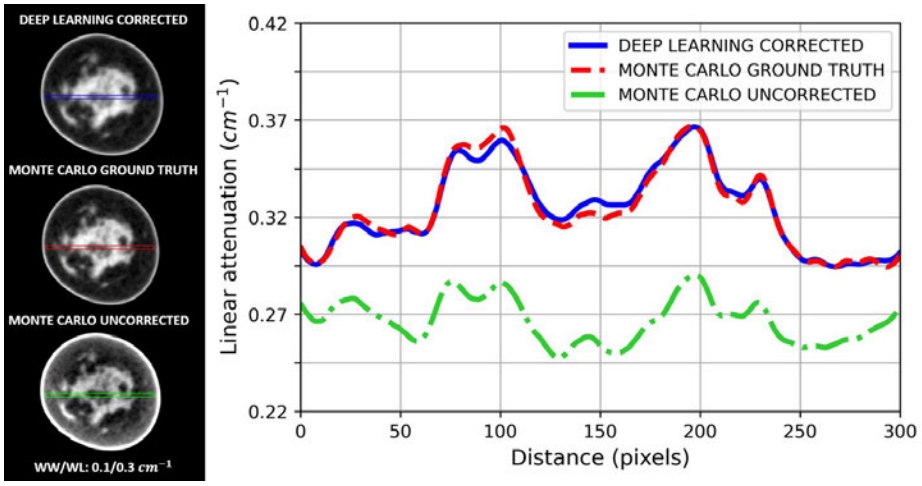

Figure 2.10: Example of profiles obtained for a Monte Carlo ground truth (red), deep-learning corrected (blue) and Monte Carlo uncorrected (green) for an MC-simulated reconstruction slice. Monte Carlo uncorrected refers to the total uncorrected reconstruction using the T_{MC} projections.

3.3 Application in Clinical Data

In Figure 2.11, profiles for a reconstructed slice of three different bCT patient acquisitions are shown. The model was found capable of accurately correcting the cupping artifact present in the uncorrected acquired images.

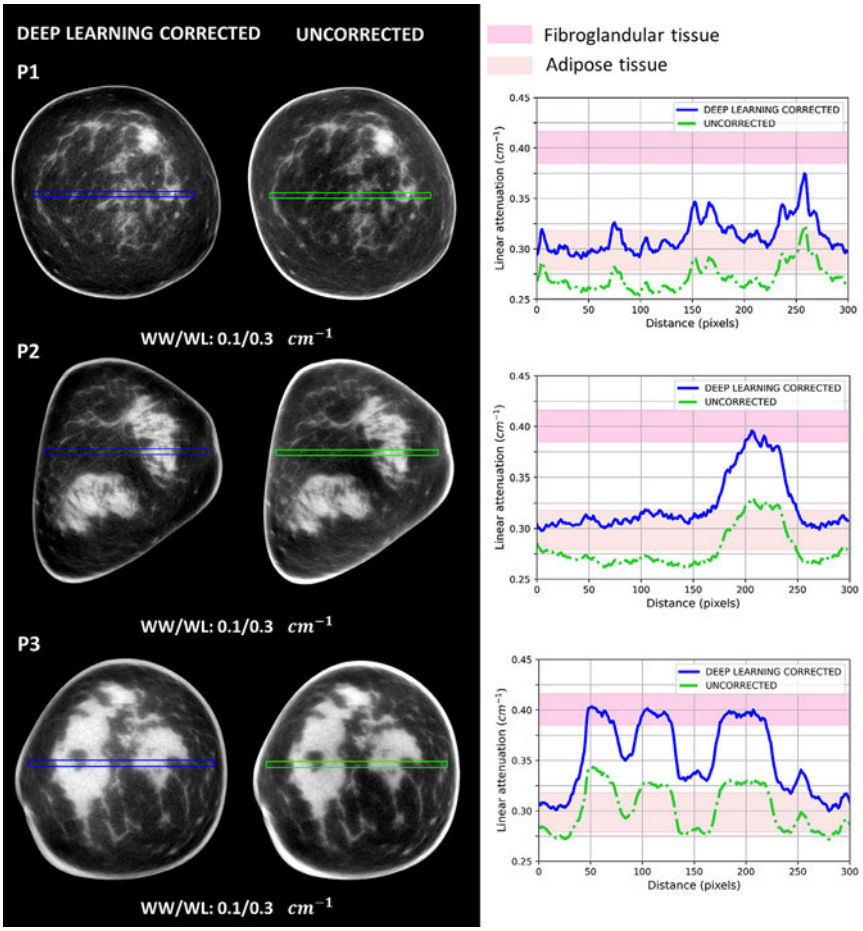

Figure 2.11: Example of profiles obtained for the three selected slices of reconstructed patient bCT images, both uncorrected and DL-corrected. The filled band represents the obtained range of x-ray linear attenuation values for fibroglandular (fuchsia) and adipose tissue (pink).

Figure 2.12 shows the box plots of the mean attenuation values for fibroglandular and adipose tissue, for the three evaluated patient cases, both uncorrected, and corrected with the developed DL model. As shown in the figure, scatter correction could recover the average voxel values to the linear attenuation coefficient found in literature for both tissues.

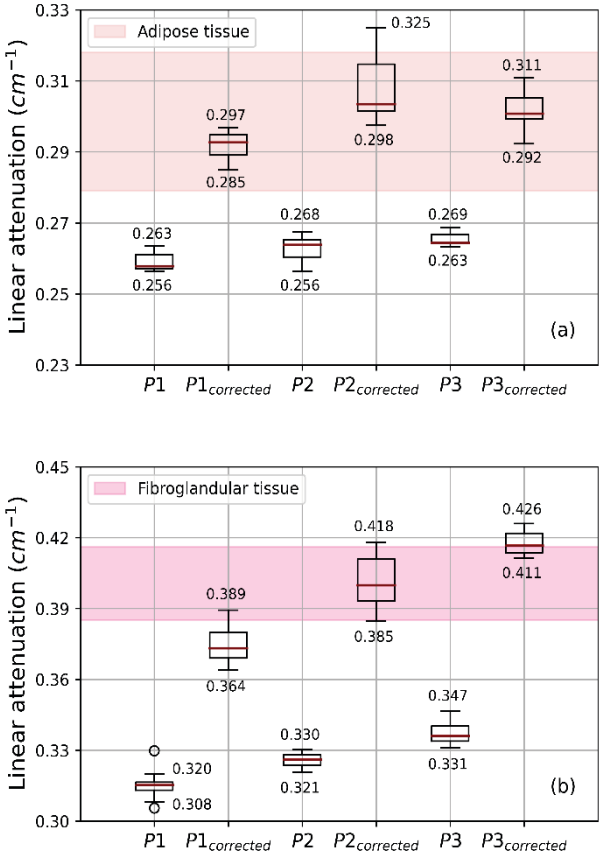

Figure 2.12: Boxplots showing the average voxel values for three reconstructed uncorrected and DL-corrected bCT patient images. The average voxel value was calculated in each patient image in 10 ROIs, half placed on adipose tissue (panel a), half on fibroglandular tissue (panel b). The measured average thickness for each case was 74 mm, 78 mm, and 72 mm, respectively. The filled bands represent the range of x-ray linear attenuation values published for adipose (pink) and fibroglandular (fuchsia) tissues. The horizontal line inside the boxes (red) indicates the median while the upper and lower limits of the boxes represent the first and third quartiles. The whiskers represent the maximum and minimum values which are shown on the plot.

The calculated contrast improvement for each patient case P1, P2 and P3 was 25%, 30% and 20% respectively. The mean CNR increased by 0.32 after scatter correction, which was not found to be significant (95% confidence interval: [-0.01, 0.65], p = 0.059). The residual distribution did not deviate from normal (p = 0.84). Figure 2.13 shows the box plots of the calculated CNRs for the three evaluated patient cases. The differences were found in both directions and are small, with the median values differing by less than 10%.

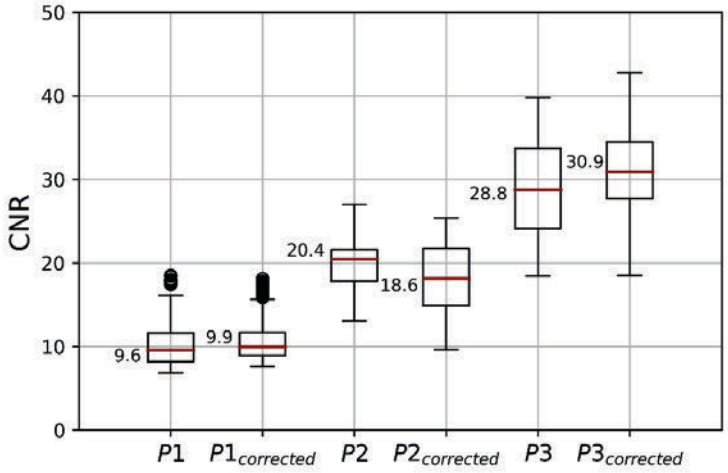

Figure 2.13: Boxplots showing the CNR values for the three example cases. The horizontal red line inside the boxes indicates the median, the boxes represent the first and third quartiles, and the whiskers represent the maximum and minimum values.

The time needed to correct the 300 projections of size 1024 × 640 pixels from a bCT scan is 58 seconds on a computer unit with an AMD Ryzen Threadripper 1950X 16-Core Processor and NVIDIA GeForce GTX 1080 GPU. The calculated time involves each of the steps of the pipeline for obtaining the scatter-corrected image: normalization, calculation of thickness maps and of the horizontal distance, scatter estimation, inversion of the normalization to scale the intensity of the obtained scatter image to the input, and subtraction of the scatter image.

4 Discussion

In this work, we developed a DL model to estimate the x-ray scatter signal in bCT projection images. When evaluated against MC simulations, the model could achieve accurate results in projection domain. When evaluated in reconstruction domain, both on simulations and on patient data, the model could correct for the cupping artifacts due to the presence of scatter, could increase the image contrast, and could recover the voxel values to the expected linear attenuation coefficient.

The proposed model was devised to estimate the scatter from a single bCT projection, with three-dimensional image information learned through the two extra inputs provided (breast location in the orthogonal direction, and thickness map). When evaluating the effect of these two additional inputs on the model performance, the

former achieved a further decrease in the dispersion of error values, and the latter helped avoid larger errors with increasing average breast thickness. These findings, therefore, confirmed the need for the inclusion of these two parameters for an optimized learning. In addition, they show that a single-projection-wise approach, when supplemented with these additional inputs, can yield accurate scatter estimates.

Moreover, because there is no useful information that can be analyzed from the reconstructed image due to the aforementioned artifacts, the chest wall was not taken into account in the error calculation. In any case, if the chest wall would have been removed completely, the resulting effect would have been minor, since Shi et al., showed that ignoring the chest wall has a negligible effect on the performance of scatter correction, mainly due to the strong signal attenuation in the chest wall region.[86]

The appropriateness of our DL approach seems to be also confirmed when put in perspective with previously reported findings obtained with DL models trained on MC simulations, performed mainly on body CBCT. For example, *Maier et al.*, who presented a U-Net-based approach for scatter estimation in body CBCT[61] reported that, in fully reconstructed images, the calculated MAE between DL-estimated and MC-simulated scatter images for different anatomical regions was less than 1.8%. Furthermore, the time required for the estimation of scatter per projection was reported to be ≈0.01 seconds. In this work, when analyzing the error in the reconstructed images, the calculated MAE was less than 1%, while the time required to correct the scatter was ≈0.2 seconds per bCT projection. Of course, while this comparison is a further confirmation of our findings, direct comparison is not possible due to inherent differences in datasets and imaging systems.

MC based on GPU has been under research and development over a number of years,[103] often requiring simplification of some of the physical simulation processes. Although performing GPU-based MC simulations has resulted in orders of magnitude speedup, it appears that an MC-GPU approach would still require ~10 hours to correct a full scan of 300 bCT projections.[104]

Importantly, our results seem to indicate no relevant dependency of the estimated accuracy as a function of breast thickness, density, and location in the field of view. This suggests that a satisfactory scatter correction can be achieved even for large, very dense breasts, and even if the breast is not positioned precisely at the bCT isocenter during acquisition. Only a single exception was found (Figure 2.5), for which the estimation error (MAE) was found considerably higher (although

still lower than 5%). However, this specific phantom presented an average breast thickness of 90 mm or higher in all simulated projections, being far from the training thickness distributions and being above the 90th percentile, according to previous literature.[105-107]

The profiles obtained from the DL-corrected patient bCT scans (Figure 2.11) showed a good agreement with the reported theoretical x-ray linear attenuation values for adipose and fibroglandular tissue in reconstructed bCT images. Furthermore, the correction could also achieve an increase in image contrast of 25% - 35% compared to the uncorrected reconstructions. This increase in contrast was similar to that obtained in previous work aimed at scatter correction in bCT images, achieved through the acquisition of a second image with a perforated tungsten plate at the exit of the x-ray tube.[84] Therefore, our approach seems to yield state-of-the-art findings, but with the important advantage of not requiring any additional hardware components or the acquisition of any additional images.

In addition, no statistically significant difference in CNR values was found between the DL scatter-corrected and uncorrected reconstructions, the calculated CNR values are close to each other for all three cases and their differences vary in sign, indicating that the CNR in the images is not really affected by the scatter correction. Although relative noise increases when the estimated scatter is subtracted from the projection, contrast also increases, keeping the ratio between noise and contrast comparable and, therefore, accurate quantitative information can be obtained without compromising the detectability, at least as represented by CNR. The small contribution of the scatter image estimated by the developed DL method to the total noise of the corrected image could be expected and may be attributable to the employed U-Net functioning as a denoiser in which many convolution layers help to generate noise-free or negligible noise output.[108]

In this study, we showed that the developed method can allow for quantitative image reconstruction, while it results in similar CNR values compared to uncorrected images. These factors point to the utility of the method in increasing image quality. However, although the CNR results are encouraging, they are not necessarily predictive of clinical task performance, which could be affected by other factors, such as higher noise correlations. In this work, we did not specifically test our approach for any clinical task, such as microcalcification detection performance. Of course, to further evaluate the appropriateness of our methods for patient image correction and clinical tasks, future work could include a larger image dataset and

human or model observers for comprehensive validation of the developed method on clinical data.

A limitation of the developed work is the potential dependency of the accuracy in scatter prediction for very large breasts (although, as mentioned, this effect was relevant only for breast above the 90th percentiles).[105-107] For this reason, to enlarge the range of the population currently considered, larger samples will be included in our training set during future investigations.

As a second limitation, the model was developed considering only a single bCT acquisition setting. If the imaging conditions vary considerably, the model must be re-trained.

In our future research, we plan to use the developed model to correct the scatter in contrast-enhanced dynamic bCT.[57] Since this involves using multiple different exposure settings, we will extend our work to generalize to the different spectra in this new system. Thanks to scatter correction, accurate image reconstruction will be possible, allowing for the correct quantification of contrast-enhancement from breast tissues and lesions, a recognized biomarker of breast lesion malignancy and aggressiveness.

5 Conclusion

We developed a deep learning model to estimate the x-ray scatter signal in bCT projection images. This model was able to estimate scatter with high accuracy, resulting in scatter-corrected images with improved contrast and without significantly affecting the CNR. These corrected images can therefore potentially be useful to improve diagnostic performance and, importantly, yield quantitative bCT image reconstructions where voxel values reflect the true physical properties of breast tissues. Furthermore, the short time required by the model to estimate (and correct) the x-ray scatter can allow its use in daily clinical practice.

3 Comparative Image Quality and Dosimetry in Breast CT Systems

Original title: Comparative image quality and dosimetric performance of two generations of dedicated breast CT systems

Juan J. Pautasso, Camille D. E. Van Speybroeck, Koen Michielsen, and Ioannis Sechopoulos

Published in Medical Physics 2025; 52(4):2191-2200. https://doi.org/10.1002/mp.17623

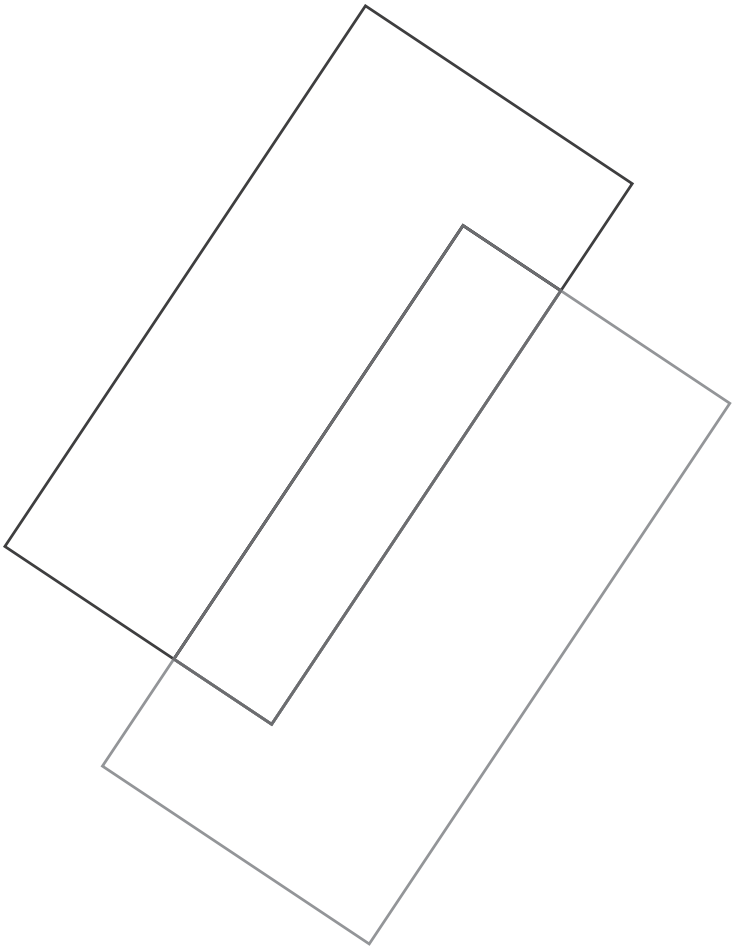

Abstract

Background

Dedicated breast computed tomography (bCT) systems offer detailed imaging for breast cancer diagnosis and treatment. As new bCT generations are developed, it is important to evaluate their imaging performance and dose efficiency to understand differences over previous models.

Purpose

To characterize the imaging performance and dose efficiency of a second-generation (GEN2) bCT system and compare them to those of a first-generation (GEN1) system.

Methods

The imaging performance was evaluated through key metrics: modulation transfer function (MTF), noise power spectrum (NPS), and detective quantum efficiency (DQE) in the projection domain. In the image domain, contrast-to-noise ratio (CNR), signal-to-noise ratio (SNR), and the visibility of calcifications were analyzed using a quality control (QC) phantom with masses and calcification clusters. Air kerma and tube output were measured and mean glandular dose (MGD) estimated for different phantom sizes for dosimetric characterization of the acquisition protocols set by the automatic exposure control (AEC).

Results

GEN2 outperformed GEN1 at higher spatial frequencies, with 57% of the MTF observed at 1 cycles/mm compared to 43% for GEN1. For a 2 mm diameter mass, GEN2 showed 60% higher CNR and 63% higher SNR. However, for larger masses, GEN1 outperformed GEN2, with CNR and SNR values higher by 12% to 44% and 14% to 43%, respectively. GEN2 also achieves higher DQE across the frequency spectrum, with 45% at 1 cycle/mm, compared to GEN1's 20%.

Regarding calcifications in the QC phantom, the 320 µm calcifications resulted in distinct full-width-at-half-maxima (FWHM ± SD), with 897 ± 58 µm for GEN1 and 811 ± 127 µm for GEN2, with a p-value of 0.19. For 290 µm calcifications, GEN1's FWHM was 866 ± 129 µm, while GEN2's was narrower at 665 ± 57 µm, with a p-value of 0.01.

The tube output was higher for GEN1 (45.2 mGy/mAs) compared to GEN2 (31.5 mGy/mAs). Additionally, GEN2 resulted in 8% lower MGD values compared to GEN1.

Conclusion

While GEN1 offers better CNR and SNR for larger masses, GEN2 provides superior resolution for calcifications, better MTF, improved DQE, and lower MGD at AEC-determined settings.

1 Introduction

Breast cancer remains the most common cancer diagnosis among women and is a major cause of cancer-related mortality worldwide.[2,109] Early detection and accurate diagnosis are critical for improving survival rates.[110-112] However, traditional breast imaging modalities often face challenges, particularly when imaging dense breast tissue. For example, mammography can struggle with tissue overlap, ultrasound may miss deeper or smaller lesions, and MRI can lead to higher false-positive rates. These limitations can hinder the early detection of small or subtle lesions, potentially impacting treatment outcomes.[4,113-115]

Dedicated breast computed tomography (bCT) systems have emerged as a promising technology that addresses many of these limitations. Unlike conventional imaging methods, bCT provides high-resolution, three-dimensional images without breast compression, enhancing both diagnostic accuracy and patient comfort.[42,116,117] Previous studies have characterized the imaging performance, dose efficiency, and clinical applications of earlier-generation bCT systems, highlighting their potential advantages and setting the stage for ongoing innovations in this technology.[40,41,44,118-121]

As newer generations of bCT systems are developed, it becomes important to evaluate their imaging performance and dose efficiency to ensure they offer significant improvements over previous models. In this study, we aimed to characterize a new bCT system, the second-generation 'Vera' (GEN2), and compare its imaging performance and dose efficiency to the first-generation 'CBCT1000' (GEN1) system, both developed by Koning Corp. (Norcross, GA, USA).

2 Material and methods

Our evaluation of image quality and dosimetry differences between the two systems focused on several metrics: modulation transfer function (MTF), noise power spectrum (NPS), detective quantum efficiency (DQE), contrast-to-noise ratio (CNR), signal-to-noise ratio (SNR), visibility of calcifications, air kerma, tube output and resulting mean glandular dose (MGD) at the automatic exposure control (AEC)-determined settings.

For this analysis, we used two distinct types of phantoms. The first, a quality control (QC) breast phantom (Figure 3.1), consists of breast-adipose equivalent material

and incorporates various embedded targets, such as masses and calcifications. The second, a slab phantom (Figure 3.2), was designed to mimic different breast sizes.

2.1 Technical specifications and operational details of GEN1 and GEN2 bCT systems

The GEN1 system, which was previously installed at our institute but has since been replaced by the recently installed GEN2 system, differs in several key technical specifications, including acquisition geometry (larger SDD but lower SID), detector type, pixel pitch, x-ray tube voltage, and voxel size. These differences are summarized in Table 3.1, which provides a detailed comparison of the two systems.

Table 3.1: Comparative overview of first-generation (GEN1) and second-generation (GEN2) bCT systems, with the specifications that are different between the two systems highlighted in bold.

	GEN1	**GEN2**
Detector Model	*Paxscan 4030 (Varian Medical System, Palo Alto, CA, USA)*	*Xineos 3030 HS (Teledyne Dalsa, Waterloo, ON, Canada)*
Detector dimensions	*397 mm × 298 mm*	*295 mm × 295 mm*
Pixel pitch	*0.388 mm (0.194 mm binned 2×2)*	*0.152 mm*
Source to detector distance (SDD)	*923 mm*	*950 mm*
Source to isocenter distance (SID)	*650 mm*	*600 mm*
X-ray tube voltage	*49 kV*	*49-65 kV**
Focal spot (nominal)	*0.3 mm*	*0.3 mm*
Pulse width	*8 ms*	*5 ms*
Projections per revolution	*300*	*225*
Permanent additional filtration	*1.5 mm Al*	*1.5 mm Al*
First half value layer	*1.39 mm Al*	*1.39 mm Al*
Rotation time (per revolution)	*10 s*	*10 s*
Reconstruction algorithm	*FDK-based*	*FDK-based*
Reconstructed voxel size	*0.273 mm*	*0.200 mm*

*Note: 49 kV is the tube voltage used for standard clinical imaging.

2.2 Evaluation of the MTF using the edge approach

The MTF for the two bCT systems were assessed in the projection domain using the edge spread function technique.[122] For comparability, GEN2's x-ray tube was set to 49 kV with 1.5 mm Al filtration, since this is its standard mode of clinical operation. A tungsten-based edge testing device (TX5, IBA Dosimetry, Schwarzenbruck, Germany) was placed directly on the detector at an angle of 3 degrees relative to the pixel grid, ensuring alignment with the central x-ray beam.[123] Using the COQ plug-in in ImageJ,[124] we determined the MTF values along the horizontal and

vertical axes. An average of two MTF measurements provided the final bCT system MTF values in the projection domain.

2.3 Evaluation of the NNPS

For both bCT systems, normalized NPS (NNPS) were determined in the projection domain at air kerma at the isocenter levels of 5.0 mGy, 12.7 mGy, and 25.6 mGy for GEN1, and 4.5 mGy, 11.0 mGy, and 22.3 mGy for GEN2, with the slight mismatch in dose levels due to the limited selection of exposure settings that can be set for a scan. Identical spectral conditions (49 kV with a 1.5 mm Al filter) were used as those used for MTF analysis, along with additional 14 mm of Al added at the source to mimic the attenuation of x-rays through breast tissue. The procedure for each system involved capturing 300 projections for GEN1 and 225 projections for GEN2. Each set of projections underwent a standard flat-field correction process. For the NNPS calculation, the COQ plug-in of ImageJ was again used, resulting in a one-dimensional NNPS, representing the radial average of the two-dimensional one.[125]

2.4 Evaluation of the DQE

The DQE for GEN1 and GEN2 systems at 12.7 mGy and 11.0 mGy, respectively, was calculated using the following equation, where q_0 denotes the photon fluence incident on the detector surface.

$$DQE = \frac{MTF^2}{q_0\, NNPS} \tag{3.1}$$

The x-ray spectrum and photon fluence of each system were modeled, as described in Section 2.1, using the SpekPy software (version 2.0.8, October 2020).[126] The implementation details for GEN2 were documented in our previous research, and the same methodology was applied to GEN1.[127] Additionally, the air kerma was measured after passing the x-ray beam output through various thicknesses of aluminum to validate the accuracy of the modeled spectra and calculate the first half-value layer.

2.5 CNR and SNR calculation

The CNR was computed to assess the system's ability to differentiate tissue types or materials using five (2 mm, 3 mm, 4 mm, 6 mm, and 8 mm in diameter, Figure 3.1) of the seven spherical epoxy resin masses present in a QC breast phantom. Signal ROIs, small enough to avoid edge effects, and background ROIs were measured and averaged over ten slices along the z-axis. The phantom was scanned using both the GEN1 and GEN2 systems, with air kerma levels set at 12.7 mGy and 11.0 mGy, respectively.

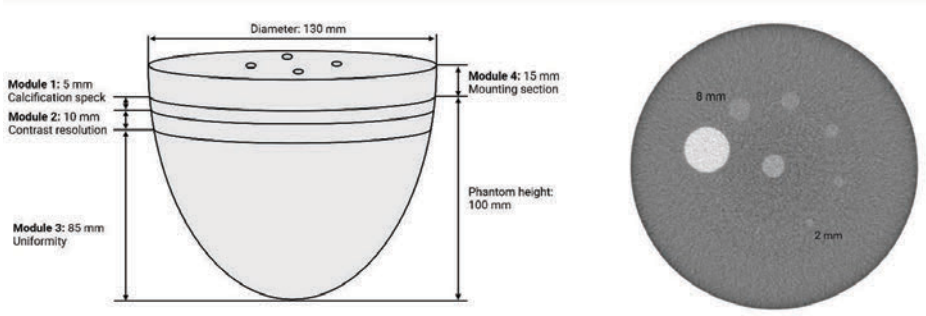

Figure 3.1: QC phantom used for estimation of CNR, SNR, and calcification visibility. (Left) A schematic representation showing modular sections: calcification speck (Module 1), contrast resolution (Module 2), uniformity (Module 3), and mounting section (Module 4), with dimensions specified. (Right) Detailed view of Module 2, highlighting the inserts for evaluating the contrast resolution, acquired with GEN2 and used for CNR calculations. WW/WL: 350/-250.

The CNR was then calculated as the average pixel intensity difference between object ($\bar{I}_o$) and background ($\bar{I}_{bg}$) ROIs, normalized by the background ROI's standard deviation (σ_{bg}).

$$CNR = \frac{\bar{I}_o - \bar{I}_{bg}}{\sigma_{bg}} \tag{3.2}$$

To account for the effect of mass size on the evaluation, the SNR (referred to as SNR_{Rose}) was calculated using the Rose signal definition.[118,128] This metric takes into account the number of pixels (*N*) within the specified ROI that had the same physical size but different pixel pitch, given by:

$$SNR_{Rose} = CNR \times \sqrt{N} \tag{3.3}$$

2.6 Evaluation of calcification visibility

The QC phantom used in this study includes a calcification speck module (Module 1, Figure 3.1) containing six patterns of calcifications with diameters of 320 µm, 290 µm, 270 µm, 240 µm, 220 µm, and 160 µm. These patterns are uniformly distributed along a circle with a 40 mm radius, all located within the same phantom slice.

To assess the spatial resolution of both systems, 10 mm-long profiles were positioned to pass through the centers of six specks in two calcification clusters (320 µm and 290 µm). Intensity profiles were extracted, and the full width at half maximum (FWHM) was calculated for each of the six calcifications of the same size in each cluster. The FWHM values were then averaged to obtain a mean FWHM for each cluster. The standard deviation and 95% confidence intervals (CIs) of the sample mean were

also calculated and reported. Additionally, the two sets of FWHM were compared for statistical significance using a paired t-test, and the resulting p-values were included.

2.7 Air Kerma measurements

A pencil beam ion chamber (10X6-3CT, Radcal Corp., Monrovia, CA, USA), linked to a dosimeter (Accu-Gold+ Touch Pro control unit, Radcal Corp.), was positioned at the isocenter and aligned with the central ray of the x-ray beam. Air kerma measurements were conducted for both systems across the full range of tube current settings: 40 mA, 50 mA, 64 mA, 80 mA, 100 mA, 125 mA, and 160 mA.

2.8 Mean glandular dose estimation

We aimed to assess the MGD during standard bCT acquisition protocol for GEN1 and GEN2, as per their corresponding AECs. To achieve this, we first modelled the x-ray spectrum and tube output of each system using SpekPy, considering the spectral and geometric characteristics established in Section 2.1.

Initially, we determined the number of photons per energy bin and the photon fluence (Φ_E) in photons/cm^2. We conducted a Monte Carlo (MC) simulation using the Geant4 toolkit (v.11.1.3, Nov 2023), based on a previously validated algorithm for the GEN1 system.[44] The validation was performed by comparing the simulation results with experimental measurements. The simulation tracked 10^6 photons, and a pencil beam ion chamber (100 mm × 10 mm) was simulated by positioning the detector at the isocenter. The pixels corresponding to the chamber's size and shape were selected, ensuring alignment perpendicular to the central ray.

The simulation results were averaged to obtain the mean fluence ($\overline{\Phi}_{MC}$). The Φ_E was then normalized (Φ'_E), and the normalized values were then scaled by the average pixel intensity from the pencil beam simulation ($\overline{\Phi}_{MC}$), resulting in the adjusted energy fluence Φ_N:

$$\Phi_N[i] = \Phi'_E[i] \times \overline{\Phi}_{MC} \tag{3.4}$$

Next, the normalized energy fluence (Φ_N) was multiplied by the mass energy-absorption coefficient for air (μ_{en}/ρ) obtained from NIST data tables,[129] to calculate the air kerma at isocenter (AK_I):

$$AK_I[i] = \Phi_N[i] \times \left(\frac{\mu_{en}}{\rho}\right)[i] \times 1.602 \times 10^{-16}\ \text{J/keV} \tag{3.5}$$

These values were validated by comparing them with empirical air kerma measurements taken at the isocenter for each system, as described in Section 2.7.

Then, the mean absolute error (MAE) in percentage was calculated as:

$$MAE\ (\%) = \frac{100\%}{n} \sum_{i=1}^{n} \left| \frac{y_{i_{measured}} - y_{i_{simulated}}}{y_{i_{measured}}} \right| \tag{3.6}$$

where $y_{measured}$ and $y_{simulated}$ represent the empirical measurements and the calculated AK_i, respectively.

Finally, the normalized glandular dose (DgN) was calculated for breasts with a fixed volume density of 14.3%,[106] and these results were compared to the values for the GEN1 system. The simulation was then adapted for the GEN2 system to similarly determine the DgN. Our findings were compared with the values for different breast sizes previously published by Sechopoulos et al.,[44] and the mean difference (MD) in percentage was calculated:

$$MD\ (\%) = \frac{100\%}{n} \sum_{i=1}^{n} \frac{y_{i_{published}} - y_{i_{present}}}{y_{i_{published}}} \tag{3.7}$$

Where $y_{published}$ and $y_{present}$ represent the previously published values and our findings.

2.9 Phantom analysis: MGD

After obtaining the DgN conversion factors, we calculated the MGD for three different breast phantom sizes: small, medium, and large, as depicted in Figure 3.2. The dimensions of the phantoms are also listed in Figure 3.2. The three phantoms were placed at the isocenter, and the AEC of the bCT system determined the optimal tube current for each case. The conversion factor for each breast size was multiplied by the corresponding air kerma value to obtain the MGD.

Small	Medium	Large
		
CWD: 14 cm CND: 6 cm	CWD: 17 cm CND: 10 cm	CWD: 18 cm CND: 14 cm

Figure 3.2: Three phantom sizes used to mimic different breast volumes for absorbed dose assessment: small (left), medium (center), and large (right). CWD refers to the chest-wall diameter, and CND refers to the chest-wall-to-nipple distance.

3 Results

3.1 Presampled MTF at the detector

Figure 3.3 shows the measured presampled MTF for the GEN1 and GEN2 systems. A slight difference was observed between the horizontal and vertical directions for both GEN1 and GEN2, but too small to be clearly distinguishable in the printed figure.

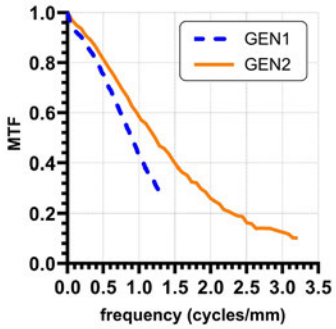

Figure 3.3: GEN1 (blue-dashed line) and GEN2 (orange line). Measured MTF in the projection domain plotted as a function of frequency.

The MTF at 1.0 cycles/mm is 57% for GEN2 and 43% for GEN1.

3.2 NNPS at the detector

Figure 3.4 shows the measured NNPS for the GEN1 and GEN2 systems.

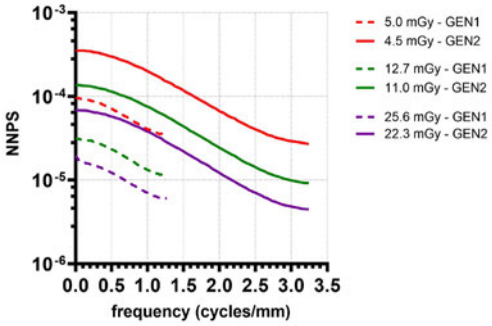

Figure 3.4: shows the NNPS measured at the detector, in the projection domain, for both systems and plotted against frequency. The GEN1 is represented by dashed lines, while the GEN2 system is indicated by a solid line.

The NNPS at 1.0 cycles/mm is 1.9×10^{-4}, 7.3×10^{-5} and 3.7×10^{-5} for GEN2 compared to 4.0×10^{-5}, 1.3×10^{-5}, and 6.94×10^{-6} for GEN1.

3.3 Detective quantum efficiency

Figure 3.5 presents the DQE for GEN1 and GEN2. The number of incident photons per cm^2 (q_0) retrieved from the SpekPy simulation was 1.07×10^4 and 1.06×10^4 photons for GEN1 and GEN2, respectively.

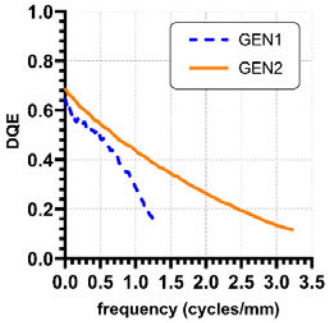

Figure 3.5: depicts the DQE measured at the detector for both systems, plotted against frequency. The GEN1 system is represented by a blue dashed line, while the GEN2 system is indicated by an orange solid line.

GEN2 achieves higher DQE across the frequency range, with 60% DQE at 0.5 cycles/mm and 45% at 1 cycle/mm, compared to GEN1's 50% and 20%, respectively.

3.4 Contrast- and signal-to-noise ratio

In Figure 3.6, CNR and SNR measurements for GEN1 and GEN2 systems plotted against mass diameter.

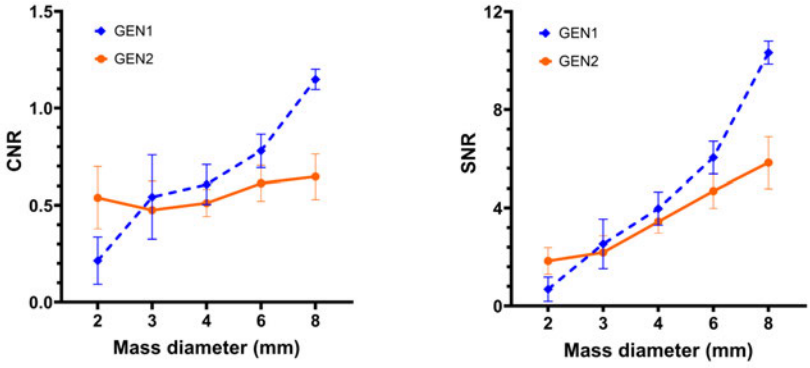

Figure 3.6: The left plot shows CNR values, while the right plot shows SNR values. Error bars indicate the standard deviation of measurements. The GEN1 system is represented by blue diamond markers and dashed lines, while the GEN2 system is indicated by orange circle markers and solid lines.

GEN2 exhibited a 60% higher CNR for the 2 mm mass compared to GEN1. However, for larger masses, GEN1 outperformed GEN2, with CNR differences of 12%, 16%, 21%, and 44% higher for the 3 mm, 4 mm, 6 mm, and 8 mm masses, respectively. Similarly, SNR results showed that GEN2 had a 63% higher SNR for the 2 mm mass. For larger masses, GEN1 again demonstrated superior performance, with SNR differences of 14%, 13%, 22%, and 43% higher for the 3 mm, 4 mm, 6 mm, and 8 mm masses, respectively.

3.5 Visibility of calcifications

Figure 3.7 depicts the analysis of two sets of calcifications, 320 µm and 290 µm in size. For the 320 µm calcifications, the FWHM values were 897 ± 58 µm (95% CI: [836, 959]) for GEN1 and 811 ± 127 µm (95% CI: [678, 944]) for GEN2, with a p-value of 0.19 (not significant). For the 290 µm calcifications, the FWHM values were 866 ± 129 µm (95% CI: [730, 1002]) for GEN1 and 665 ± 57 µm (95% CI: [605, 725]) for GEN2, with a p-value of 0.01 (significant).

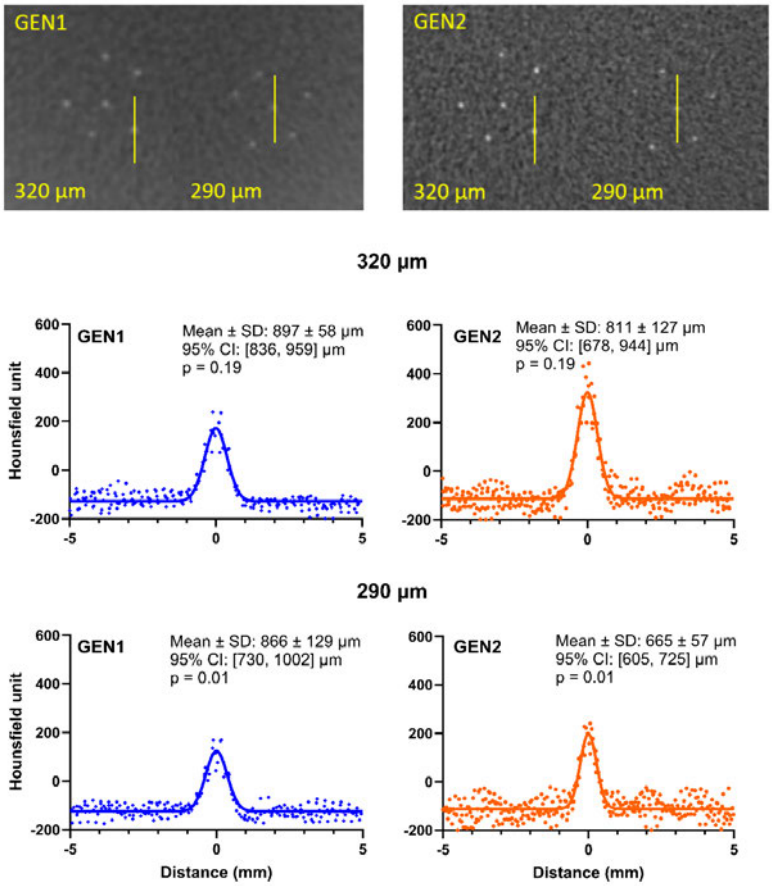

Figure 3.7: Comparison of calcification measurements for 320 µm and 290 µm clusters using GEN1 and GEN2 systems. Graphs show 10-mm long intensity profiles (depicted in yellow in images) for both systems, with FWHM values, standard deviations (SD), 95% confidence intervals (CI), and statistical significance (p-values) included. GEN1 is represented in blue, and GEN2 is represented in orange. The Gaussian fits in the graphs were derived from the calculated average FWHMs. WW/WL: 1420/130.

3.6 Air Kerma measurements

Figure 3.8 illustrates the linear relationship between tube current and air kerma for both the GEN1 and GEN2 systems. The linear fit equations are provided for both systems: Y = 0.25 X for GEN1 and Y = 0.23 X for GEN2 with R2 = 0.99 in both cases.

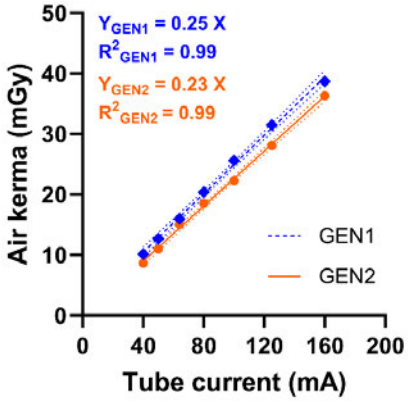

Figure 3.8: Air Kerma as a function of tube current for GEN1 (blue diamonds) and GEN2 (orange circles). The 95% confidence intervals were also plot for GEN1 and GEN2.

3.7 Mean glandular dose

The MAE (min; max) between empirical measurements and the simulated AK_i was computed as 3% (1%; 4%) for GEN1 and 3% (1%; 6%) for GEN2.

The conversion factors for GEN1 and GEN2 are derived from the calculations and listed in Table 3.2:

Table 3.2: The table presents the number of photons at isocenter, air kerma per milliampere seconds at the isocenter for both GEN1 and GEN2 systems.

System	Num. of Photons	Tube output at isocenter (mGy/mAs)
GEN1	1.44×10^{14}	45.2
GEN2	9.57×10^{13}	31.5

In Table 3.3, the DgN coefficients for breasts of varying sizes are presented:

Table 3.3: DgN coefficients in mGy per mGy of air kerma for breasts of varying sizes, considering a glandularity of 14.3% by volume. Air kerma at the isocenter of the bCT system (49 kV/1.5 mm Al) was taken as reference.

Chest-wall diameter (cm)	Chest wall-to-nipple distance (cm)	DgN (mGy/mGy) GEN1 previously published[14]	DgN (mGy/mGy) GEN1 (this work)	Diff GEN1/GEN1-published	DgN (mGy/mGy) GEN2
10	5	0.52	0.50	3.72%	0.50
	7.5	0.54	0.52	4.20%	0.54
	10	0.56	0.54	4.03%	0.55
12	6	0.47	0.46	3.44%	0.47
	9	0.50	0.48	3.27%	0.49
	12	0.51	0.49	3.55%	0.50
14	7	0.44	0.42	3.06%	0.43
	10.5	0.46	0.45	2.36%	0.45
	14	0.47	0.46	2.60%	0.47
16	8	0.40	0.39	3.33%	0.40
	12	0.42	0.42	2.19%	0.42
	16	0.43	0.43	2.05%	0.43
18	9	0.38	0.37	2.29%	0.37
	13.5	0.39	0.38	2.28%	0.39
	18	0.40	0.39	2.00%	0.40

From Table 3.3, the MD (min; max) between the current GEN1 values and the previously published GEN1 values was 2.96% (2.00%; 4.20%).

3.8 Phantom analysis: mean glandular dose

Table 3.4 presents the MGD for small, medium, and large phantom sizes in both GEN1 and GEN2 systems. On average, GEN2 delivers 8% lower MGD than GEN1.

Table 3.4: MGD for different phantom sizes in GEN1 and GEN2 systems. The automatic exposure control determined the optimal tube current to be used for each case. "CWD" refers to chest-wall diameters, and "CND" refers to chest-to-nipple distances.

Phantom size (cm) (CWD × CND)	Tube current (mA)	Air Kerma at isocenter (mGy)		MGD (mGy)	
		GEN1	*GEN2*	*GEN1*	*GEN2*
Small (14 × 6)	*40*	*10.2*	*8.7*	*4.3*	*3.7*
Medium (17 × 10)	*64*	*16.0*	*15.1*	*5.9*	*5.7*
Large (18 × 14)	*80*	*20.4*	*18.5*	*7.9*	*7.3*

4 Discussion

When comparing the GEN2 with the older GEN1, several key performance improvements and trade-offs become evident. GEN2 demonstrates a clear enhancement in spatial resolution (Figure 3.3). This increased resolution is largely due to GEN2's detector with smaller pixel pitch and no binning, although this also results in higher noise levels (Figure 3.4). In contrast, GEN1 benefits from a larger pixel size and 2 × 2 binning, which contribute to lower noise levels.

GEN2 also achieves higher DQE across the frequency spectrum, with 60% DQE at 0.5 cycles/mm and 45% at 1 cycle/mm, compared to GEN1's 50% and 20%, respectively (Figure 3.5). This enhanced photon detection efficiency contributes to the overall improved image quality in GEN2, despite the increased noise.

In terms of CNR and SNR, GEN1 performs better at larger mass diameters, indicating its effectiveness in detecting contrast differences in larger masses (Figure 3.6). However, GEN2 provides superior resolution and edge definition for smaller features, such as calcifications, as shown by its narrower FWHM values (Figure 3.7).

The air kerma analysis indicates a linear relationship with tube current for both systems. GEN1 has a slightly higher tube output rate due to its longer pulse width and more projections per revolution. In contrast, GEN2, with its shorter pulse width and fewer projections, reduces the overall dose while still maintaining sufficient image quality, likely due to the lower electronic noise of its CMOS detector. Although GEN1 produced a higher number of photons at the isocenter, GEN2 had a higher air kerma per mAs. Additionally, although GEN2 generally exhibits slightly higher normalized glandular dose values, it maintains efficiency in dose management, delivering lower MGD across different phantom sizes. The glandular dose decreases with increasing breast diameter and decreasing chest-wall-to-nipple distance, in alignment with previously published studies.[44]

The MGD analysis in Table 3.4 highlights that at the AEC settings, GEN2 consistently provides lower MGD values across small, medium, and large phantom sizes, indicating its improved dose efficiency while preserving image quality. However, the suitability and comparability of the clinical performance of the images resulting from the two generations when using their AEC at the manufacturer-determined settings, as tested here, remains to be evaluated.

5 Conclusion

Although GEN1 demonstrates higher CNR and SNR for larger masses, GEN2 provides superior spatial resolution for calcifications, better MTF, and improved DQE. While GEN2's smaller pixel pitch results in higher noise levels, it compensates with enhanced photon detection efficiency and sharper edge definition. Additionally, GEN2 delivers these improvements while consistently providing lower MGD at the AEC settings across different breast sizes, making it more efficient overall.

4 Optimization of a Breast CT for Contrast-Enhanced Imaging

Original title: Characterization, validation, and spectral optimization of a dedicated breast CT system for contrast-enhanced imaging

Juan J. Pautasso, Koen Michielsen, and Ioannis Sechopoulos

Published in Medical Physics 2024; 51(5):3322-3333. https://doi.org/10.1002/mp.17069

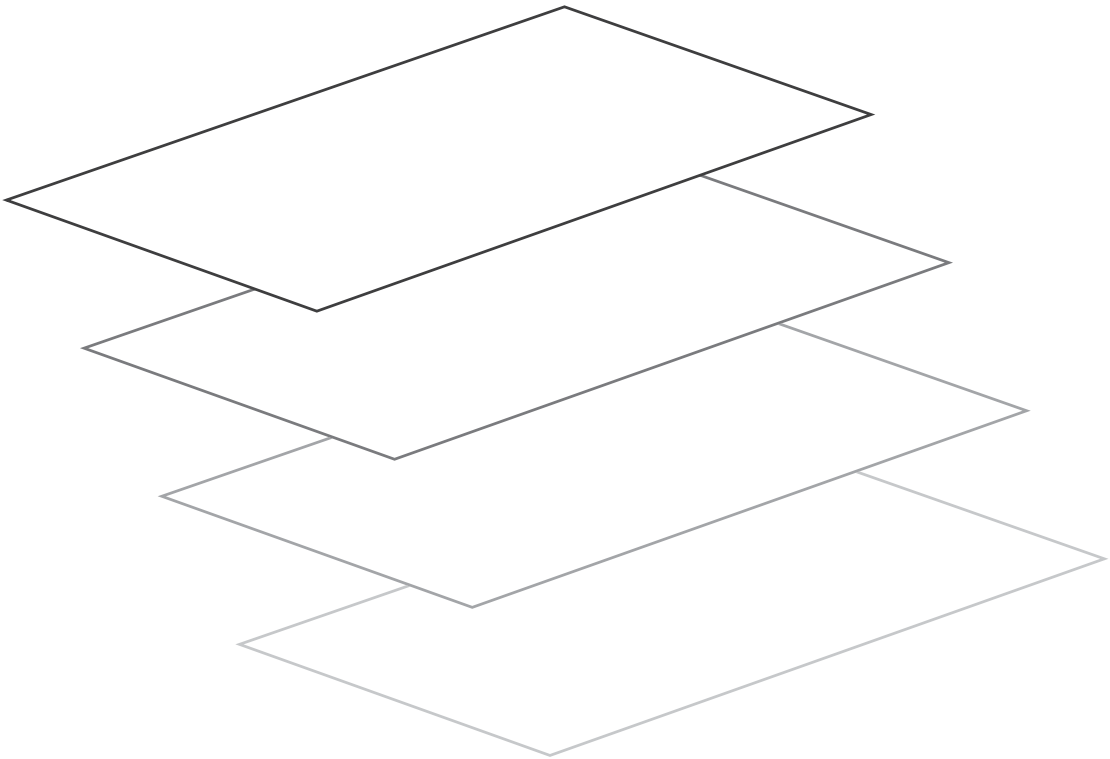

Abstract

Background

The development of a new imaging modality, such as 4D dynamic contrast-enhanced dedicated breast CT (4D DCE-bCT), requires optimization of the acquisition technique, particularly within the 2D contrast-enhanced imaging modality. Given the extensive parameter space, cascade-systems analysis is commonly used for such optimization.

Purpose

To implement and validate a parallel-cascaded model for bCT, focusing on optimizing and characterizing system performance in the projection domain to enhance the quality of input data for image reconstruction.

Methods

A parallel-cascaded system model of a state-of-the-art bCT system was developed and model predictions of the presampled modulation transfer function (MTF) and the normalized noise power spectrum (NNPS) were compared with empirical data collected in the projection domain. Validation was performed using the default settings of 49 kV with 1.5 mm aluminum filter and at 65 kV and 0.257 mm copper filter. A 10 mm aluminum plate was added to replicate the breast attenuation. Air kerma at the isocenter was measured at different tube current levels.

Discrepancies between the measured projection domain metrics and model-predicted values were quantified using percentage error and coefficient of variation (CoV) for MTF and NNPS, respectively. The optimal filtration was for a 5 mm iodine disk detection task at 49 kV, 55 kV, 60 kV, and 65 kV. The detectability index was calculated for the default aluminum filtration and for copper thicknesses ranging from 0.05 mm to 0.4 mm.

Results

At 49 kV, MTF errors were +5.1% and -5.1% at 1 cycle/mm and 2 cycles/mm, respectively; NNPS CoV was 5.3% (min=3.7%; max=8.5%). At 65 kV, MTF errors were -0.8% and -3.2%; NNPS CoV was 13.1% (min=11.4%; max=16.9%). Air kerma output was linear, with 11.67 µGy/mA (R^2=0.993) and 19.14 µGy/mA (R^2=0.996) at 49 kV and 65 kV, respectively. For iodine detection, a 0.25 mm-thick copper filter at 65 kV was found optimal, outperforming the default technique by 90%.

Conclusion

The model accurately predicts bCT system performance, specifically in the projection domain, under varied imaging conditions, potentially contributing to the enhancement of 2D contrast-enhanced imaging in 4D DCE-bCT.

1 Introduction

Since its inception in the 1970s, dedicated breast CT (bCT) technology has evolved significantly, particularly with the advent of flat-panel detectors and computational advances in the early 2000s.[130] This technology aims to overcome the limitations of 2D mammography by offering 3D imaging.[41,42,44,45,75,131] Recent studies even propose the feasibility of 4D dynamic contrast-enhanced bCT (4D DCE-bCT) for better lesion detectability and treatment personalization.[47,48,50,57,132] To optimize this advanced bCT modality, a comprehensive analysis of the parameter space is necessary. Cascaded-systems analysis, which breaks down the imaging process into discrete stages, offers an effective methodology for this optimization.[133-145]

Cascaded models have been utilized to guide the development of innovative imaging modalities, including full-field digital mammography,[146-149] tomosynthesis,[150] and dedicated cone-beam CT.[151-154] In this study, a parallel-cascaded model was implemented and validated to assess the performance of a dedicated bCT system compared to bCT measurements in the projection domain. Since the ultimate goal is to optimize bCT performance for 4D DCE-bCT, spectral optimization was performed within the projection domain. This entailed identifying optimal technique factors that enhance the iodine contrast signal. Specifically, we measured and modeled spatial resolution, noise, and detectability in the projection domain, employing the detectability index to navigate and optimize the relevant parameter space. This strategy ensures the provision of an optimized input for subsequent reconstruction processes, thereby potentially also enhancing the overall efficacy of 4D DCE-bCT imaging.[155-159]

2 Material and methods

2.1 Dedicated breast CT system

A state-of-the-art dedicated bCT system (Koning Corp., Norcross, GA, USA) was used for this work (Figure 4.1). The system incorporates a pulsed x-ray tube and a flat-panel detector (FPD) mounted on a rotating gantry. The x-ray tube (M-1581, Varian Medical Systems, Salt Lake City, UT) has a maximum anode heat capacity of 1.1 MJ and can operate at up to a maximum voltage of 70 kV with an inherent filtration of 1.4 mm Be. It uses a rotating anode with a 10° tilted tungsten coating insert and a nominal input power of 12 kW, with a nominal focal spot size of 0.3 mm. The system allows for four voltage settings for the x-ray tube: 49 kV (default), 55 kV, 60 kV, and 65 kV. The tube current level is constrained by the system's maximum power capacity of 7 kW.

The mounted CMOS-based FPD is a Xineos 3030HS (Teledyne Dalsa, Waterloo, ON, CA) with 0.1518 mm pixel pitch and incorporates a CsI:Tl columnar scintillator that is 0.700 mm thick. The active area spans 295 × 295 mm^2 involving 1952 × 1952 pixels. At full resolution, it is capable of a readout rate of 30 frames per second. Measured MTF nominal values have been reported to be 58% and 25% at 1 cycle/mm and 2 cycles/mm, respectively.[154,160] The source is located 950 mm from the detector (SDD) and 600 mm from the isocenter (SID). A standard bCT scan involves the acquisition of 225 projections over 360°, in 10 seconds.

Figure 4.1: Dedicated bCT system installed at Radboudumc and used for this work. The system has a length of 205 cm with a maximum width of 160 cm. The operating console, located to the right in Figure 4.1, comprises a standard computer and monitor with a user interface for image acquisition and reconstruction.

2.2 bCT measurements

The Modulation Transfer Function (MTF) and Noise Power Spectrum (NPS) of the aforementioned system were assessed in the projection domain. To accomplish this, the x-ray tube was configured to operate under standard bCT clinical settings: i.e., voltage of 49 kV, pulse width of 5 ms, and a 1.5 mm additional aluminum filter of 99.999% purity. Additionally, a 10 mm thick aluminum plate, also with 99.999% purity, was placed at the x-ray tube's output to simulate the x-ray attenuation typically caused by a patient breast.

2.2.1 Presampled-MTF determination

To determine the presampled MTF of the bCT system, the edge method was utilized.[122] A tungsten edge test device (TX5, IBA Dosimetry, Schwarzenbruck, Germany) was positioned at the entrance of the detector, angled slightly by approximately 3° and aligned with the x-ray beam's central ray.[123] The test edge was positioned to measure the vertical and horizontal MTFs, with a scout image acquired after each placement.

The acquired images were analyzed using the COQ plug-in, a specialized tool for ImageJ designed for the analysis of x-ray systems.[124] From 256 × 256 regions of interest (ROIs) encompassing a portion of the tungsten edge, both horizontal and vertical presampled MTFs were extracted. These MTFs were subsequently averaged to obtain the final bCT-measured MTF in the projection domain.

2.2.2 Normalized NPS determination

Seven normalized Noise Power Spectra (NNPS) were measured in the projection domain using the bCT system, employing the same spectrum described above. These measurements were conducted at various tube current values: 20, 32, 40, 50, 64, 80, and 100 mA. Air kerma for each tube current was measured using an ion chamber connected to a dosimeter (10X6–6 chamber, 9660 ion chamber digitizer, and Accu-Pro™ 9660 control unit, Radcal Corp., Monrovia, CA, USA). The ion chamber was centered at the isocenter and aligned with the x-ray beam's central ray.

All acquired projection images were flat-field corrected through multiplication by the normalized reciprocal of the average intensity projection from the corresponding scan.

To calculate the NNPS, the COQ plug-in for ImageJ was again used. A 256 × 256 ROIs was used, aligned with the x-ray central beam axis, and included 14 lines (7 rows above and 7 below). This approach has shown good concordance with other methods described in existing literature.[125]

2.3 Parallel-cascaded model

The developed model, shown in Figure 4.2, divides the bCT system's image formation process into eight stages, each characterized as linear, shift-invariant, and spatially stationary.[133-145,161] The two initial stages account for the interaction between x-rays and the scintillator, converting the x-rays into optical photons and incorporating K-fluorescent x-ray absorption through parallel pathways. Subsequent stages focus on the processing of optical photons, from blurring effects to photodiode coupling and integration. The final stages cover the detector signal

sampling and pixel readout. For any combination of input conditions, the output of the model consists of the estimates of the MTF and the NNPS.

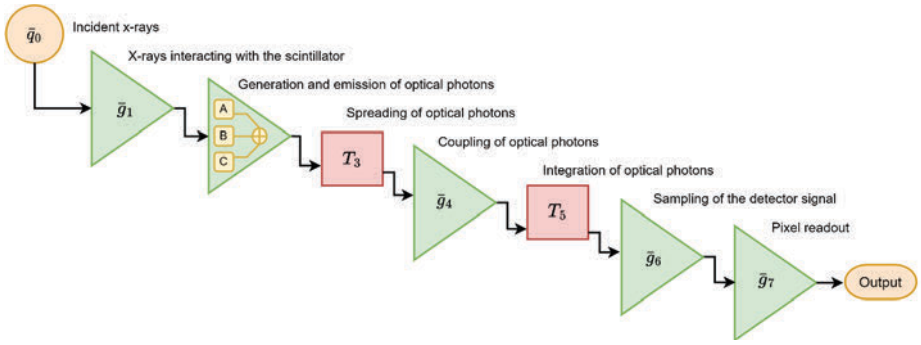

Figure 4.2: Parallel-cascaded model representation as gain (triangles in green) and spreading (squares in red) stages.

2.3.1 Stage 0: Incident x-rays

The polyenergetic x-ray spectrum was modeled using SpekPy software (v.2.0.8, October 2020) with the parameters described in Section 2.1.[126] Attenuation from 600 mm of air was accounted for to align the model with acquired data. An additional 350 mm of air attenuation and 2.5 mm of carbon fiber were added for the detector path. The scintillator's surface cover was modeled as 1 mm of silicon oxide. The stage's final output is the fluence in terms of energy and total fluence (q_0) in photons/mm^2.

2.3.2 Stage 1: X-rays interacting with the CsI:Tl scintillator

The probability of an x ray interacting with the scintillator follows a binomial process and is given by the average of the quantum efficiency $\bar{g}_1$.[140] The average quantum efficiency was computed as:

$$\bar{g}_1 = \int_0^{E_{max}} g_1(E) q_{rel}(E) dE \tag{4.1}$$

The energy-dependent quantum efficiency ($g_1(E)$) was weighted by the incident spectrum with $q_{rel}(E)$ being the incident spectrum normalized by unit area.[140] The quantum efficiency $g_1(E)$ is expressed as follows:

$$g_1(E) = 1 - exp\left[\left(\frac{\mu}{\rho}(E)\right)_{CsI:Tl} . t_{CsI} . \rho_a\right] \tag{4.2}$$

The mass attenuation coefficient for CsI:Tl was computed using the open source database XrayDB (v8.1 Python module 4.5.0, January 2023).[162] The thickness of the

scintillator is denoted as t_{CsI}. The areal density (ρ_a) is determined by multiplying the density of CsI (ρ_{CsI}) with the packing factor (PF_{CsI}). The density of CsI is 4.51 g/cm^3, and the fractional weights for cesium (w_{Cs}) and iodine (w_I) in CsI are 0.51155 and 0.48845, respectively.[129] The packing factor, PF_{CsI}, was calculated based on the assumption of body-centered cubic unit cells for atoms of Cs and I.[163]

2.3.3 Stage 2: Generation and emission of optical photons

This stage involves three distinct light emission paths: A, B, and C, each with varying interactions with K-fluorescent x-rays. By following the works of Cunningham, Yao[139] and Vedantham,[140] the average gain $\bar{g}_2$ is expressed as:

$$\bar{g}_2 = (1 - \xi\omega)\bar{g}_{2A} + \xi\omega\bar{g}_{2B} + \xi\omega f_k\bar{g}_{2C} \tag{4.3}$$

The average gains along three light emission paths A, B, and C are calculated using the variables ξ, ω, and f_k, which represent K-shell photoelectric interaction probability, fluorescence yield, and fraction of K-fluorescent x-rays absorbed in the photodiode, respectively. Values for ξ and ω are 0.83 and 0.87, obtained from Cao et al.[153] The K-fluorescent x-ray absorption factor, f_k was calculated by applying the method developed by Chan and Doi.[164]

To compute the average gains for paths A, B, and C, the scintillator was partitioned into fractional layers each with a thickness of Δt as described by Vedantham et al.[140] Subsequent to this partitioning, the spreading of K-fluorescent photons, expressed as , was determined as:

$$T_{k_{total}}(u, v) = \frac{(1 - \xi\omega)\bar{g}_{2A} + \xi\omega\bar{g}_{2B} + \xi\omega\bar{g}_{2C}f_k T_k(u, v)}{\bar{g}_2} \tag{4.4}$$

where $T_k(u, v)$ is a transfer function describing K-edge x-ray reabsorption at varying distances. It was determined using Monte Carlo simulations considering the absorption and scattering coefficients for CsI:Tl.[140,165] Attenuation coefficients corresponding to the average energy (E_K) were obtained from the NIST database.[166] During Monte Carlo simulations, the cylindrical response to an isotropic point source in a semi-infinite slab was calculated. Each photon undergoes hopping to a new position, weight dropping due to absorption, spinning into a new trajectory due to scattering, and a check to determine if the photon should terminate using the Roulette technique as detailed by Jacques.[165,167]

2.3.4 Stage 3: Spreading of optical photons

The stochastic spread of optical quanta, denoted as $T_3(u, v)$, was fitted to the function:

$$T_3(u,v) = \frac{1}{1 + Hf^2 + H^2 f^3} \tag{4.5}$$

In this equation, H serves as the fitting parameter and f represents the spatial frequency (cycles/mm).[168] This fitting parameter, also referred to as the blurring factor, was optimized using mean squared error, yielding an optimal value of 0.15. This optimization was carried out while considering all other components of the model as fixed.

2.3.5 Stage 4: Coupling of optical photons to photodiode

This stage describes the stochastic gain that operates based on the binomial process. Within this process, the probability of an incident quantum being coupled to the photodiodes of the fiber optic plate is determined by the average coupling efficiency, $\bar{g}_4$. The specific value of $\bar{g}_4$, which is 0.59 was obtained from Cao et al.[153]

2.3.6 Stage 5: Integration of optical photons by the photodiode

Stage 5 represents the deterministic spreading of optical quanta, characterize by the pixel presampling MTF:[140,144]

$$T_5(u,v) = \left|sinc(\pi a_x u) sinc(\pi a_y u)\right| \tag{4.6}$$

The light-sensitive pixel's active area is determined by a_x and a_y, derived from the pixel pitch (p_{pitch}), and the fill factor (f_{pix}).[140,168]

2.3.7 Presampling MTF

At this instance of our model, the MTF at the detector can be formulated as proposed by Cao et al.[153]

$$MTF_{det}(u,v) = T_3(u,v) T_5(u,v) T_{k_{total}}(u,v) \tag{4.7}$$

2.3.8 Stage 6: Sampling of the detector signal

Incorporating the work of Metz and Vyborny[169] and Vedantham[140,168], the pre-sampling Noise Power Spectrum (NPS) along the u-axis is defined by:

$$NPS_{pre}(u) = \bar{q}_0 \bar{g}_1 \bar{g}_4 p_{pitch}^2 f_{pix} T_5^2(u) [\bar{g}_4 T_3^2(u) \times (A(u) - \bar{g}_2) + \bar{g}_2] \tag{4.8}$$

Where:

$$A(u) = (1 - \xi\omega)\bar{g}_{2A}^2 + \xi\omega\bar{g}_{2B}^2 + \xi\omega f_k \bar{g}_{2C}^2 + 2\xi\omega f_k \bar{g}_{2B}\bar{g}_{2C} T_k(u). \tag{4.9}$$

The pixel pitch and the fill factor are denoted as p_{pitch} and f_{pix}. The specific values for these parameters were set to 0.1518 and 0.85, respectively. Following this, Equation 4.10 introduces the comb function F_{III}, which characterizes the aliasing effect caused by the sampling of quantum noise.[153]

$$NPS_s = NPS_{pre} \otimes F_{III} \tag{4.10}$$

2.3.9 Stage 7: Pixel readout

The last stage involves combining the aliased NPS with the power spectrum of the additive electronic noise, referred to as $NPS_{add} = p_{pitch}^2 \sigma_{add}^2$, to obtain the NPS at the detector NPS_{det}:

$$NPS_{det} = NPS_s + NPS_{add} \tag{4.11}$$

2.3.10 NNPS in projection images

As an extra step, the normalized NPS (NNPS) was expressed as follows:

$$NNPS = \frac{NPS_{det}}{L_{signal}^2} \tag{4.12}$$

Being L_{Signal} the large area signal defined as $p_{pitch}^2 \bar{q}_0 \bar{g}_1 \bar{g}_2 \bar{g}_4$ as suggested by Cao et al.[153]

2.4 Additional measurements for model validation

For a comprehensive validation of the developed parallel-cascaded model, the x-ray tube was also operated at a voltage of 65 kV with a pulse width of 5 ms. The standard 1.5 mm aluminum filter was replaced with a 0.257 mm copper filter, while retaining the same 10 mm aluminum plate to simulate a patient breast. The MTF and NNPS measurements in the projection domain were carried out as outlined in Sections 2.2.1 and 2.2.2, but the NNPS was measured at tube currents of 40, 50, 64, 80, and 100 mA. The choice of 65 kV and specified current levels is aimed at achieving high-quality pre-contrast images.

2.5 Error calculation between bCT-measured and model-predicted MTFs

In order to calculate the discrepancy between the MTF values measured on the bCT system and those predicted by the model, the deviation at 1 cycle/mm and 2 cycles/mm, were examined. The error was calculated as follows:

$$Error\ (\%) = \frac{y_{predicted} - y_{measured}}{y_{measured}} \times 100 \tag{4.13}$$

where $y_{predicted}$ and $y_{measured}$ represents the model-predicted and the bCT-measured MTFs in the projection domain, respectively.

2.6 Error calculation between bCT-measured and model-predicted NNPS

For the NNPS, the model's predictive performance was assessed by first calculating the residuals using the root-mean-square error (RMSE):

$$RMSE = \sqrt{\frac{\sum_i^n (y_{predicted_i} - y_{measured_i})^2}{n}} \tag{4.14}$$

where $y_{predicted}$ and $y_{measured}$ refer to the values predicted by the NNPS model and those measured by the bCT in the projection domain, respectively, while stands for the total number of samples.

These values were then normalized by the average of the bCT-measured values for each case, resulting in the coefficient of variation (CoV), expressed as a percentage:

$$CoV\ (\%) = \frac{RMSE}{\bar{y}_{measured}} \times 100 \tag{4.15}$$

2.7 Task-based spectral optimization

After characterizing the bCT system as described in Section 2.1 and validating the developed parallel-cascaded model, the model was used to determine the optimal spectral settings for imaging iodine with 4D DCE-bCT. For this, the parallel-cascaded model was first used with the x-ray tube voltage set to 49 kV, and the air kerma limited to 6 mGy. This limitation is imposed to ensure a fair comparison across thickness and tube-current settings. The breast was simulated with an average thickness of 80 mm, comprising 15% fibroglandular tissue and 85% adipose tissue, positioned at the isocenter.[106,170] These tissues were defined as having the chemical composition and density given by the NIST database.[171]

Iodine enhancement within breast lesions was modeled by integrating an iodine weight fraction (W_I) based on a specified iodine concentration (C_I) of 10 mg/mL, accounting for the distinct densities of breast tissue ($\rho_{BN} = 1.02\ g/cm^3$) and iodine (M_I).[171] The weight fraction (W_I) was calculated from the ratio of the mass of iodine (M_I) in a given volume to the total mass of the breast tissue-iodine mixture (M_{Total}), resulting in $W_I = M_I / M_{Total}$.

The adjusted density (ρ_{BI})) was then estimated through a weighted average, reflecting the volume contributions of both iodine and the breast tissue. This was calculated as $\rho_{BI} = (1 - V_I) \times \rho_{BN} + V_I \times \rho_I$ where $V_I = \frac{C_I}{\rho_I}$ represented the proportion of iodine in the tissue.

For this analysis, initially a 1.5 mm aluminum filter was used, as per the default configuration. Subsequently, the performance with a copper filter was evaluated with it having thicknesses ranging from 0.05 mm to 0.4 mm with a 0.025 mm step.

The Modulation Transfer Function (MTF), large area signal (L_{Signal}), and Normalized Noise Power Spectrum ($NNPS$) were estimated for the breast without iodine, denoted as MTF_{BN}, $L_{signal_{BN}}$, and $NNPS_{BN}$ respectively, and for the breast with iodine, denoted as MTF_{BI}, $L_{signal_{BI}}$, and $NNPS_{BI}$.

Given that the differences between the breast with and without iodine for MTF were minimal ($MTF_{diff} < 0.1\%$), it was assumed that:

$$MTF = MTF_{BN} = MTF_{BI} \tag{4.16}$$

The $NNPS$ was calculated as the sum of the $NNPS$ values for the breast without and with iodine:

$$NNPS = NNPS_{BN} + NNPS_{BI} \tag{4. 17}$$

The change in the signal ($\Delta Signal$) due to iodine was calculated as:

$$\Delta Signal = L_{signal_{BI}} - L_{signal_{BN}} \tag{4. 18}$$

A task was modeled to detect a disk with a 5 mm diameter. This is represented as:

$$W_{Task} = 2\pi \times r \times sinc\,(2\pi \times f \times r) \tag{4. 19}$$

where the Fourier transform of a disk is approximated by a sinc function in 1D for simplicity, with being r the radius of the disk. Finally, the detectability index d' was calculated as the figure of merit along the spatial frequency axis u up to the Nyquist frequency (u), as given by:[156]

$$d'^2 = \int_0^{u_{Nyq}} \frac{(MTF(u) \times \Delta Signal)^2}{NNPS(u)} W_{Task}^2(u)\, du \tag{4. 20}$$

The analysis was subsequently performed with the tube voltage set to 55 kV, 60 kV, and 65 kV, the allowable tube voltage levels of the bCT system as described in Section 2.1. The detectability index obtained using the default aluminum filtration was then compared to the maximum d' achieved with the copper filter.

3 Results

3.1 Model parameters

Table 4.1 lists the parameters used for the setup and tuning of the model. This table includes basic physical units, details on the geometry of the breast CT system, and operating parameters for the detector.

Table 4.1: Summary of terms and symbols and their corresponding values used in the parallel-cascaded model.

Nomenclature	Notation	Value	Ref.
CsI:Tl nominal thickness	t_{CsI}	0.7 mm	-
CsI density	ρ_{CsI}	4.91 g/cm^3	129
Fractional weight of Cs in CsI	w_{Cs}	0.51155	129
Fractional weight of I in CsI	w_I	0.48845	129
Packing factor	PF_{CsI}	0.72	163
K-edge energy	E_K	35 keV	153
K-fluorescence probability	ξ	0.83	153
K-fluorescent yield	ω	0.87	153
Work function	m_0	55.6 optical photons/keV	153
Quantum detection efficiency	$\bar{g}_1$	0.9652	-
K-fluorescence reabsorption	f_K	0.75	-
Coupling efficiency	$\bar{g}_4$	0.59	153
Blurring factor	H	0.15	-
Fill factor	f_{pix}	0.85	-
Pixel pitch	p_{pitch}	0.152 mm	160
Electronic noise	σ_{add}	100 e$^-$ rms	-
Fractional weight of I	W_I	0.0097	-
Breast tissue with iodine density	ρ_{BI}	1.03 g/cm^3	-
Source-detector distance	SDD	950 mm	-
Source-Isocenter distance	SID	600 mm	-

3.2 Air kerma and HVL measurements

The 1st HVL for the 49 kV spectrum with an added filtration of 1.5 mm Al was found to be 1.39 mm Al. After the introduction of the 10 mm Al aluminum plate, the HVL value increased to 3.55 mm Al.

When measurements were performed at 65 kV with additional filtration of 0.257 mm Cu, a 1st HVL of 4.47 mm Al was found. Then, upon introducing the 10 mm aluminum plate, the value rose to 5.87 mm Al.

The air kerma values measured for 49 kV and 65 kV are presented in Figure 4.3.

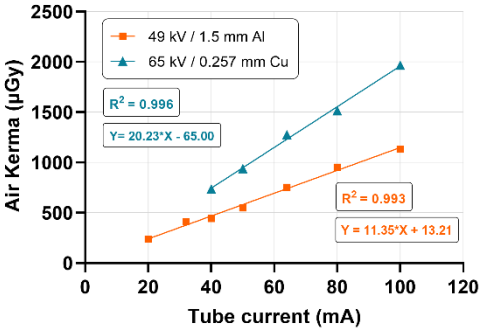

Figure 4.3: Air kerma measurements for two distinct x-ray tube settings. For the first setting at 49 kV with a 1.5 mm Al filter measured air kerma values were 238, 410, 442, 548, 750, 952, and 1132 µGy, while the second setting at 65 kV with a 0.257 mm Cu filter yielded values of 736, 939, 1276, 1515, and 1967 µGy. Linear regression analysis shows R^2 values at 0.993 and 0.996, respectively. The fitting parameters are Y = 11.35X + 13.21 for 49 kV/1.5 mm Al, and Y = 20.23X – 65.00 for 65 kV/0.257 mm Cu.

3.3 Validation at 49 kV

3.3.1 MTF at 49 kV

Figure 4.4 shows the presampled MTF measured at the detector at 49 kV, as outlined in Section 2.2.1, alongside the presampled MTF predicted by the implemented model. Analyzing the differences at two points, 1 cycle/mm and 2 cycles/mm, the calculated errors in percentage were +5.1% and -5.1%, respectively.

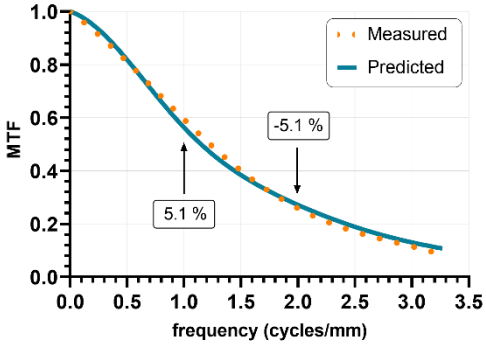

Figure 4.4: bCT-measured at the detector (orange dots) and model-predicted (blue line) MTF plotted as a function of frequency.

3.3.2 NNPS at 49 kV

In Figure 4.5, the NNPS measured at the detector and predicted by the model are shown. The mean CoV (min, max) was 5.3% (3.7%, 8.5%).

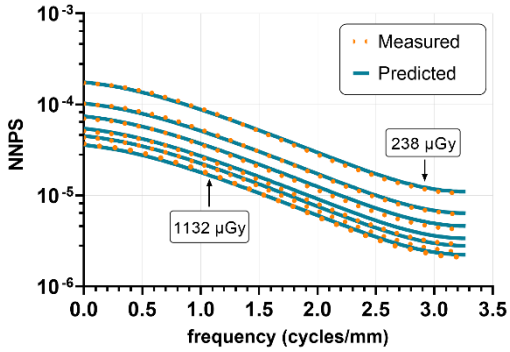

Figure 4.5: bCT-measured at the detector (orange dots) and model-predicted (blue line) NNPS plotted as a function of frequency. From top to bottom the curves correspond to the air kerma measurements of 238, 410, 548, 750, 952, and 1132 µGy.

3.4 Validation at 65 kV

3.4.1 MTF at 65 kV

Figure 4.6 shows the measured at the detector and modeled presampled MTF at 65 kV. The calculated errors at 1 cycle/mm and 2 cycles/mm were -0.8% and -3.2%.

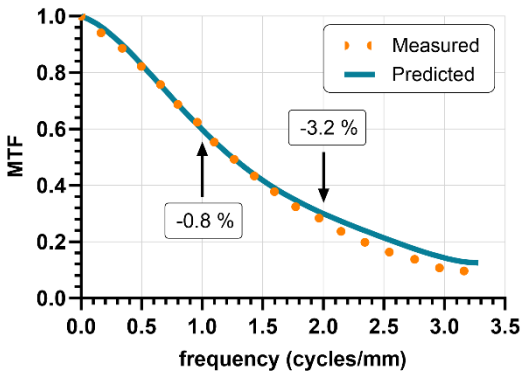

Figure 4.6: MTF bCT-measured at the detector (orange dots) and model-predicted (blue line) plotted as a function of frequency.

3.4.2 NNPS at 65 kV

Figure 4.7 shows the bCT-measured at the detector and model-predicted NNPS. The computed mean value of the CoV was 13.1%, with a minimum and maximum of 11.4% and 16.9% respectively.

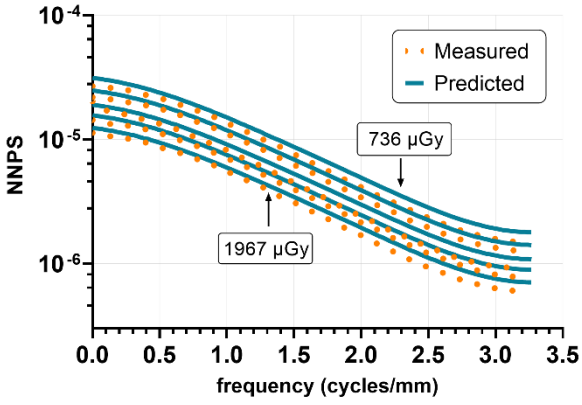

Figure 4.7: bCT-measured at the detector (orange dots) and model-predicted (blue line) NNPS plotted as a function of frequency. From top to bottom the curves correspond to the air kerma measurements of 736, 939, 1276, 1515, and 1967 µGy.

3.5 Detectability index

The maximum iodine-detection d' was found to be when using an additional copper filtration 0.4 mm thick at 65 kV. However, the current required for the protocol of interest would exceed the system's power limitations (7 kW). Therefore, the optimum value was determined to be 0.25 mm of Cu. Figure 4.8 highlights the balance between d' and power consumption across varying copper thicknesses. For ease of comparison, the d' values are shown normalized to the maximum d'. The graph demonstrates a progressive improvement in d' with increasing copper filter thickness. This trend implies a sensitivity of d' to changes in filter thickness, where a greater thickness correlates with an enhanced d'.

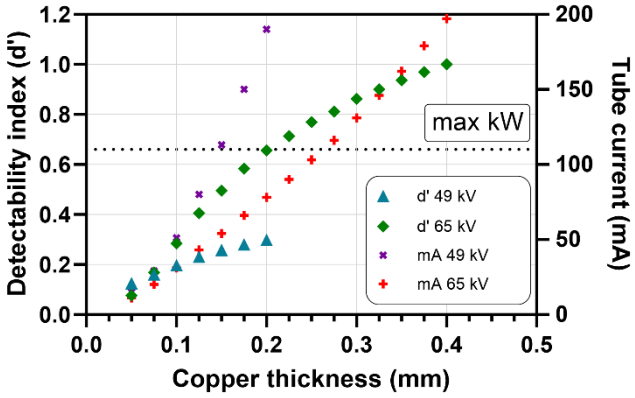

Figure 4.8: Scatter plot illustrating the relationship between copper thickness and the detectability index (d') as well as the required tube current (mA) for the two voltage settings, 49 kV and 65 kV. Blue triangles and green diamonds represent the d' values at 49 kV and 65 kV, respectively. Purple and red crosses correspond to the tube current values at the respective voltage settings. The dotted line indicates the system's maximum power threshold ("max kW") at 65 kV.

At voltage settings of 49 kV and 55 kV, copper filtration outperformed 1.5 mm aluminum filtration. However, the system's power limitations restricted the maximum d'. At 60 kV, the highest d' was found at 0.225 mm Cu, but it was 19% lower than the observed at 65 kV/0.25 mm Cu.

When comparing the d' obtained for the default 1.5 mm aluminum filtration, the performance of the 65 kV/0.25 mm copper filter technique exceeds that obtained with 49 kV/1.5 mm Al and 65 kV/1.5 mm Al by 90% and 74%, respectively.

4 Discussion

In this work, a parallel-cascaded model to characterize a state-of-the-art dedicated bCT system was implemented. The model allowed to derive the spatial frequency-dependent MTF and NNPS in the projection domain. The model predictions were validated with the aim of advancing 4D DCE-bCT and showed good agreement with measurements. Specifically, the discrepancies between the *MTF*s measured at the detector and those predicted by the model were approximately 5% at 49 kV and less than 5% at 65 kV. These results align with existing literature, as reported by Cao et al.[153] and Sheth et al.[154]

The model-predicted $NNPS$ differed from the measured values by approximately 5% at 49 kV in terms of CoV. At 65 kV, however, the CoV rose to around 15%, likely due to the blurring factor being optimized for the default 49 kV tube voltage. This discrepancy is most evident at the tails of the $NNPS$ curve, as seen in Figure 4.7. Future research could focus on optimizing a tube-voltage dependent blurring factor. The choice to utilize 49 kV with a 1.5 mm Al filter (default setting) and 65 kV with a 0.257 mm Cu filter was based on the evaluation of the x-ray tube's voltage range and the model's performance with different filtration.

The model is highly sensitive to even minor fluctuations in the output of number of photons, making it crucial to use measured input values rather than nominal values and a full stack of projections for $NNPS$ measurements. This minimizes inconsistencies when comparing bCT-measured signals with model predictions given that the model assumes uniform behavior across projections. This premise could be undermined by variability in air kerma output between projections of the same scan.

Prior studies have made similar validation comparisons for cone-beam CT[151-154] and CMOS detectors,[153,154] with our results being consistent with those findings. Additionally, similar comparisons have been specifically performed for low-exposure values.[140,147] The results obtained are comparable to those published previously. Nevertheless, the distinct nature of the modeled systems, which are characterized by different components and input parameters, hinders direct comparisons between the curves representing spatial-frequency-dependent descriptors.

The calculation of the Normalized Noise Power Spectrum ($NNPS$) in our study, which entails summing the $NNPS$ values for breast tissue both with and without iodine, draws on methodologies from Richard et al.'s work on dual-energy imaging systems.[143] This approach, which adopts a subtraction factor (w_s) of 1, is consistent

with the optimization principles detailed in their analysis.[172,173] Additionally, it is important to clarify that our model does not incorporate anatomic noise. This means that our study employs a simplified approach in which a perfect alignment between the pre- and post-contrast images is achieved, resulting in complete removal of non-enhanced anatomic noise.

Furthermore, we recognize that the possible presence of background parenchymal enhancement (BPE) would introduce an additional background iodine signal during contrast-enhanced breast imaging.[174,175] However, a spectral optimization as proposed in this study cannot distinguish the iodine signal uptake by a lesion from one in the parenchyma. Therefore, the findings here should be interpreted as an optimization, in the projection domain, of the detectability of iodine, not necessarily of an iodine-containing lesion. As evaluated by Day and Tanguay, BPE can significantly impact detectability, with reductions of up to 40% reported under certain conditions, depending on system and technique parameters.[176,177]

In this study, $\Delta Signal$, which measures the change in signal intensity due to iodine contrast, is adopted for a focused analysis of the contrast agent's effect. This approach enables the isolation of iodine's specific contribution to the overall signal, thereby offering a direct measure of contrast enhancement. The integration of $\Delta Signal$ with the MTF and $NNPS$, both fundamental to the frequency domain, streamlined the analysis, eliminating the need to transform the large area signal ($\Delta Signal$) from spatial to frequency domain.

The detectability index results helped determine the optimal tube voltage and filtering parameters for iodine detection using the evaluated bCT system.

These findings align with prior studies that optimized a bCT system with a different geometry and detector from those in the current investigation. Prionas et al. assessed six tube voltages (50, 60, 70, 80, 90, and 100 kV) and three different filters (0.2 mm Cu, 0.2 mm Sn, and 1.5 mm Al). They concluded that iodine contrast enhancement was optimized at 60 kV using a 0.2 mm Cu filter.[155] The differences between the values in this study and prior work are minimal; no detectability drop related to voltage was noted at 60 kV or 65 kV. Subsequently, Hernandez et al. found that a decrease in the signal-to-noise ratio with increasing tube voltage was significant only at 70 kV when using 0.2 mm Cu; 50 kV and 60 kV showed no notable difference.[156]

In separate studies, various materials were evaluated, and it was concluded that a 0.3 mm gadolinium filter would be a superior candidate to copper, surpassing

its performance for iodine detection due to the K-edge at 50.2 keV. Despite gadolinium's advantages, copper's comparable performance, widespread availability, lower x-ray tube current requirements, and reduced manufacturing costs make it a good option for 4D DCE-bCT.[156,157]

Optimizing filter materials in the projection domain aims to enhance 3D reconstruction quality by providing high-quality inputs under the premise that any subsequent reconstruction method would be able to start from an optimized input.[178] However, this domain's insights might not capture all aspects of the 3D reconstruction process.[179] As a result, the benefits seen in 2D image quality from such optimizations do not guarantee similar improvements in 3D reconstructions. This highlights the need for in-depth research into the effects of projection domain optimizations on 3D image quality in 4D DCE-bCT.

Moreover, the model was developed to work under default exposure time conditions, i.e., a 5 ms pulse width with a 10-second scan time. The study did not investigate the effects of varying these parameters, leaving that for future research. An additional constraint within this study is that our findings are applicable to the specific system under evaluation. It is plausible that variations among seemingly identical systems, particularly in relation to input factors, may lead to disparities in subsequent outputs or results.

5 Conclusion

A parallel-cascaded model was developed to characterize the response of a dedicated bCT system. The model demonstrated reasonable agreement with bCT measurements in predicting the system response, enabling efficient parameter optimization for 4D DCE-bCT development. The model highlights copper's practicality, though caution is warranted in extending 2D optimizations to more complex imaging.

5 4D Breast CT: Phantom-Based Reconstruction Optimization for Iodine Quantification

Original title: 4D Dynamic contrast-enhanced breast CT: Phantom-based reconstruction parameter optimization for iodine quantification

Juan J. Pautasso, Mikhail Mikerov, Liselot C. Goris, Koen Michielsen, and Ioannis Sechopoulos

Published in Medical Physics 2025;52(4):2212-2223. https://doi.org/10.1002/mp.17658

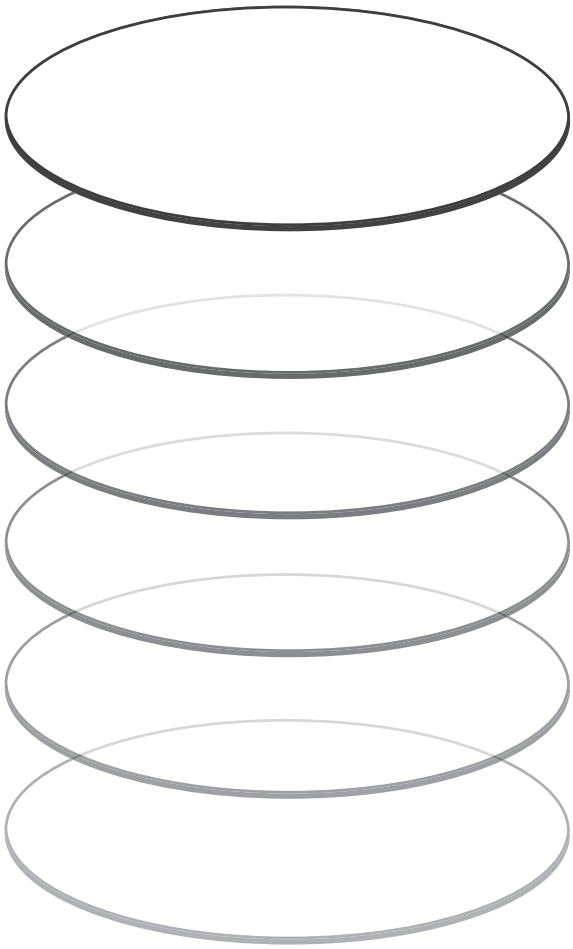

Abstract

Background

Four-dimensional dynamic contrast-enhanced breast CT (4D DCE-bCT) offers promising high-resolution spatial and temporal imaging capabilities for the characterization and monitoring of breast tumors. However, the optimal combination of parameters for iodine quantification in image space remains to be determined.

Purpose

This study aims to optimize a dedicated bCT system to perform long dynamic contrast-enhanced scans with high spatio-temporal resolution while maintaining a reasonable radiation dose.

Methods

Our protocol includes the acquisition of a high-quality prior image that is reconstructed with a polychromatic iterative algorithm (IMPACT). The acquisition of the post-contrast sequence is continuous but sparse and these images are reconstructed using prior image constrained compressed sensing (PICCS). A four-step optimization process is performed using images of a physical phantom. First, the optimal tube current is selected by taking the noise level into account. Second, the optimal number of angles is selected based on the absence of streak artifacts. Third, the number of iterations in IMPACT is specified at the lowest value that achieves the highest spatial resolution. Finally, the number of iterations in PICCS is determined based on the quantitative accuracy of a range of iodine concentrations.

Results

When a high-quality prior image is available, the imaging of post-contrast images can be performed using just 40 projection angles with a tube current of 32 mA. The noise level in the post-contrast images is inherited from the prior image and no streak artifacts are visible. Mean difference between the linear attenuation coefficients of samples containing iodine reconstructed with IMPACT using all 360 projections and PICCS using 40 projections is 0.0004 mm^{-1} at most. The spatial resolution of images reconstructed with PICCS is lower than the one of IMPACT images and is concentration dependent. The cut-off frequency at 10% modulation transfer function drops from 1.55 mm^{-1} in the prior image to 0.9 mm^{-1} when the target with the largest concentration is evaluated. The total mean glandular dose of the protocol does not exceed 22.5 mGy.

Conclusion

This study found the optimal acquisition and reconstruction parameters for a low-dose dynamic contrast-enhanced bCT protocol. The numerical accuracy of the proposed protocol was ensured by performing a physical phantom study.

1 Introduction

Around 16% of all cancer deaths among women are due to breast cancer, resulting in an estimated 685 000 deaths in 2020 worldwide. This problem is only growing, with breast cancer being predicted to take more than 1 million lives in 2040.[2] Screening programs have already enabled early detection and diagnosis of breast cancer, thereby increasing positive treatment outcomes.[180] After diagnosis, some women first undergo neoadjuvant therapy to reduce tumor size, followed by breast conserving therapy. Cases where neoadjuvant therapy leads to pathologically complete response are correlated with both outcome and survival rates improvements.[181-185] In these cases it might even be possible to eliminate surgical treatment.[186,187]

Currently, neoadjuvant treatment is less efficient because it is rarely personalized due to limited availability of suitable imaging modalities. However, dynamic perfusion imaging may provide the necessary functional information to personalize treatment. This raises the importance of accurate quantification of the contrast agent concentration throughout the tumor over time, regardless of the breast shape, size, or composition.

Dynamic contrast–enhanced magnetic resonance imaging (DCE–MRI) and dedicated breast CT (bCT) are both suitable modalities for functional imaging. DCE–MRI with gadolinium contrast agents is already an established modality in breast imaging,[188] while the feasibility of DCE imaging in bCT has only been shown on digital phantoms.[89] However, bCT offers several advantages over MRI, such as better uniformity, higher spatial and temporal resolution, and the ability to depict calcifications and to provide quantitative results. Iodine is a well suited contrast agent for bCT because of its K-edge energy of 33.2 keV, which enables the use of x-ray spectra with lower average x-ray energy to increase contrast between adipose and fibro–glandular tissues.

The most straightforward way to obtain the iodine uptake and wash-out curves is temporal subtraction imaging. The idea of this method is that when two images are subtracted from each other, the difference is solely explained by the change in the iodine concentration between the two acquisitions. Although one can use regular setups for anatomic imaging with already existing reconstruction methods, patient exposure becomes the limiting factor for this approach. Specifically, all images in the sequence must be acquired at high dose with densely-sampled projections to minimize the artifacts and noise in the difference images. High dose limits the applicability of this method for sequences with high temporal resolution, as it negatively affects both the patient and can lead to overheating of the x-ray tube.

Alternatively, multi-energy acquisition protocols could be employed, where, depending on the setup, iodine concentration estimation can be achieved without patient motion artifacts. However, quantitatively accurate reconstruction of iodine distribution in multi-energy bCT is challenging due to several factors, such as sparse and spatially misaligned projections in half-cone beam geometry in the cone-angle direction. For example, the number of projections during one whole revolution of bCT typically ranges from 225 to 500.[42] This number is further split between each spectrum if the multi–energy mode of operation is achieved by spectrum switching.

Thus, any reconstruction that requires material decomposition in the projection domain is not possible without interpolation over a large angular range of missing data.[189] On the other hand, methods based on decomposition in the image domain will need to handle any artifacts that are introduced due to the reconstruction of sparse data. Furthermore, methods that perform direct decomposition are limited to a maximum of two base materials in the most commonly used double-energy setups, with a third base material with K–edge possible given sufficient spectral separation around the K-edge energy. Although, this limitation is tolerated when three base materials are different, e.g., bone, soft tissue, and iodine, it is not sufficiently accurate for breast imaging, where it becomes important to distinguish between similar tissues such as blood, adipose, and glandular, especially when they are combined with low concentrations of iodine.

In the future, multi-binned photon-counting detectors could enable the use of advanced models of attenuation to provide accurate quantitative results. However, to the best of our knowledge, photon-counting CT currently uses no more than two bins at the time of writing this work, and is limited to use in spiral bCT due to the high cost of these detectors.

Prior image constrained compressed sensing (PICCS) sets itself apart from the above mentioned methods as a well suited technique for tracking of the contrast agent in bCT.[190] Briefly, this method uses a high quality prior image to then allow reconstruction of subsequent images from severely undersampled data of the same anatomy under the assumption that only minor changes are present that can be captured through compressed sensing. Although PICCS faces challenges with patient motion when applied in long dynamic scan sequences, it enables low-dose imaging with high temporal resolution and accurate quantification of the contrast agent using a single spectrum.

In this work we aim to determine the optimal data acquisition settings and reconstruction parameters for accurate iodine quantification in 4D dynamic contrast-

enhanced bCT (4D DCE-bCT) using PICCS. We performed an extensive physical phantom study to quantify the influence of dose, number of projections, and number of iterations in iterative methods on the accuracy of iodine quantification.

2 Material and methods

2.1 DCE-bCT imaging protocol

A bCT system (Vera, Koning Corp, Norcross, GA, USA) was modified to perform multiple scan sequences, each up to 100 s in duration. The system is equipped with a pulsed x-ray tube and a flat-panel detector (FPD) mounted on a rotating gantry. The x-ray tube (M-1581, Varian Medical Systems, Salt Lake City, UT, USA) can generate spectra with voltages between 49 and 65 kV, tube currents between 32 mA and 160 mA, and pulse durations between 5 and 8 ms in the current realization of the bCT. The FPD, a CMOS-based Xineos 3030HS (Teledyne Dalsa, Waterloo, ON, Canada), possesses a 0.152 mm pixel pitch and a 0.700 mm thick CsI:Tl columnar scintillator. The geometry of the system places the source 950 mm from the detector and 600 mm from the isocenter. The FPD can be shifted laterally to increase the field of view, but this option is not used in our setup since the detector is large enough for the vast majority of breasts encountered in our clinic and this allows higher temporal resolution since complete angular sampling is reached after a half rotation plus fan-angle instead of a full rotation.

The scan protocol we aim to optimize is intended for patients with a known lesion to be characterized and follows the general concept of the protocol introduced by Prionas *et al.*[47] The main difference is that instead of four post-contrast images in the original protocol, we aim to have continuous acquisitions over 300 seconds. The protocol starts with a pre-contrast scan of the contralateral breast. Afterward, the patient is repositioned and the pre-contrast scan of the ipsilateral breast is made. The long post-contrast imaging sequence of the ipsilateral breast begins immediately after contrast injection to ensure the wash-in is captured. This sequence consists of two or three 100 seconds long individual scans during which the projections are acquired continuously while the gantry rotates at 0.1 Hz, resulting in 10 full revolutions and 20 independently-reconstructed post-contrast images per 100-second scan, with half rotation overlap between each time-point. Finally, the patient is repositioned once more to perform a late-phase contrast-enhanced scan of the contralateral breast.

For the imaging of the contralateral breast we will use temporal subtraction with registration as developed by Gazi *et al*.[50] The reconstruction of the ipsilateral dynamic image sequence is described in section 2.2.

2.2 Reconstruction of 4D sequence

We reconstruct post-contrast images using the PICCS method. This algorithm consists of two steps. To begin with, a high-quality artifact-free prior image needs to be reconstructed. This image is acquired before the administration of the contrast agent. It is always preferable to acquire this image at the highest possible exposure with densely sampled projections and without any patient motion, to maximize the chances that the prior image is not affected by artifacts, has good spatial resolution, and is ideally close to being piece-wise constant. Following that, each post-contrast image in the sequence is reconstructed from severely undersampled projection data acquired at lower exposure levels using the high-quality prior to guide the reconstruction. Under the assumption that only a small fraction of voxels in the post-contrast image is different from the corresponding voxels in the high-quality prior image, their attenuation values can be estimated even from undersampled data by enforcing data sparsity.

2.2.1 Reconstruction of the prior image

We use the iterative maximum-likelihood polychromatic algorithm for CT (IMPACT) to obtain the prior image.[191] IMPACT is a single-energy polychromatic reconstruction method, which enables reconstruction of the image without cupping and metal artifact if the list of base materials is chosen appropriately for the imaged anatomy. IMPACT performs the tissue decomposition into a weighted sum of the energy-dependent contributions due to photoelectric effect $\Phi\,(e)$ given by Braggs-Pierce power law and Compton scatter $\Theta\,(e)$ given by the Klein-Nishina equation:

$$\mu_j(e) = \phi_j \cdot \Phi\,(e) + \theta_j \cdot \Theta\,(e) \tag{5.1}$$

At first glance, this model has two unknowns for every voxel j, ϕ_j and θ_j, which must be estimated, meaning that two different spectra are needed to solve the reconstruction problem. However, in practice both ϕ_j and θ_j are functions of a common parameter. In the work of De Man *et al.* this was chosen to be linear attenuation at a reference energy of 70 keV, which is appropriate for clinical CT while we use the linear attenuation at 30 keV, which is approximately the average energy in the bCT x-ray spectrum. Figure 5.1 shows the representation of the contributions of both effects as a piece-wise linear function of linear attenuation at 30 keV for typical breast tissues. This data is also available in Table 5.1. Except for the choice of reference energy and base materials, our implementation matches the update step provided in the work of De Man *et al.* exactly.

Table 5.1: Decomposition of the linear attenuation coefficient according to equation 5.1 for tissues present in breast. Iron is included to ensure numerical stability of the reconstruction.

	θ (1/cm)	ϕ (1/cm)	μ_{30keV} (1/cm)
Air	*1.8993e-04*	*8.1078e-05*	*0.0004*
Adipose tissue[171]	*0.1651*	*0.0382*	*0.2907*
Fibro-glandular tissue[171]	*0.1860*	*0.0630*	*0.3748*
Skin[192]	*0.1863*	*0.0709*	*0.3959*
Calcification	*1.1581*	*1.5463*	*5.0015*
Iron	*16.8700*	*19.3133*	*64.3895*

2.2.2 Reconstruction of post-contrast images

PICCS reconstruction can be written as the following minimization problem:

$$argmin_X\ \alpha \left\|\nabla\left(X - X_p\right)\right\|_{l_1} + (1 - \alpha)\|\nabla X\|_{l_1},\ s.t.\ \|\mathbf{A}X - Y\| \leq \epsilon. \tag{5.2}$$

Here, X and X_p are the post-contrast and prior images, respectively; $\mathbf{A}$ is the forward operator, Y is the projection data. Discrete gradient operator ∇ is used as a sparsification transformation. Hyperparameter α can be seen as a control parameter for the smoothness of the image X.

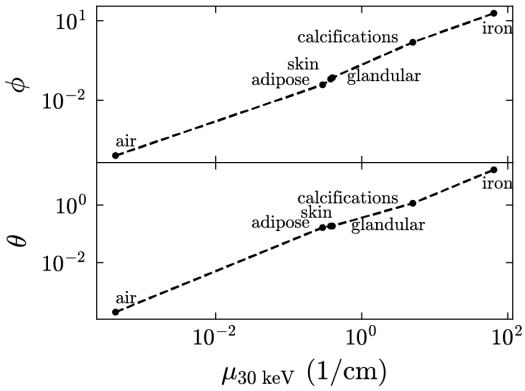

Figure 5.1: Contributions of photoelectric effect and Compton scatter to the total linear attenuation as functions of linear attenuation coefficient at 30 keV. Each combination of two materials is given by a linear equation.

The discrete gradient operator ∇ is chosen so that its application on the difference image sets all unchanged voxel values close to zero and keeps only a small fraction of large values. It is also applied to reduce the influence of a bad prior by enforcing image smoothness. We set $\alpha = 0.92$ to favor accuracy over image smoothness.[193]

In other words, the post-contrast images can have a higher noise level and be affected by sparse reconstruction artifacts, but are expected to provide more accurate quantitative values.

After initialization with the prior image, the reconstruction process is performed iteratively, comprising two alternating main steps in each iteration. First, a single iteration of the IMPACT method is performed to keep the current image estimate consistent with the projection data. Second, a single step is taken to minimize the loss in equation 5.2 using gradient descent with backtracking line search.[193]

2.3 Breast phantom and iodinated contrast sample preparation

Iodine dilutions were prepared from a 300 mg/mL Iomeron (Bracco Imaging, Konstanz, Germany) stock solution, with concentrations ranging from 10 mg/mL to a 0 mg/mL control to mimic a scenario of a 100 kg patient with 5 liter blood volume. In such a case, a 150 mL injection of Iomeron, with a 300 mg/mL concentration, would provide an iodine blood concentration close to 9.0 mg I/mL. This led us to establish 10 mg I/mL as the upper limit for consistency. Each sample volume was adjusted to 50 mL, achieving dilutions from 0.5 to 10 mg I/mL. To ensure accurate and consistent sample volumes, water was initially added to reach 50 mL, then an equivalent volume was replaced with Iomeron stock, enabling precise dilutions and effective mixing. To ensure reproducible phantom positioning, a custom 3D-printed support was developed to hold the 50 mL tube within a conically shaped phantom, which measures 150 mm in height, transitioning from a 120 mm diameter at the top to an 110 mm diameter at the base. This phantom, filled with olive oil, serves to mimic the radiodensity characteristics of adipose tissue (Figure 5.2). Due to the absence of motion, a homogeneous adipose-equivalent phantom is appropriate to study image reconstruction with PICCS since the background image is inherited from high-quality prior image.[193,194] Thus, a phantom with a more complex background that includes features representing fibro-glandular tissue is not needed for this optimization process.

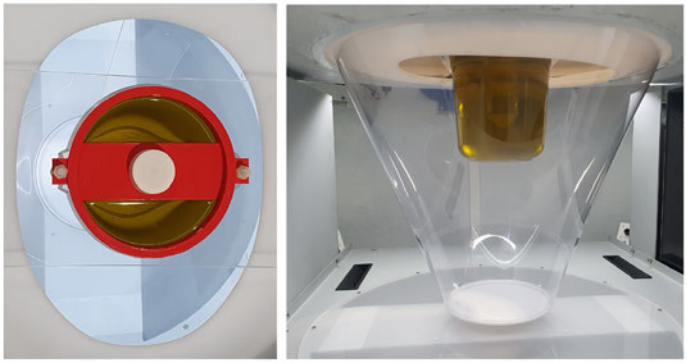

Figure 5.2: Phantom for imaging, including a 50 mL tube with iodine dilution, secured by a 3D-printed holder, all submerged in olive oil.

2.4 Finding the best acquisition and reconstruction parameters

The imaging protocol and reconstruction methods described in the previous sections have several parameters that need to be carefully selected to obtain good image quality and maximize quantitative accuracy. On the image acquisition side, the x-ray spectrum was selected to provide optimal iodine detection in projection domain in our previous work[127] while the tube current and the number of projections per rotation remain to be chosen.

On the image reconstruction side only the number of iterations to reconstruct the prior image and the number of iterations in PICCS need to be set, since in preliminary results it was confirmed, as expected, that tube current (above a minimum) had no impact on the reconstruction quality. These four parameters could be selected sequentially using the following scheme:

1. **Determine the tube current.** We reconstructed the phantom with the 6 mgI/mL target acquired with 60 projections over 360 degrees and at four different tube currents (32/50/64/80 mA) using PICCS. Mean values and standard deviations were calculated inside and outside the target in the ROIs displayed in Figure 5.3 across 20 slices. This approach was based on the premise that demonstrating outcome consistency across settings was crucial, rather than the precision of individual values. Hence, we chose sparse acquisition with 60 projections due to the absence of streak artifacts and predetermined the lowest exposure setting that could be used if outcomes were consistently similar.
2. **Determine the optimal number of angles.** After the optimal exposure per projection was selected, the minimum required number of angles was determined using a method described in 2.6. The phantom with the highest concentration (10 mg I/mL) was used, since from our previous analysis we knew that PICCS performs worse when the difference between the images is large.
3. **Determine the number of iterations in IMPACT**. When reconstructing the prior image, a higher number of iterations will lead to better spatial resolution, but will also increase the noise level if the reconstruction is not regularized. However, noise regularization results in added bias and resolution loss. Because high quantitative accuracy and high resolution are important in this task, noise regularization was not used. The difference in the spatial resolution between reconstructions was given by the modulation transfer function (MTF) in the image domain, which was estimated using the method proposed by Richard *et al*.[195] The number of iterations that leads to the highest cutoff-frequency at 10% MTF while maintaining low noise level was chosen for the final optimization.

4. **Determine the number of iterations in PICCS.** The same analysis was performed to estimate the optimal number of PICCS iterations. However in this analysis, we focused on the convergence of the average value within the target, rather than on the noise level.

Had the sequential optimization not worked as described above, we would have performed a multidimensional sampling of the space of all parameters.

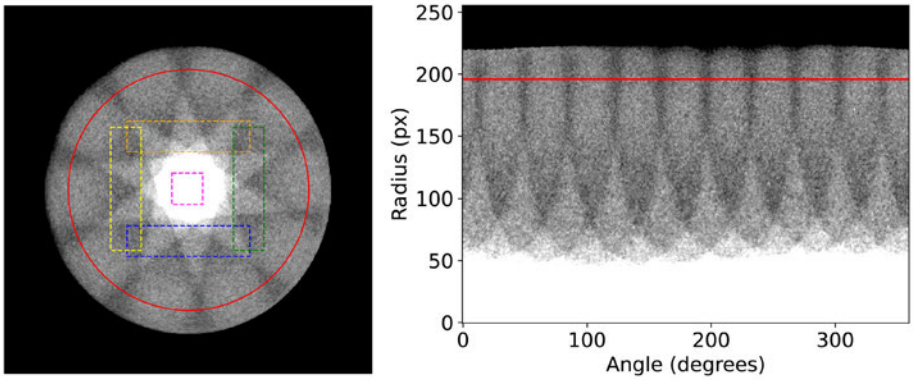

Figure 5.3: Representation of a single slice of the 10 mg I/mL phantom acquired with 10 angles and reconstructed with PICCS in Cartesian and polar coordinates. The data for frequency domain representation was collected along the red line. Ten radial lines attributed to the streak artifacts are clearly visible in both coordinate systems. Rectangular ROIs used to calculate the mean and standard deviation are overlaid on the Cartesian representation. PICCS, prior image constrained compressed sensing.

2.5 Scatter correction

Since the deep learning-based scatter correction method we developed is only valid for patient data,[170] we implemented a dedicated correction for the phantom projection data and note here that this correction is not expected to perform differently from our approach for patient data. The concentration of iodine was the only variable modified; the shape and the location of the phantom remained unchanged. Following reconstruction of a single scan and segmentation of the phantom, primary and scatter projection images were produced using a validated Monte Carlo simulation algorithm.[90] These simulations emulated the bCT's geometry and settings. A 65 kV spectrum with a 0.257 mm Cu filter was modeled, and 10^9 photons were tracked. From the simulation, a set of 360 projections images (1°steps) was generated.

Scatter correction was achieved by subtracting these MC-simulated scatter projections after normalization by the right magnitude from the phantom scans.

2.6 Quantification of the streak artifacts

We developed a quantitative method to estimate the optimal number of projections making use of the radial symmetry of the phantom. The method starts by aligning the geometrical center of the phantom in the center of the 2D matrix. After that, coordinate transformation is applied to represent each 2D slice in polar coordinates system. Then, a line close to the outer border of the phantom is selected and averaged over 40 slices in the z-direction. Finally, we represent this averaged line in the frequency domain, in which each peak corresponds to the frequency of the streak artifacts. We select the angle of projections as a trade-off between the exposure and visibility of the artifacts. Figure 5.3 illustrates the analysis of the phantom with the 10 mg I/mL target.

2.7 Air kerma measurements and dose calculation

To investigate the magnitudes of glandular doses resulting from the acquisition of an image sequence using a 4D DCE-bCT modality, the geometry of the bCT system described in Section 2.1 was replicated using a previously validated Monte Carlo-based algorithm.[44] This algorithm measured radiation captured by a pencil beam (100 mm × 10 mm) situated at the isocenter, with the simulation tracking 10^6 photons. The validation process involved comparing the simulated exposure distribution to empirical measurements obtained at the isocenter using a pencil 100 × 10 mm ion chamber and a Radcal Accu-Gold+ Touch Pro dosimeter.

Following validation, the simulation incorporated breasts of varying sizes, establishing chest wall diameters (CWD) at 10, 12, 14, 16, and 18 cm. The chest-to-nipple distances (CND) were set at 0.5, 0.75, and 1.0 times these diameters, yielding a total of 15 size variations.[196]

Subsequently, the normalized mean glandular dose in mGy per mGy air kerma (DgN) from bCT was calculated, considering a glandular composition of 14.3% by volume.[106] To determine the mean glandular dose delivered to breast, the DgN coefficient is multiplied by the measured air kerma (mGy) at the isocenter for the defined 4D DCE-bCT image sequence.

3 Results

3.1 Optimal exposure level

Figure 5.4 shows the mean values and standard deviations in five regions of the phantom: one inside the iodine-containing sample and four just outside the iodine tube. As expected, the mean value inside the tube in the prior image is lower than in the post-contrast images acquired at various tube currents, since it contains no iodine. It is evident that the tube current has no effect on either the mean value or the standard deviation. Therefore, we proceed with further analysis using only the lowest tube current.

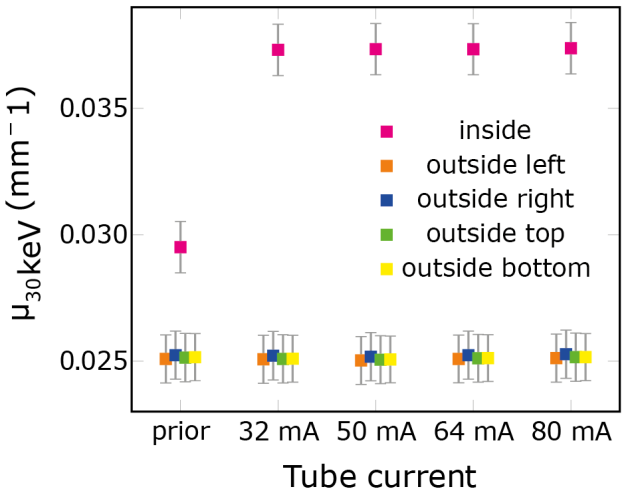

Figure 5.4: Mean attenuation values and standard deviations in five regions of the phantom with 6 mg I/mL insertion.

3.2 Determine optimal number of angles

The frequency-domain representation of the mean value over the angles shown in Figure 5.5 indicates that 40 projections are sufficient to not cause major streaking artifacts. When the number of projections is decreased to 36, the peak at 36° becomes significantly larger than the peak at 40° leading to more visible streak artifacts as depicted in Figure 5.6. Therefore, we continue our further analysis only with 40 projections.

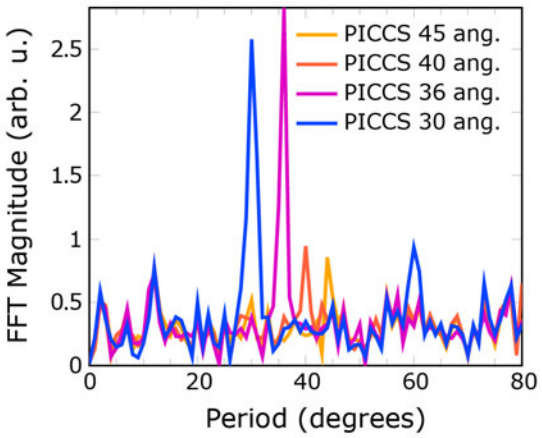

Figure 5.5: Frequency-domain representation of the streak artifacts due to undersampled data acquisition in the image-domain.

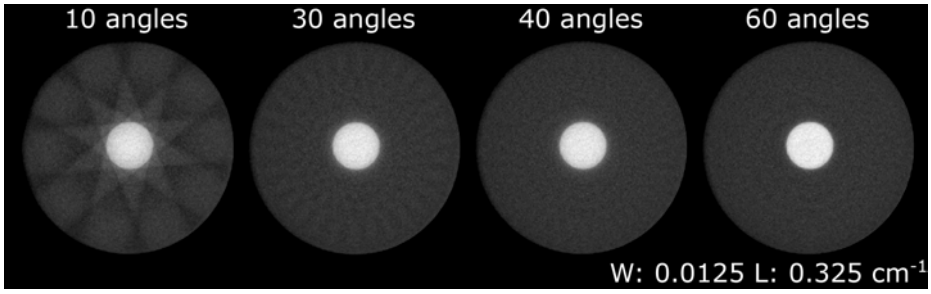

Figure 5.6: PICCS reconstruction of the phantom with 10 mg I/mL acquired with different number of angles. PICCS, prior image constrained compressed sensing.

3.3 Optimal number of iterations to reconstruct the prior image

Figure 5.7 shows the radially-averaged edge profile of the tube filled with water in the image domain. We clearly see that the sharpness increases with higher number of iterations. Values near the center of the tube have larger spread due to the oversampling nature of the method. The standard deviation becomes larger with higher number of iterations as the noise increases. Therefore, only the range from 10 mm to 18 mm was used to calculate the MTF that is shown in Figure 5.8. The MTF plot supports the conclusion that better spatial resolution is achieved when the number of iterations is higher. Furthermore, in order to provide the decision based on a numerical value, we plotted the standard deviation outside the phantom and cutoff-frequency, at which MTF falls to 10%, as a function of the number of iterations. From Figure 5.9 we conclude that 60 IMPACT iterations will be sufficient,

as the benefits of having lower noise outweigh slightly better spatial resolution. Figure 5.10 provides visual confirmation that higher number of iterations leads to better spatial resolution but also increases the noise level.

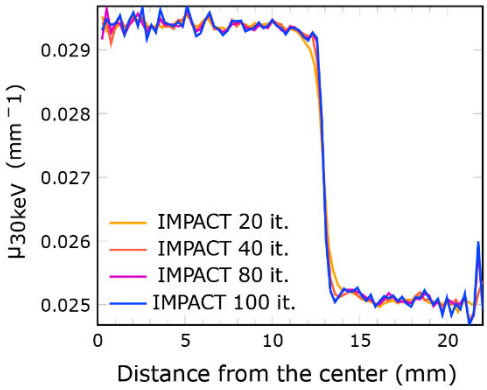

Figure 5.7: Average edge-profile of the tube with water in the image domain reconstructed for various number of iterations.

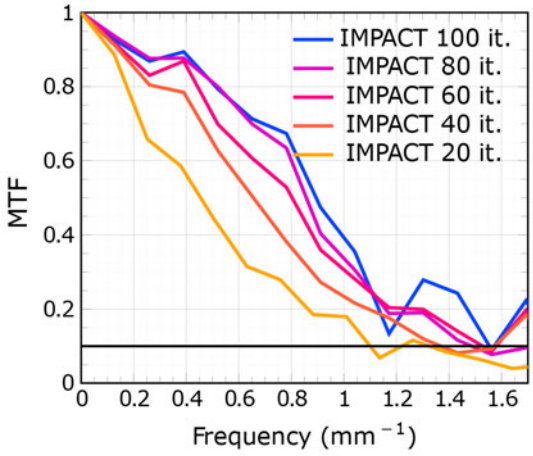

Figure 5.8: Image-domain MTF of the reconstruction of the prior image for various number of iterations.

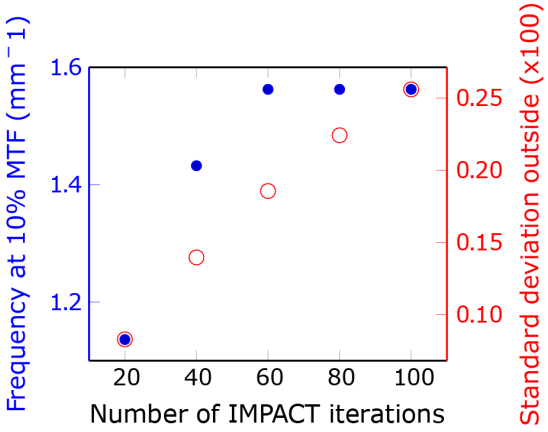

Figure 5.9: Spatial resolution and noise level as a function of the number of iterations when reconstructing the prior image.

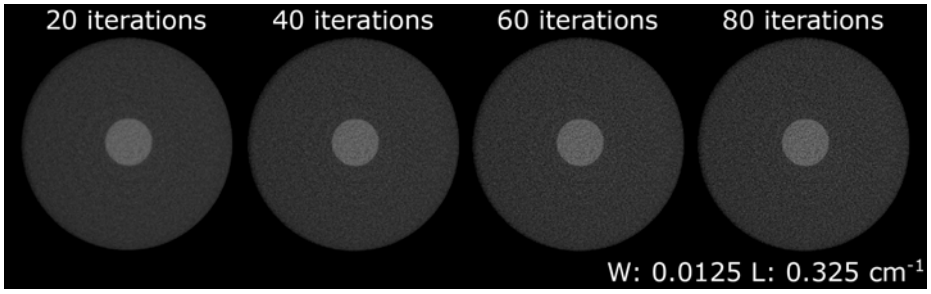

Figure 5.10: Reconstruction of the prior image with increasing number of iterations.

3.4 Optimal number of iterations in PICCS reconstruction

Figure 5.11 visualizes the radially-averaged edge profiles of the tube filled with a 10 mg/mL iodinated solution in the image domain reconstructed with different number of PICCS iterations. It is apparent that a higher number of PICCS iterations is required for the mean value to converge. Moreover, a higher number of iterations also leads to a sharper depiction of the edge. However, the PICCS reconstruction is unable to reach the same spatial resolution as the IMPACT reconstruction of the prior image. Figure 5.12 shows the image-domain MTF of the prior image and the phantom with the highest concentration (10 mg I/mL), the most challenging case for PICCS. We observe significant decrease in the ability to resolve small spatial features.

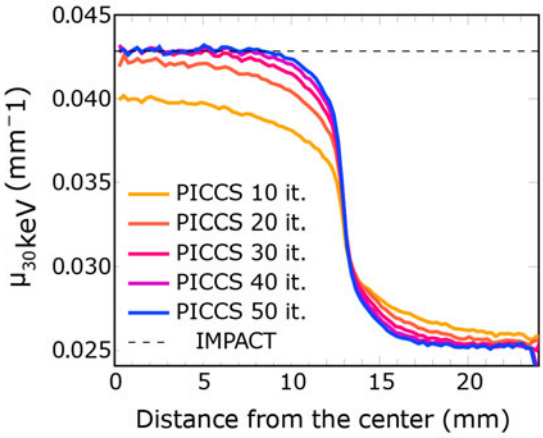

Figure 5.11: Average edge-profile of the tube with 10 mg I/mL in the image-domain reconstructed with various number of PICCS iterations. PICCS, prior image constrained compressed sensing.

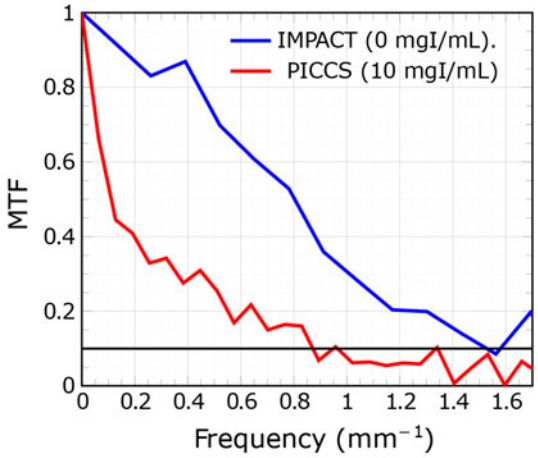

Figure 5.12: Image-domain MTF of the prior image and image of the phantom with 10 mg I/mL target. MTF, modulation transfer function.

3.5 Calibration curves

Figure 5.13 and 5.14 show that the maximum attenuation difference between values obtained with PICCS reconstruction with just 40 angles and IMPACT reconstruction with 360 angles does not exceed 0.0004 mm^{-1}. With the optimized settings, we estimated the calibration curves.

The calibration curve using full reconstruction with IMPACT is

$$\mu_{30keV} = 0.001303 \cdot c + 0.029581 \quad (5.3)$$

While the same calibration curve obtained using PICCS reconstructions with 40 angles is

$$\mu_{30keV} = 0.001331 \cdot c + 0.029553 \tag{5.4}$$

where c is the concentration of iodine. The obtained parameters for the linear fit were compared using ANCOVA and both slopes (p=0.068) and intercepts (p=0.057) were found to not be different between both reconstructions.

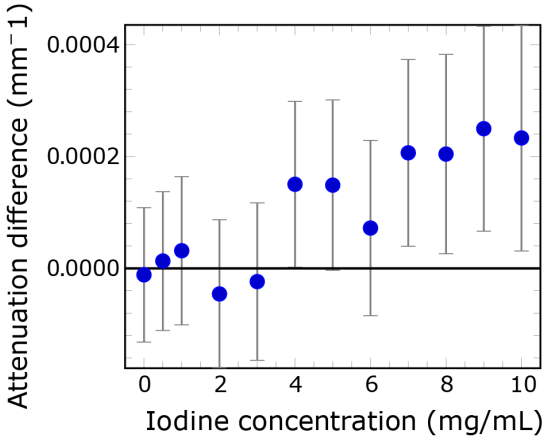

Figure 5.13: Relative difference between the linear attenuation coefficients reconstructed with IMPACT using all 360 projections and PICCS using 40 projections. PICCS, prior image constrained compressed sensing.

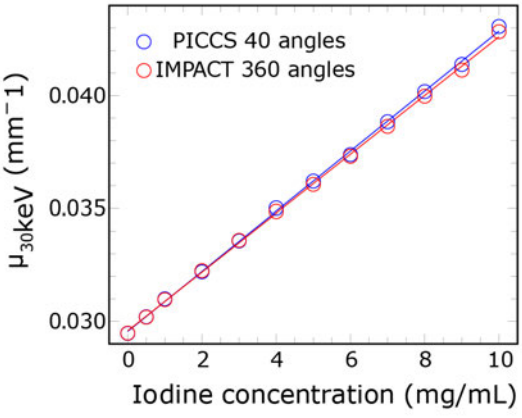

Figure 5.14: Calibration curves using IMPACT reconstructions of data sets with 360 projections and PICCS reconstructions of data sets with 40 projections. PICCS, prior image constrained compressed sensing.

3.6 Obtained air kerma and mean glandular dose

Air kerma measured at the isocenter showed that 360 projections at 65 kV and 80 mA with a 0.257 mm Cu filter resulted in 12.2 mGy, while 40 projections at 32 mA resulted in 0.56 mGy. In Table 5.2, the normalized mean glandular dose (DgN) coefficients for breasts of varying sizes are presented, with a mean value of 0.762 (ranging from a minimum of 0.667 to a maximum of 0.851).

Table 5.2: Normalized mean glandular dose (DgN) coefficients in mGy per mGy of air kerma for breasts of varying sizes, considering a glandularity of 14.3% by volume.

CWD (cm)	CND (cm)	DgN (mGy/mGy)
10	*5*	*0.763*
10	*7.5*	*0.818*
10	*10*	*0.851*
12	*6*	*0.744*
12	*9*	*0.797*
12	*12*	*0.827*
14	*7*	*0.712*
14	*10.5*	*0.772*
14	*14*	*0.801*
16	*8*	*0.686*
16	*12*	*0.746*
16	*16*	*0.775*
18	*9*	*0.667*
18	*13.5*	*0.720*
18	*18*	*0.745*

Note: Air kerma at the isocenter of the bCT system (65 kV/0.257 mm Cu) was taken as reference. Abbreviations: CND, chest-to-nipple distance; CWD, chest wall diameter.

4 Discussion

The goal of this study was to perform the optimization of reconstruction parameters to define a protocol for DCE-bCT. Since the aim is to continuously acquire post-contrast images over a minimum timespan of two minutes, it was important to reduce patient dose and prevent tube overheating. PICCS reconstruction was deemed suitable for this task as it allows image reconstruction from severely undersampled data acquired at low tube currents. However, the quantitative accuracy of the method needed to be ensured.

To begin with, no dependency of the mean value inside the tube and noise level on the tube current could be found. Image noise properties in the post-contrast images reconstructed with PICCS are inherited from the prior image. Thus, the lowest tube current is selected for this protocol.

The minimum and maximum tube currents were determined by the bCT's settings and its 7 kW power capacity, respectively.

Following this, we recommend using 40 projection angles for post-contrast images, even though a lower number of angles can further reduce the dose while still maintaining sufficient image quality for diagnostic or localization purposes. Nevertheless, it will come at the cost of more prominent streak artifacts, which will negatively influence quantitative values.

The air kerma measured at the isocenter showed that 360 projections at 65 kV and 80 mA with a 0.257 mm Cu filter resulted in 12.20 mGy, while 40 projections at 32 mA resulted in 0.56 mGy. From Table 5.2, if an average breast size of 14 cm CWD and 10.5 cm CND is considered, then the mean glandular dose delivered to the breast is equivalent to 9.41 mGy for the pre-contrast phase and 0.43 mGy for the single image in the post-contrast case. During the entire post-contrast phase of 300 seconds, the total mean glandular dose delivered to the patient will be 12.96 mGy.

Next, we wanted to ensure that the degree of enhancement can be quantified, since making longitudinal comparisons throughout neoadjuvant treatment will be beneficial for personalizing and adapting treatment to response. Due to the large variability of breast sizes, shapes, and inner structures, FDK-based methods will suffer from cupping artifacts due to insufficient beam hardening correction. To enable longitudinal comparisons, the images were reconstructed with the iterative IMPACT method. While IMPACT reconstruction combined with scatter correction eliminates beam hardening artifacts, its spatial resolution and noise levels depend on the number of iterations. We determined that 60 iterations offer an optimal balance between spatial resolution and image noise.

Finally, we studied the impact of the number of PICCS iterations on the accuracy of the post-contrast images. In general, the higher the number of PICCS iterations, the more accurate and sharper the images will be. The analysis showed that the spatial resolution of the images reconstructed with PICCS will not reach the spatial resolution of the prior image even when the number of iterations is high. However, this analysis was performed with a very high concentration of 10 mg I/mL as the

worst case scenario, while the iodine concentration in clinical applications is not expected to exceed 6 mg I/mL.[197] In general, the numerical accuracy of images reconstructed with PICCS will decrease with increasing concentration of the contrast agent, due to the difference constraint with the prior image and with smaller size of the perfused anatomy,[198] the latter in our opinion likely due to partial volume effects.

Future work will be dedicated, among other things, to incorporating noise regularization methods in IMPACT and to improving its convergence rate. Additionally, the lower spatial resolution in the post-contrast images compared to prior image, which we identify as the main limitation of the proposed method, must be addressed. Moreover, the influence of intra-scan motion during the acquisition of the prior image and inter-scan motion between different frames needs to be studied as it could not be replicated with the presented phantom. Our approach for reducing inter-scan motion is rigid registration of the post-contrast projections to the corresponding projections of the prior image. This approach should significantly reduce the registration artifacts; in the best-case scenario, only non-rigid motion will remain. The artifacts due to intra-scan motion during the acquisition of the prior image can be reduced using our previously developed non-rigid motion compensation method.[199] An important point to consider is that even though it is able to produce artifact-free images when motion is moderate, there is no control over the final position of the breast image and its geometrical shape. Thus, it could lead to a very different representation of the prior and post-contrast images, limiting the accuracy of the method. Finally, validation on a dynamic phantom with known ground truth is required before the protocol can be applied to scan patients.[200] In terms of phantom design, addition of solid structures representing non-perfused fibro-glandular tissue is necessary to confirm that the background image is fully inherited from high-quality prior image without causing artifacts when using PICCS, but the optimization performed here would most probably not be affected.

5 Conclusion

We propose a protocol for DCE-bCT tailored to provide accurate quantitative values at low dose. With this protocol, the pre-contrast image and a 300 s long sequence of post-contrast images can be acquired at 22.37 mGy.

6 4D Breast CT: Phantom-Based Quantitative Accuracy Evaluation

Original title: Evaluation of quantitative accuracy in 4D DCE-bCT: Insights from a perfusion phantom study

Juan J. Pautasso, Liselot C. Goris, Koen Michielsen, and Ioannis Sechopoulos

In preparation for submission to Medical Physics

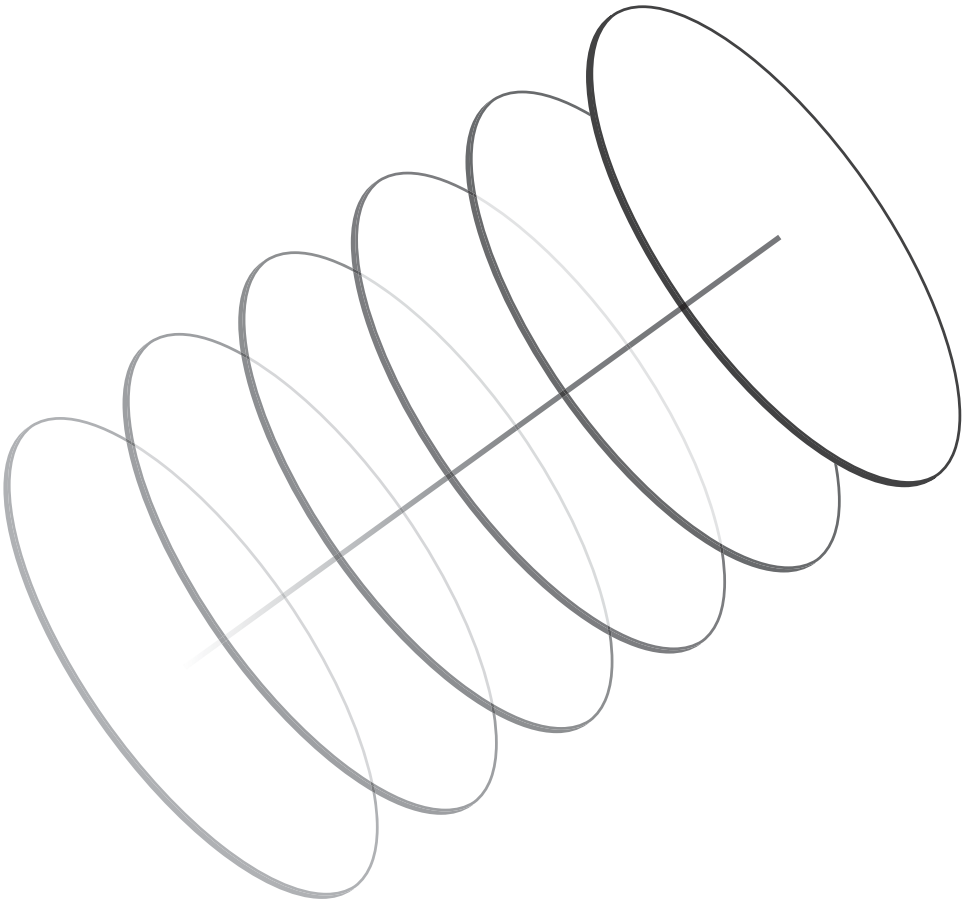

Abstract

Background

Four-dimensional dynamic contrast-enhanced breast CT (4D DCE-bCT) provides submillimeter spatial resolution and temporal sampling within seconds, offering potential for improved perfusion assessment in breast cancer. Its quantitative accuracy, however, must be validated against physical ground truth before clinical use.

Purpose

To experimentally evaluate the accuracy of dynamic iodine concentration quantification in 4D DCE-bCT using a perfusion phantom with in-line optical spectroscopy and ultraviolet-visible (UV/VIS) spectrophotometry as reference standards.

Methods

A dynamic flow phantom with a 3-mm internal diameter was used to approximate the dimensions of tumor-feeding vessels observed during angiogenesis. Potassium iodide (KI)-based contrast was introduced using two injection protocols. The first consisted of block pulses at 1, 3, and 5 mg I/mL to test quantification at discrete dilutions. The second was a gradual inflow-outflow sequence programmed to mimic bolus passage. Transmission at the phantom entrance and exit was measured with an in-line optical spectroscopy system, and discrete fluid samples were collected and analyzed by UV/VIS spectrophotometry to provide reference values.

Dynamic bCT acquisitions were performed using a previously developed sparse-view protocol, consisting of a pre-contrast scan reconstructed with the iterative maximum-likelihood polychromatic algorithm for CT (IMPACT) to serve as the static prior, followed by post-contrast dynamic scans reconstructed with the prior image constrained compressed sensing (PICCS) algorithm. Acquisitions were performed at 65 kV with 0.25 mm Cu filtration, 80 mA for the pre-contrast scan (360 projections over 10 s) and 32 mA for the post-contrast scans (400 projections per 100 s), using 5 ms pulse width. For each acquisition, this prior image was subtracted from post-contrast volumes to suppress the static background.

The tube interior was segmented using fixed thresholding and morphological cleanup, and voxel values were converted to iodine concentration using a calibration curve derived from KI dilutions. Agreement with reference standards was assessed from both peak concentrations and time-concentration profiles. Quantitative errors were expressed as absolute differences from nominal/reference values and as percentage error.

Results

The calibration curve between linear attenuation and iodine concentration was well described by a linear relationship, with a residual standard error of 0.10 mg I/mL. However, denoising by the reconstruction algorithm at very low attenuation introduced larger relative errors near 1 mg I/mL. For block pulse injections, 4D DCE-bCT measured peaks of 0.07 mg I/mL (absolute error 1.00 mg I/mL; 93.5% error) at 1 mg I/mL, 1.92 mg I/mL (error 1.07 mg I/mL; 35.8%) at 3 mg I/mL, and 4.42 mg I/mL (error 0.35 mg I/mL; 7.3%) at 5 mg I/mL.

For the gradual inflow-outflow sequence, the 4D DCE-bCT-derived peak concentration was 5.23 ± 0.62 mg I/mL, in agreement with the UV/VIS reference of 6.07 mg I/mL.

The optical average peaked at 5.26 mg I/mL, slightly lower than UV/VIS, consistent with temporal averaging of the optical signal. Temporal wash-in and wash-out dynamics were also reproduced correctly. Reliable quantification was therefore achieved for concentrations ≥3 mg I/mL, while accuracy at lower levels may have been suppressed as noise and limited by spatial resolution and calibration sensitivity.

Conclusion

4D DCE-bCT accurately quantified dynamic iodine profiles at clinically relevant concentrations above 3 mg I/mL in a 3-mm tube phantom. This emphasized robustness under challenging conditions representative of tumor angiogenesis, while also identifying limitations near the detection threshold. These findings establish the quantitative feasibility of the proposed pipeline and support progression toward studies with more anatomically realistic phantoms and initial clinical evaluation.

1 Introduction

Breast cancer is the most diagnosed cancer and the leading cause of cancer-related deaths among women globally. In 2022, approximately 2.3 million new cases were diagnosed, and around 666,000 deaths were reported.[11] This burden is expected to grow, with both incidence and mortality projected to rise by 2040.[2]

Breast cancer heterogeneity influences cancer progression, treatment outcomes, and prognosis.[201] MRI is currently the gold standard for disease staging and treatment planning, especially in patients undergoing neoadjuvant chemotherapy, since it helps assess treatment response and detect residual disease.[33-35,202] However, MRI has several limitations, including difficulty in detecting calcified structures and limited spatial and temporal resolution for tracking contrast uptake. Additionally, the lack of a standardized measure for tissue characteristics across vendors hampers the consistency of its quantitative analysis.[203]

To address these limitations, Prionas et al. enhanced lesion detection using contrast-enhanced dedicated breast CT (CE-bCT),[47] while Caballo et al. demonstrated the feasibility of 4D dynamic CE-bCT (4D DCE-bCT) for high-resolution functional imaging, particularly for staging, treatment planning, and monitoring.[57] Building on these advancements, a bCT system was optimized for this dynamic contrast-enhanced scanning, with the specific aim of achieving accurate iodine quantitation at high spatio-temporal resolutions, with new reconstruction algorithms developed and the x-ray spectrum refined to enhance iodine concentration quantification.[127,204]

The aim of this study is to experimentally evaluate the quantitative accuracy of dynamic iodine imaging in 4D DCE-bCT using a functional physical phantom on this 4D DCE-bCT-optimized system. Ground truth iodine concentrations were obtained with in-line optical spectroscopy, supported by ultraviolet-visible (UV/VIS) spectrophotometry of collected samples. The simplified phantom minimizes unnecessary complexity while replicating key imaging characteristics, providing a controlled environment to assess the complete 4D DCE-bCT pipeline and verify iodine quantification accuracy.

2 Material and methods

A dedicated breast CT (bCT) system was used to perform 4D dynamic contrast-enhanced imaging of a custom-made breast perfusion phantom. Projection data

were corrected for scatter using Monte Carlo simulations and reconstructed with algorithms optimized for iodine quantification. Iodine concentrations derived from the images were validated against in-line optical spectroscopy and UV/VIS spectrophotometry of collected samples. The experimental and analysis workflow is illustrated in Figure 6.1.

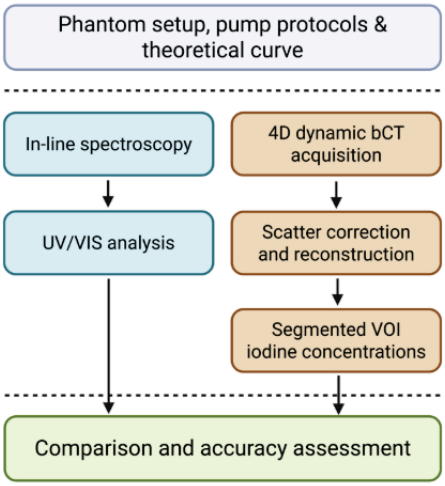

Figure 6.1: Workflow of the experimental setup and analysis for the 4D DCE-bCT phantom study. The process starts with phantom preparation and pump protocol configuration providing the input for the generation of a theoretical curve, followed by two parallel acquisition paths: in-line optical spectroscopy with UV/VIS analysis (left) and 4D DCE-bCT imaging with scatter correction, reconstruction, and VOI segmentation (right). Outputs from both paths are combined for quantitative accuracy assessment of iodine concentration measurements.

2.1 Breast CT system and acquisition parameters

A modified dedicated bCT system (Vera, Koning Corp., Norcross, Georgia, USA) was used for this study. Tube current and exposure were set according to previous work,[127,204] to optimize iodine quantification. Pre-contrast scans were performed using 0.25 mm Cu filtration at 65 kV, 80 mA, and 5 ms pulses.

Post-contrast scans used 65 kV, 32 mA, and 5 ms pulses. The pre-contrast sequence comprised 360 projections over a single revolution in 10 seconds, while post-contrast imaging captured 400 projections over 10 revolutions in 100 seconds for each of the three dynamic phases, covering both wash-in and wash-out, for a total of 1200 projections. There is an inherent 5-second gap between consecutive dynamic phases due to system exposure reset and preparation.

2.2 4D DCE-bCT acquisition and reconstruction

The acquired 4D DCE-bCT projection images were first corrected for scatter using a previously developed Monte Carlo-based method and then reconstructed with the iterative maximum-likelihood polychromatic algorithm for CT (IMPACT) and prior image constrained compressed sensing (PICCS) algorithms.[190,191,204]

For scatter correction, a validated Monte Carlo simulation, previously described,[170] was performed to replicate the geometry and acquisition settings of the bCT system.[44] A single scan was reconstructed and segmented and input into the Monte Carlo simulation to obtain primary and scatter projection estimates. The simulation used a 65 kV x-ray spectrum with 0.25 mm Cu filtration, tracked 10^9 photons, and generated 360 projections at 1° intervals. The resulting simulated scatter projections were scaled to the appropriate magnitude and subtracted from the measured projections.

The IMPACT algorithm extends the classical maximum-likelihood transmission reconstruction (MLTR) approach by modeling x-ray attenuation as the sum of photoelectric and Compton scattering components while only allowing the presence of a predefined number of material combinations as constraint.[191]

PICCS reconstruction[190] was then applied to the scatter-corrected data, using the IMPACT image as a prior. Each time frame was reconstructed from 40 evenly spaced projections spanning 10 seconds, with the time assigned to each frame corresponding to the average time of acquisition of its contributing projections.[204] For each 400-projection phase, this yielded 19 reconstructed time points, each separated by 5 seconds. In between post-contrast phases, the 5-second inter-sequence gap described above results in approximately 15 seconds between the last time point of sequence N and the first time point of sequence N+1. The reconstructed images had an isotropic voxel size of 0.25 mm.

In terms of dose, the static prior acquisition (360 projections at 65 kV, 80 mA, 0.25 mm Cu) delivered 12.2 mGy air kerma at isocenter. Each dynamic frame (40 projections at 32 mA) delivered 0.56 mGy. Using a normalized glandular dose coefficient (DgN) of 0.762 mGy/mGy based on the phantom dimensions, the total mean glandular dose for a full dynamic acquisition was 22.5 mGy.[204]

2.3 Iodine contrast concentration range in breast and tumor tissue

To test the quantitative accuracy of dynamic iodine imaging in 4D DCE-bCT, an appropriate iodine concentration range must be selected. Previous phantom

studies in quantitative contrast-enhanced breast x-ray imaging used iodine concentrations of 0-2 mg I/mL, 0-3 mg I/mL, and 0-5 mg I/mL.[205-210]

Quantitative CT studies in breast cancer patients reported mean iodine concentrations in breast lesions of 1.1 mg I/mL (maximum 1.38 mg I/mL), 2.7 ± 1 mg I/mL (maximum 5.6 mg I/mL) and, 1.9 ± 0.6 (maximum 6 mg I/mL).[197,211,212] Based on these findings, a maximum iodine concentration of 6 mg I/mL was selected to ensure clinical relevance, since this value encompasses the reported lesion concentrations.

2.4 Phantom design

The simplified breast perfusion phantom is modelled after a standard bCT quality control phantom with a maximum diameter of 13 cm (Koning Corp, Norcross, Georgia, USA). To simulate the x-ray attenuation of breast skin, the wall of the phantom is 1.5 mm thick and printed from clear resin material using a 3L SLA printer (Formlabs Inc., Sommerville, Massachusetts, USA).[213] The phantom is filled with olive oil to mimic fatty tissue.[214] The breast-shaped phantom has a total height of 125 mm and a maximal internal diameter of 120 mm, and it is closed with a 3D-printed acrylic lid (Figure 6.2). To avoid tumor-like shapes (e.g., a sphere) acting as chambers and altering the fluid dynamics, a U-shaped inlet tube with an inner diameter of 3 mm and a height of 80 mm is integrated into the lid, with a path length corresponding to a 200 mm perimeter. The outer contour of the phantom has a perimeter of 300 mm.

Figure 6.2: Design and setup of the breast perfusion phantom. The schematic illustrations (left and center) show the phantom's structure and position of components, while the right image displays the actual phantom filled with olive oil to mimic fatty tissue.

2.5 Phantom pumping system

The phantom was connected to a dedicated pumping system comprising three programmable syringe pumps (AL-4000, World Precision Instruments, Hertfordshire, UK): one for contrast input, one for water input, and one for fluid extraction. The system was prefilled with water, and flexible medical-grade tubing (5 mm outer diameter, 3 mm inner diameter, 70 cm length) was used to ensure consistent flow and minimal resistance.

2.6 Optical system for monitoring the iodine concentration in the contrast medium

An in-line optical spectroscopy system, illustrated in Figure 6.3 and previously described, was used to measure the iodine concentrations at the phantom inlet (P1) and outlet (P2) during the dynamic protocols.[200] The measurement cell was modified from earlier prototypes to improve dynamic performance (shown in Appendix A, Figure 6.A1). The updated measurement piece, with a smaller cross-section comparable to the rectangular piece, minimized mixing artifacts and allowed for a more accurate measurement of time-dependent iodine concentrations.

KI was selected as the test contrast medium for its optical detectability and comparable x-ray attenuation to clinical agents. Adjusting for molecular weight differences enables preparation of KI solutions with equivalent iodine concentrations (mg I/mL), making it a suitable substitute for phantom studies.[200]

The optical setup comprised a green LED coupled to a fiber optic cable and collimator to produce a parallel light beam through the measurement cell. A second collimator on the opposite side directed the transmitted light into a fiber optic cable connected to a photodetector.

Before dynamic measurements, calibration curves were obtained by recording transmission values for eight known KI concentrations (0, 0.5, and 1-6 mg I/mL in 1 mg I/mL steps) at both P1 and P2. The concentration and transmission were related by a one-phase decay function, defined as:

$$Y = Plateau + (Y_0 - Plateau) \cdot \exp(-K \cdot X)$$

Function fitting was performed using Prism software (GraphPad Software, Boston, MA, United States). These curves were applied during the experiments to convert measured light intensities into iodine concentrations.[28]

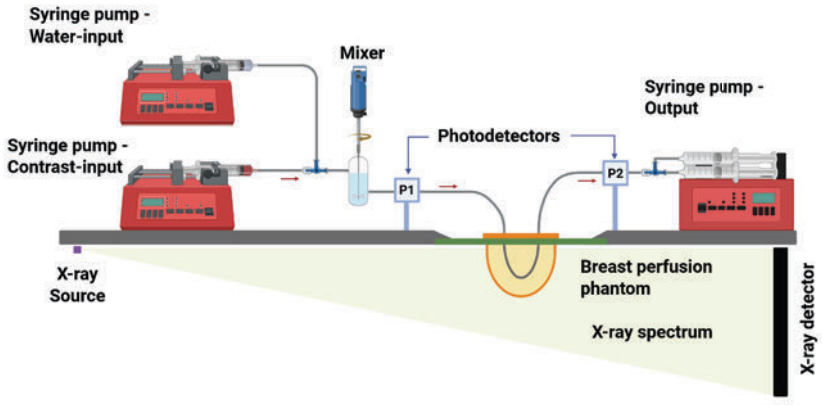

Figure 6.3: Schematic of the phantom pumping system (described in Section 2.5) for dynamic contrast delivery. Photodetectors (P1 and P2) monitor the flow (as described in Section 2.6), and 4D DCE-bCT x-ray imaging captures contrast changes.

2.7 Dynamic measurements

Two types of measurements were conducted to evaluate the quantitative performance of 4D DCE-bCT under different enhancement patterns. The first used discrete, well-defined iodine pulses, allowing direct validation of system accuracy since the exact iodine concentration for each pulse was known. The second used a gradual inflow-outflow protocol designed to mimic physiologically relevant perfusion curves and assess the system's ability to track continuous, gradual changes in iodine concentration over time.

2.7.1 Block pulse protocol

Three block-pulse protocols were acquired, each comprising a 20-second iodine pulse at 24 mL/min, preceded and followed by water to flush the system. Fixed pulse concentrations of 1, 3, and 5 mg I/mL were used. Each protocol was imaged with a single 4D dynamic breast CT sequence as described in Section 2.2, sufficient to capture the entire pulse. Because KI solutions can sediment over time, particularly at higher concentrations, samples from each concentration were collected immediately after acquisition (see Section 2.8).

2.7.2 Gradual inflow-outflow protocol

To generate a gradually increasing and decreasing iodine curve, a 24 mL mixing container was added to the pumping setup, where the contrast and water were mixed before entering the phantom. The pumping program was set to deliver a contrast input of 7.6 mg I/mL at a rate of 24 mL/min for 100 seconds, followed

by 200 seconds of water input at the same rate. This produced a peak intensity of approximately 6 mg I/mL within the first 100 seconds, followed by a decline to near 0 mg I/mL over the subsequent 200 seconds.

The experiment was then repeated twice without 4D DCE-bCT acquisition to allow for fluid sampling and avoid perturbations in the flow that could compromise the in-line optical measurements. Using 3-way valves connected to syringes positioned before the inlet and after the outlet measurement sections, 1 mL samples were collected at the peak input time (140 s) and peak output time (160 s) for subsequent analysis (see Section 2.8). The acquisition timing for the gradual inflow-outflow protocol is shown in Figure 6.4.

2.7.3 Theoretical curves

The variation of iodine concentration in the tubing over time can be estimated from the pump settings and system volumes by solving an ordinary differential equation (ODE).[214] The change in concentration inside the tube, C_{in}, is expressed as:

$$\frac{dC_{in}(t)}{dt} = \frac{s_1 c_1 + s_2 c_2 - Q_{in} C_{in}}{V_{in}}$$

where:

- $Q_{in} = s_1 + s_2$ denotes the combined inflow rate from the two pumps.
- $C_{in}(t)$ is the concentration in the tube at time t.
- $Q_{in} C_{in}$ represents the mass of fluid leaving the tube per unit time.
- c_1 and c_2 are the iodide concentrations of the inputs from pumps 1 and 2, respectively.
- $s_1 c_1 + s_2 c_2$ gives the total mass of the solution entering the tube per unit time.
- V_{in} is the internal volume of the tube, which determines the rate at which concentration changes.
- c_0 is the initial concentration present in the tube before the injection starts.

The ODE can be solved for any timepoint t to reflect different injection rates. Numerical solutions were obtained using the *odeint* function from the *SciPy* integration library (v1.14.0), providing theoretical concentration-time curves.

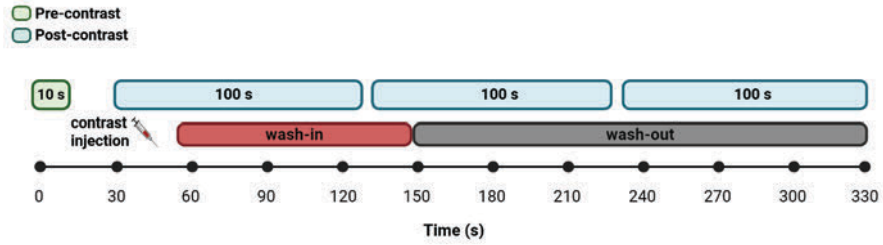

Figure 6.4: Time sequence for the gradual inflow-outflow protocol, consisting of a 10-second pre-contrast scan followed by three consecutive 100-second post-contrast scans (400 projections each) separated by 5-second gaps. Contrast injection began 20 seconds after the start of the first post-contrast phase, with wash-in occurring during this phase, reaching a peak during the second phase and wash-out extending into the subsequent phases.

2.8 Fluid sample extraction and analyses

Samples obtained during the dynamic measurements previously described were analyzed using a UV/VIS spectrophotometer (UV-2600, Shimadzu, Kyoto, Japan) with an accuracy of 0.002 A (equivalent to 6 µg I/mL). Before sample analysis, a calibration curve was established by measuring the absorbance of eight KI solutions with known iodine concentrations (0, 0.5, and 1-6 mg I/mL in 1 mg I/mL steps). A fitted curve was then used to relate absorbance values to iodine concentration. This relationship was then applied to the measured absorbance values of the collected samples to determine their iodine concentrations.

2.9 Calibration for iodine quantification

Calibration samples were prepared by diluting potassium iodide (KI) stock solution with water to obtain concentrations ranging from 0 to 7 mg I/mL. Each dilution was stored in 50 mL tubes and placed in a 3D-printed holder inside the breast phantom filled with olive oil.[204] All samples were scanned and reconstructed as described in Section 2.2 for static prior acquisitions. A water-filled tube (0 mg I/mL) was first acquired and designated as the reference prior. For each iodine dilution, this water prior was subtracted to remove the static background, and a binary mask derived from the water scan was applied to isolate the homogeneous KI region. Voxel values within the mask were averaged per concentration, and linear regression against the known iodine concentrations was used to obtain calibration curves for quantification.

2.10 Segmentation and quantitative analysis

The pre-contrast (prior) reconstruction was loaded as a 3D volume. For each post-contrast acquisition, the prior was subtracted voxel-wise to form a subtracted

volume, which was then cropped to a fixed volume of interest. A binary mask was generated from the prior by slice-wise Gaussian smoothing ($\sigma = 0.5$) and fixed thresholding at 0.26 cm^{-1}. This threshold was selected from the histogram of the prior image (effective energy 35 keV), allowing retention of the tubing and lumen while excluding lower-attenuation background structures.

After thresholding, 3D morphological cleanup was applied: connected components smaller than 250 voxels were removed and internal voids up to 500 voxels were filled. The mask was then eroded in 3D using a spherical structuring element (radius = 10 voxels) to exclude the 3D printed tube, ensuring that only the iodine-containing region remained in the segmented volume. The eroded binary mask and the masked prior volume were saved for subsequent analysis.

Quantitative analysis was performed by applying the eroded mask to each cropped, subtracted dataset. Voxel values within the mask were extracted as raw attenuation and converted to iodine concentration using a calibration factor derived from KI calibration samples.

2.11 Comparison with reference data

For each iodine dilution (1, 3, and 5 mg I/mL), concentration-time curves were generated and compared with reference UV/VIS spectrophotometry data and with the optical input-output profiles of the flow system. The agreement between 4D DCE-bCT and UV/VIS was assessed by comparing peak concentrations, and reporting absolute and percentage errors.

For the gradual inflow-outflow sequence, optical signals were recorded at the P1 and P2 positions, then time shifted and averaged to obtain a single optical reference curve. UV/VIS samples were drawn at the same two positions near the peak, analyzed by spectrophotometry, and averaged to yield a single UV/VIS reference value. The 4D DCE-bCT-derived concentration-time curve was compared with these averaged references. When a single theoretical curve was displayed, the theoretical P1 and P2 profiles computed from the programmed injection were averaged in the same manner. Comparisons included peak concentration, wash-in and wash-out dynamics, and qualitative agreement of curve shapes.

3 Results

3.1 In-line spectroscopy and UV/VIS calibration curves

The calibration curves for the two in-line spectroscopy systems are shown in Figure 6.B1 in Appendix B. At the phantom entrance (P1), the fitted equation is:

$$y = 0.101 + (0.999 - 0.101)\, exp(-0.469\, X)$$

with a root-mean-square error (RMSE) of 0.005. At the phantom exit (P2), the relationship is defined as:

$$y = 0.038 + (0.999 - 0.038)\, exp(-0.464\, X)$$

with an RMSE of 0.005.

The calibration curve for the tested iodine concentrations in the UV/VIS spectrophotometer is illustrated in Figure 6.B2 of Appendix B. The relationship between iodine concentration and absorbance at 525 nm is defined as:

$$y = 0.32\, X + 0.02$$

with an R^2 value of 0.99. The concentrations of the samples were estimated using this relationship, and the results are added as data points in the figure.

3.2 Calibration results

The calibration curve (Figure 6.5) demonstrated a linear relationship, with slope of 37.86 mg I/mL per cm^{-1} and a standard error (Sy.x) of 0.10 mg I/mL, indicating close agreement between measured data and the fitted line.

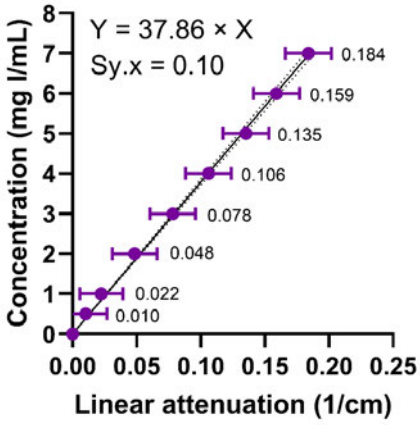

Figure 6.5: Calibration curve relating iodine concentration to measured linear attenuation. Purple markers indicate measured values. Error bars represent the standard deviation of repeated measurements. The solid black line shows the linear regression fit, while dotted lines represent the 95% confidence interval of the fit. The residual standard error (Sy.x = 0.10 mg I/mL) quantifies the scatter of measured values around the fitted regression line.

3.3 Dynamic acquisitions: optical system vs. breast CT

3.3.1 Block pulse measurements

Block pulse time-concentration curves for iodine dilutions of 1, 3, and 5 mg I/mL are shown in Figure 6.6. The corresponding peak concentrations and errors are summarized in Table 6.1.

Table 6.1. Peak concentration comparison between 4D DCE-bCT and UV/VIS for block pulse measurements.

Nominal conc (mg I/mL)	UV/VIS (mg I/mL)	4D DCE-bCT peak (mg I/mL)	Absolute error (mg I/mL)	Percentage error (%)
1	1.07	0.07	1.00	93.5
3	2.99	1.92	1.07	35.8
5	4.77	4.42	0.35	7.3

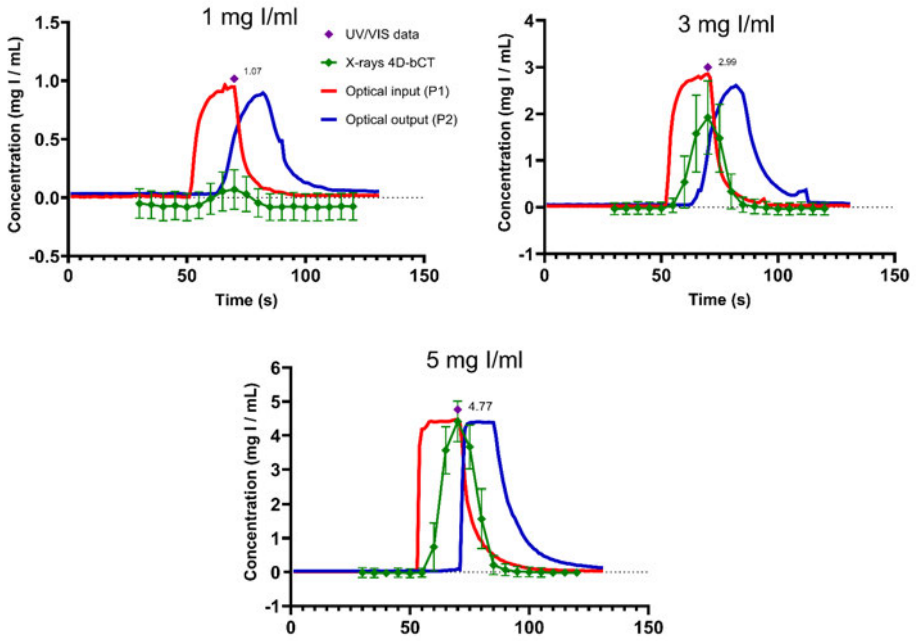

Figure 6.6: Block pulse time-concentration curves obtained with 4D DCE-bCT (green), optical input (red), optical output (blue), and reference UV/VIS spectrophotometry (purple) for samples with 1, 3, and 5 mg I/mL. 4D DCE-bCT values were derived from voxel intensities converted using the KI calibration factor.

3.3.2 Gradual inflow and outflow

Figure 6.7 shows the gradual inflow–outflow sequence. The 4D DCE-bCT-derived concentration-time curve is plotted alongside the theoretical profile, the averaged optical signal, and the averaged UV/VIS measurement. The UV/VIS measurement (6.07 mg I/mL) coincided with the peak of the theoretical curve, while the optical average peaked at 5.26 mg I/mL, reflecting temporal smoothing of the optical signal. The 4D DCE-bCT peak concentration was 5.23 ± 0.62 mg I/mL.

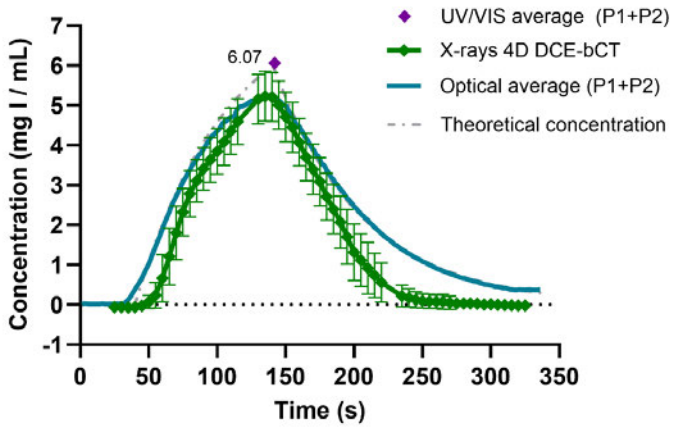

Figure 6.7: Comparison of 4D DCE-bCT-derived concentration-time curve (green) with averaged optical reference (teal) and averaged UV/VIS measurement (purple) during the gradual inflow-outflow sequence. The theoretical concentration profile is shown in gray (dashed) for reference.

4 Discussion

This study experimentally evaluated the quantitative accuracy of dynamic iodine imaging in 4D DCE-bCT using a simplified perfusion phantom and an in-line optical reference together with extracted samples as the reference standards. The results demonstrated that the current reconstruction and calibration pipeline effectively captured time-varying iodine profiles and accurately quantified peak intensities at concentrations from approximately 3 mg I/mL upward. At lower concentrations (≤3 mg I/mL), temporal dynamics remained identifiable, but intensity estimates were less precise, reflecting the combined effects of image noise, spatial resolution limitations, and calibration sensitivity at low attenuation values.

The x-ray calibration curve derived from KI dilutions was highly linear overall. However, at 1 mg I/mL the measured attenuation of 0.022 cm^{-1} yielded 0.83 mg I/mL, corresponding to a 17% underestimation. This illustrates how small absolute errors

in attenuation near zero translate into disproportionately large relative errors. At 3 mg I/mL, the peak concentration was measurable but underestimated (1.92 mg I/mL), while at 5 mg I/mL the error was within 10% (4.42 mg I/mL) and the x-ray-based measurement corresponded with the dynamic optical one. This experiment shows that, in our setup with a 3-mm tube, the pipeline reliably quantified concentrations ≥3 mg I/mL, while lower values could only be tracked qualitatively.

Clinical CT studies have reported mean iodine concentrations in breast tumors between 1 and 3 mg I/mL, with maxima up to 6 mg I/mL, although values depend strongly on contrast protocol and acquisition phase. Volterrani et al.[197] used iopamidol 370 mg I/mL at 1.5 mL/kg (late arterial phase) and reported a mean of 2.7 ± 1.0 mg I/mL (maximum 5.6 mg I/mL), identifying 1.7 mg I/mL as an optimal diagnostic cutoff. Hasse et al.[211] applied iohexol 350 mg I/mL at 1.43 mL/kg (venous phase) and observed 1.9 ± 0.6 mg I/mL with maxima of 6 mg I/mL, while Chen et al.[212] used ioversol 320 mg I/mL at 1.2 mL/kg (arterial and venous phases) and reported mean values of 1.1 mg I/mL (maximum 1.38 mg I/mL).

In our phantom, a programmed inflow of 7.6 mg I/mL into a 24-mL mixing chamber produced a UV/VIS peak of 6.07 mg I/mL, while bCT measured 5.23 ± 0.62 mg I/mL. This dilution-dispersion effect parallels in-vivo conditions, where high-concentration agents (320-370 mg I/mL) are distributed and attenuated to tumor tissue values in the 1-6 mg I/mL range. By including up to 7.6 mg I/mL in our phantom, we ensured that the resulting peaks (≈6 mg I/mL) overlapped with reported clinical maxima, while also illustrating how dilution, dispersion, and target size strongly influence the measured values.

Target size further influenced performance. The tube with a 3-mm inner-diameter used in this work was intended to approximate feeding vessels that develop during tumor angiogenesis, providing a deliberately challenging but clinically relevant test. In Figure 5.14 of Chapter 5, large 28-mm tubes showed <1% differences between IMPACT and PICCS reconstructions, confirming stable quantification in sufficiently sized volumes.[204]

Conversely, previous experiments demonstrated that reliable quantification is not achievable below 1 mm diameter.[215] This is consistent with the modulation transfer function (MTF) reported in Chapter 5 (Figure 5.12), which shows decreasing resolution as feature size decreases.

A 28-mm diameter tube (≈0.04 mm^{-1}) lies in the high-MTF region and yields stable quantification, a tube with a 3-mm inner diameter (≈0.33 mm^{-1}) falls in the mid-range where temporal dynamics remain detectable provided concentrations exceed ≈3 mg/mL. In contrast, a tube with a 1-mm inner diameter (1 mm^{-1}) lies near zero MTF, making quantification not feasible. Together, these results indicate that 4D DCE-bCT with its current set of selected parameters is accurate for large targets, feasible for structures down to ≈3 mm at clinically relevant concentrations, and limited applicability for features near 1 mm. Even with reduced precision at 1–3 mg I/mL, the modality preserved key dynamic features (arrival, peak time, washout), which are the parameters most relevant for clinical translation.

It is likely that the reconstruction parameters optimized for previous scans were not fully appropriate for the setup used in this work, which differed in several respects (e.g., target size). This was particularly evident in the suppression of low iodine signals, most likely caused by overly aggressive denoising during image processing. Our simplified phantom design allowed us to validate the end-to-end pipeline without interference from breast tissue heterogeneity, though at the cost of not reproducing perfusion complexity or microvascular networks. Although more complex phantoms, such as tumor models with heterogeneous perfusion or microvascular structures, could provide additional insights, the next step will be pilot clinical imaging studies to evaluate feasibility and utility in patient populations. These studies will also allow reconstruction parameters to be fine-tuned specifically for clinical application.

The acquisition protocol was limited to three dynamic phases, leading to 5-second inter-sequence gaps and incomplete temporal coverage. The updated 3D-printed optical measurement piece reduced mixing artifacts and improved quantification of time-dependent iodine concentrations, yet its transmission accuracy declined at iodine concentrations above 5 mg I/mL, requiring discrete UV/VIS sampling at peak times to address non-linearities. Finally, although the UV/VIS spectrophotometer was highly accurate, manual sampling at fixed time points remained prone to minor timing errors.

5 Conclusion

This study demonstrated that 4D DCE-bCT can accurately quantify dynamic iodine concentrations from approximately 3 mg I/mL upward in a 3-mm tube phantom, supported by in-line optical and UV/VIS reference measurements. Using this small

target size emphasized robustness under deliberately challenging conditions representative of tumor angiogenesis, while also highlighting limitations near the lower detection threshold. These findings establish the quantitative feasibility of the proposed pipeline for small targets at clinically relevant concentrations and support progression toward more anatomically realistic phantoms and initial clinical evaluation.

Appendix A – Optical measurement piece

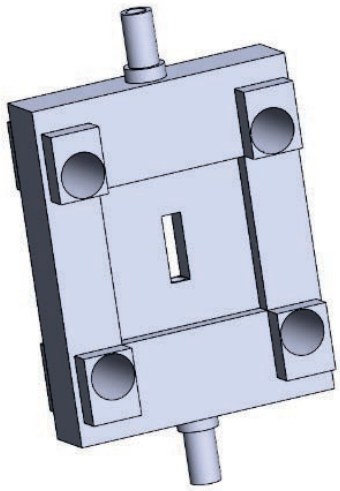

Figure 6.A1: 3D-printed optical measurement piece.

The optical measurement piece has an inflow and outflow tube with an internal diameter of 3 mm. The rectangular slit for optical measurements has a 3 mm width, 10 mm length, and 3 mm depth. A square microscopic cover glass is glued to both sides of the measurement piece to create a closed volume and enable fluid flow.

Appendix B - Calibration curves of in-line spectroscopy system and UV/VIS spectrophotometer

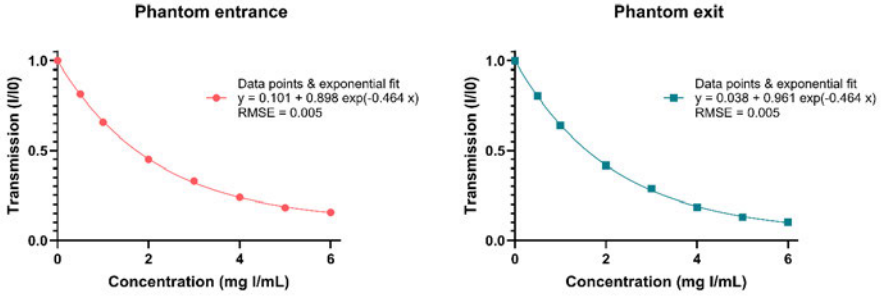

Figure 6.B1: calibration curves of the in-line spectroscopy system

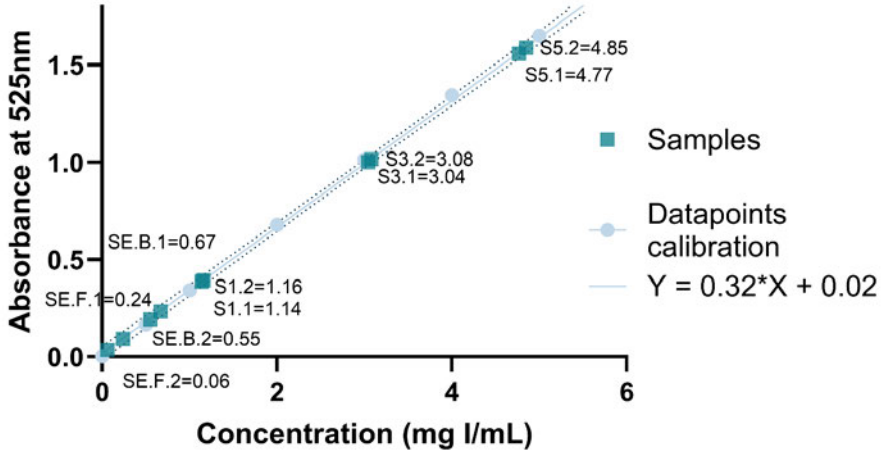

Figure 6.B2: calibration curve and fitted samples of the UV/VIS spectrophotometer

General Discussion

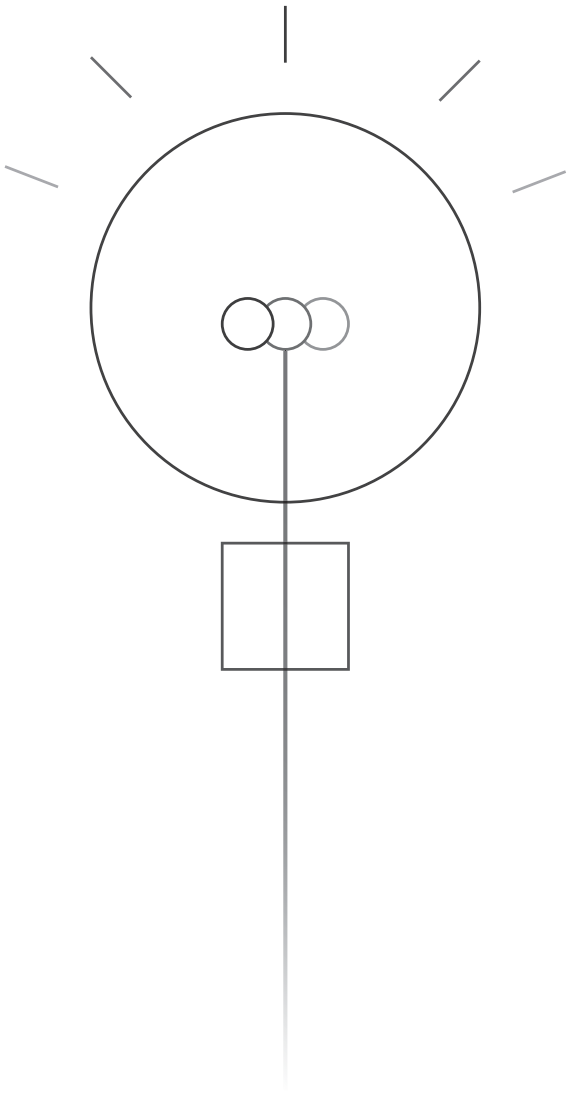

Although dedicated breast CT (bCT) was proposed over 50 years ago, its clinical adoption remains limited. The central question is no longer whether bCT can produce high-resolution 3D images, but whether it can deliver reproducible, additional information that improves patient care. Such improvement would come from providing quantitative information on perfusion and enhancement kinetics, which is not available when using conventional mammography and is only partly captured by MRI.

This thesis represents a significant step in advancing bCT from 3D to 4D imaging by integrating projection-domain optimization, advanced reconstruction techniques, and functional imaging protocols. Together, these developments demonstrate the potential of 4D dynamic contrast-enhanced bCT (4D DCE-bCT) for future clinical use and help address persistent limitations in breast imaging.

In the past, bCT systems struggled with limited spatial resolution and dose efficiency compared to mammography, and these challenges still persist today. Early systems relied on simpler reconstruction methods that required dense angular sampling to achieve accurate images, which resulted in high radiation doses. In addition, their clinical role remained undefined because bCT did not clearly outperform mammography for screening or diagnosis, nor MRI for functional characterization, leaving its niche uncertain and hindering adoption.

However, recent advancements, including the work presented in this thesis, have enabled high spatial and temporal-resolution imaging, positioning 4D DCE-bCT as a candidate for future clinical use in treatment monitoring and response prediction. This application is particularly suitable because response assessment requires reproducible, quantitative functional information on perfusion and enhancement kinetics, which 4D DCE-bCT can provide. Although such information would also be useful for diagnostic purposes, the relatively high dose involved in 4D DCE-bCT limits its applicability in that clinical application.

One of the central challenges in bCT for our application is scattered radiation, which degrades both contrast and quantitative accuracy. This issue is especially relevant in the non-compressed, free-hanging breast, where scatter is highly shape-dependent and this shape can vary widely between patients. This thesis addressed the problem by developing a deep learning model trained on patient-based phantom data, offering a practical and targeted solution for scatter correction in breast CT.

This work also included a systematic comparison of two generations of bCT systems. The results showed improvements in spatial resolution and dose efficiency, while

other system characteristics remained unchanged. These gains support potential clinical deployment, especially given clear advantages such as short exam times, full 3D imaging, and no need for breast compression. These improvements in resolution and dose efficiency also provide important input for the reconstruction algorithm, particularly in the context of quantitative imaging.

To optimize acquisition settings specifically for the 4D imaging sequence, a cascaded system analysis was implemented in the projection domain. The parallel cascaded model (PCM) was used to fine-tune parameters such as tube voltage and filtration, particularly for enhancing iodine detectability. This effort led to the development of CASYMIR, an open-source, Python-based implementation of the generalized cascaded systems model.[216] CASYMIR supports both direct and indirect detectors and is readily extendable to other imaging modalities, including mammography. It serves as both a tool for detector optimization and a reusable framework for imaging system design.

Since PCM does not easily account for non-linear reconstruction effects, a separate phantom-based study was carried out to investigate how reconstruction parameters, such as the number of iterations in IMPACT (iterative maximum-likelihood polychromatic algorithm for CT) and PICCS (the prior image constrained compressed sensing), influence spatial resolution, noise levels, and iodine quantification accuracy. Implementing 4D DCE-bCT required a reconstruction pipeline that carefully balanced dose, resolution, and temporal fidelity. This was achieved using IMPACT for static prior images and PICCS for dynamic frames.

Imaging parameters play a critical role in iodine detectability and quantification. Lower tube voltages and appropriate filtration improve contrast near the iodine K-edge, while increasing the tube current up to a saturation point reduces noise. Sparse sampling enhances temporal resolution but, if overused, can introduce artifacts and degrade quantitative accuracy. This thesis demonstrated that coordinated tuning of spectral and reconstruction parameters is essential for maximizing iodine detectability within dose constraints.

To evaluate quantitative accuracy under controlled conditions, a dedicated phantom was developed using a tube with a 3-mm inner diameter to mimic small vessels and early angiogenic tumor structures. Although this setup makes the measurements more susceptible to spatial resolution limits and image noise, the selected dimensions reflect clinically relevant targets for early perfusion imaging.

These technical developments led to the main contribution of this thesis: the implementation of 4D DCE-bCT. To the best of our knowledge, this work presents the first combined optimization of a dedicated reconstruction for 4D DCE-bCT, using a dedicated breast-shaped phantom with a flowing iodine-filled tube to emulate contrast dynamics.

This modality offers time-resolved, quantitative information about contrast-enhancement dynamics. Phantom-based evaluations confirmed that 4D DCE-bCT is reproducible and accurate within defined limits, making it clinically promising. The findings suggest that 4D DCE-bCT may enable the capture of enhancement kinetics and spatial iodine distribution in uncompressed breast volumes. A limitation of the current bCT design is that dynamic contrast imaging can only be performed in one breast at a time, this restriction is less critical for its intended applications in treatment monitoring and staging.

Future work should also address how to present and analyze the complex dynamic data produced by 4D DCE-bCT. Advanced methods, such as unbalanced regularized optimal mass transport (urOMT) model, among others, open up possibilities for visualizing contrast flow as a vector field and, more importantly, for parameterizing enhancement dynamics.[217] This could allow for quantification of perfusion and diffusion properties that may serve as useful biomarkers for tumor response. Combining such physics-based models with machine learning approaches for tumor tissue characterization and treatment response prediction could further enhance the clinical value of 4D DCE-bCT.

Beyond these technical developments and future methodological opportunities, the next step is to evaluate how 4D DCE-bCT could fit into clinical practice. While this thesis focused on the technical development and phantom-based validation of 4D DCE-bCT, its clinical translation depends on demonstrating clear advantages over existing modalities.

The need for more detailed functional and spatial characterization aligns with broader goals in oncology. As Guo et al. emphasize, the heterogeneity of breast cancer at the molecular, cellular, and spatial levels presents both a challenge and an opportunity. To achieve personalized precision therapy, we need multimodal, spatially resolved data that can guide therapies based on the unique characteristics of each tumor.[201] In this context, 4D DCE-bCT holds promise not only as a functional imaging modality, but also as a bridge between imaging features and personalized treatment. However, integrating it into routine clinical practice will also depend on

multicenter validation studies, standardized imaging protocols, cost-effectiveness analyses, and reimbursement strategies.

Seen this way, the field of 4D DCE-bCT is moving from technical development toward clinical application.

The contributions of this thesis, which include scatter correction, dose-efficient acquisition, robust system modeling, and dynamic quantitative imaging, provide a solid foundation for reliable and high-quality breast imaging. With continued refinement, validation, and integration into clinical workflows, 4D DCE-bCT has the potential to become a valuable addition to the imaging toolbox for personalized management of breast cancer.

Reflections and Outlook

Looking back, the past five years have been a process of both learning and innovation. If I had known at the beginning what I know now about imaging system development and the clinical environment in which it must operate, I would have structured several aspects differently.

Scatter correction, initially considered a technical side task, ultimately proved to be a key determinant in achieving reliable quantitative results. This experience highlighted how even supporting elements can significantly influence the overall performance of an imaging system. Nevertheless, some aspects of the developed solution remain limited. The model is specific and dedicated, meaning it requires retraining if the imaging geometry or x-ray settings change. While the patient population was generally well represented in the training set, a few extreme cases beyond the 95th percentile had to be handled separately. To address this, I supervised a master's student in developing a breast shape model capable of generating the missing sample population. This work led to the Master's thesis titled *Generative 3D Breast Shape Modeling and Deep Learning for X-ray Scatter Correction in Dedicated Breast CT: Towards 4D Dynamic Contrast-Enhanced Breast CT Imaging*.[218] Additionally, to handle variability in x-ray beam conditions and further improve model robustness, a broader range of spectra and acquisition settings would need to be simulated.

Although working with two different bCT systems was not a deliberate choice, it had a significant impact on the project. Due to the pandemic, the installation of

the GEN2 system was delayed by two years, which led me to begin work on the GEN1 system. I initially assumed that transferring the work to the GEN2 system would only require adjusting a few parameters. However, I soon encountered key differences between the two systems, including detector characteristics, x-ray tube properties, and an initially shifted detector position. This led to duplicated work and additional effort to revise the GEN1 developments for compatibility with GEN2. In hindsight, I would have waited for the installation of GEN2, focused on other parts of the project in the meantime, such as validation, and concentrated my efforts on the system ultimately intended for use in the 4D DCE-bCT modality.

One of the most challenging realizations during this project was how central the validation setup would become. What began as a basic setup involving the dynamic phantom, optical system, iodine injection, and x-ray timing became the foundation for producing reliable measurements and credible results. In retrospect, investing earlier in a coordinated validation strategy, along with a better understanding of iodine dynamics, might have accelerated progress and revealed system limitations sooner.

This experience reinforced the importance of remaining flexible and responsive to what the data and system behavior reveal over time. Among the most demanding aspects was maintaining functional integration across the entire imaging chain, from acquisition through reconstruction to analysis, as the project evolved. Yet this was also the most rewarding part of the process: seeing hardware, algorithms, and clinical objectives aligned within a single, working modality.

This thesis focused on demonstrating the feasibility of 4D DCE-bCT as a technical concept. Using a single, simplified phantom under controlled conditions was appropriate to isolate system-level performance and minimize confounding factors. However, this did not eliminate the need for multiple iterations in phantom design, pre- and post-processing, and repeated experiments.

I look back on these setbacks and embrace them with care, knowing they were valid decisions given the information available at the time. I believe the most effective way to learn is through conscious, hands-on experience, and failure is an integral part of the process. For someone beginning a similar project today, I would offer this piece of advice: *start simple but always keep the clinical goal in sight*.

As confidence grew in the acquisition and reconstruction pipeline, it became increasingly clear that more clinically grounded validation, linked to realistic enhancement dynamics, could enhance clinical translation and provide more

meaningful insights. This led to ongoing work beyond the scope of this thesis, in which modular perfusion phantoms are being developed to bridge the gap between system-level testing and clinical evaluation in patients, as described by Goris et al.[215]

If I were to continue this work for another five years, I would either focus on developing output analysis methods to support clinical integration of 4D DCE-bCT or apply the insights gained to advance a new imaging modality from technical concept to clinical readiness for patient studies. The question is no longer whether 4D DCE-bCT is feasible, as this has been demonstrated. The challenge now lies in identifying where and how it can be most effectively applied. Comparative studies with existing modalities, such as dynamic contrast-enhanced breast MRI, would be valuable for assessing treatment response and guiding therapy planning. Close collaboration with clinicians will be important to develop acquisition protocols that balance image quality with workflow feasibility and are tailored to specific clinical questions. Key considerations include the duration required to capture meaningful contrast dynamics and the minimum exposure time needed to ensure sufficient characterization accuracy.

In parallel, it is also important to explore the biological significance of the functional data provided by 4D DCE-bCT. The modality offers high-resolution information on contrast kinetics, creating the opportunity to identify subregions within tumors that may respond differently to therapy. Correlating these imaging-derived features with histological and genomic profiles could support more nuanced and individualized treatment strategies.

Throughout this project, I have been guided by the belief that imaging should not only detect disease but also reveal the underlying biology of individual tumors and guide treatment. 4D DCE-bCT represents a step toward that vision, an effort to combine imaging physics with clinical insight to enable more informed, precise, and patient-centered care.

One particularly promising application is the non-invasive prediction of pathological complete response (pCR). If imaging can reliably confirm that no cancer remains after treatment, it could justify skipping surgery in selected cases, potentially reducing patient burden and healthcare costs. Since pCR is currently confirmed through tissue analysis after surgery, developing a trustworthy imaging-based alternative would represent a significant shift in clinical decision-making. Achieving this would require strong predictive models trained on large and diverse datasets, ideally combined with other clinical and molecular data, in line with Gao et al.[219]

Building on this, the quantitative perfusion data obtainable with 4D DCE-bCT could be valuable in several clinical contexts. For staging, volumetric iodine mapping could help visualize lesion extent and multifocal disease. For predicting susceptibility to systemic therapy, perfusion patterns and baseline vascularity could provide predictors of treatment sensitivity. Finally, for response assessment, the modality's reproducible, quantitative measurements of contrast dynamics could allow detection of therapy-induced changes earlier than conventional MRI or mammography.

My hope is that this work may eventually help clinicians make more confident, less invasive treatment decisions and enable patients to benefit from a more personalized, data-driven approach to care.

As this technology moves closer to clinical use, its integration raises new questions that go beyond technical performance. There is an ethical responsibility in using imaging to guide or replace interventions as significant as surgery or radiotherapy. Predicting pCR non-invasively may offer substantial benefits, but it also requires careful modeling of uncertainty and clear communication of risk. Shared decision-making will be essential when imaging is used to support life-altering choices.

The growing use of radiomics, artificial intelligence, and other quantitative analysis techniques brings both opportunity and responsibility.

These tools must be interpretable, validated, and reliable across diverse populations and settings. Trust is fundamental for high-stakes applications such as predicting treatment outcomes.

With an eye to the future, I hope this work contributes not only to improved imaging for breast cancer but also to a broader evolution in medical imaging, one that values precision, adaptability, and above all, clinical relevance.

Bibliography

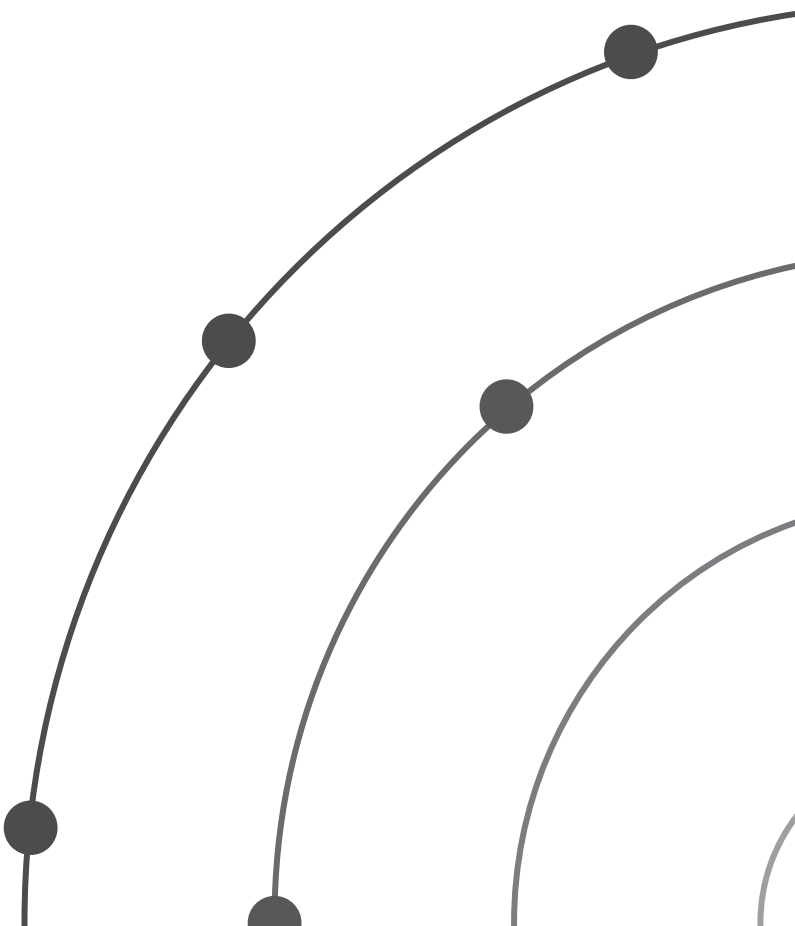

1. Bray F, Laversanne M, Sung H, et al. Global cancer statistics 2022: GLOBOCAN estimates of incidence and mortality worldwide for 36 cancers in 185 countries. *CA Cancer J Clin*. 2024;74(3):229-263. doi:10.3322/caac.21834
2. Arnold M, Morgan E, Rumgay H, et al. Current and future burden of breast cancer: global statistics for 2020 and 2040. *Breast*. 2022;66:15-23. doi:10.1016/j.breast.2022.08.010
3. Buist DS, Porter PL, Lehman C, Taplin SH, White E. Factors contributing to mammography failure in women aged 40-49 years. *J Natl Cancer Inst*. 2004;96(19):1432-1440. doi:10.1093/jnci/djh269
4. Boyd NF, Guo H, Martin LJ, et al. Mammographic density and the risk and detection of breast cancer. *N Engl J Med*. 2007;356(3):227-236. doi:10.1056/NEJMoa062790
5. Chong A, Weinstein SP, McDonald ES, Conant EF. Digital breast tomosynthesis: concepts and clinical practice. *Radiology*. 2019;292(1):1-14. doi:10.1148/radiol.2019180760
6. Vedantham S, Karellas A, Vijayaraghavan GR, Kopans DB. Digital breast tomosynthesis: state of the art. *Radiology*. 2015;277(3):663-684. doi:10.1148/radiol.2015141303
7. Nguyen T, Levy G, Poncelet E, et al. Overview of digital breast tomosynthesis: clinical cases, benefits and disadvantages. *Diagn Interv Imaging*. 2015;96(9):843-859. doi:10.1016/j.diii.2015.03.003
8. Sechopoulos I. A review of breast tomosynthesis, II: image reconstruction, processing and analysis, and advanced applications. *Med Phys*. 2013;40(1):014302. doi:10.1118/1.4770281
9. Sechopoulos I. A review of breast tomosynthesis, I: the image acquisition process. *Med Phys*. 2013;40(1):014301. doi:10.1118/1.4770279
10. Philpotts LE, Grewal JK, Horvath LJ, Giwerc MY, Staib L, Etesami M. Breast cancers detected during a decade of screening with digital breast tomosynthesis: comparison with digital mammography. *Radiology*. 2024;312(3):e232841. doi:10.1148/radiol.232841
11. Heindel W, Weigel S, Gerß J, et al. Digital breast tomosynthesis plus synthesised mammography versus digital screening mammography for the detection of invasive breast cancer (TOSYMA): a multicentre, open-label, randomised, controlled, superiority trial. *Lancet Oncol*. 2022;23(5):601-611. doi:10.1016/S1470-2045(22)00194-2
12. Zackrisson S, Lång K, Rosso A, et al. One-view breast tomosynthesis versus two-view mammography in the Malmö Breast Tomosynthesis Screening Trial (MBTST): a prospective, population-based, diagnostic accuracy study. *Lancet Oncol*. 2018;19(11):1493-1503. doi:10.1016/S1470-2045(18)30521-7
13. Skaane P, Bandos AI, Gullien R, et al. Comparison of digital mammography alone and digital mammography plus tomosynthesis in a population-based screening program. *Radiology*. 2013;267(1):47-56. doi:10.1148/radiol.12121373
14. Houssami N, Miglioretti DL. Digital breast tomosynthesis: a brave new world of mammography screening. *JAMA Oncol*. 2016;2(6):725-727. doi:10.1001/jamaoncol.2015.5569
15. Johnson K, Lang K, Ikeda DM, Akesson A, Andersson I, Zackrisson S. Interval breast cancer rates and tumor characteristics in the prospective population-based Malmö Breast Tomosynthesis Screening Trial. *Radiology*. 2021;299(3):559-567. doi:10.1148/radiol.2021204106
16. Houssami N, Bernardi D, Caumo F, et al. Interval breast cancers in the 'screening with tomosynthesis or standard mammography' (STORM) population-based trial. *Breast*. 2018;38:150-153. doi:10.1016/j.breast.2018.01.002
17. Kerlikowske K, Su YR, Sprague BL, et al. Association of screening with digital breast tomosynthesis vs digital mammography with risk of interval invasive and advanced breast cancer. *JAMA*. 2022;327(22):2220-2230. doi:10.1001/jama.2022.7672
18. Ohuchi N, Suzuki A, Sobue T, et al. Sensitivity and specificity of mammography and adjunctive ultrasonography to screen for breast cancer in the Japan Strategic Anticancer Randomized Trial

(J-START): a randomised controlled trial. *Lancet*. 2016;387(10016):341-348. doi:10.1016/S0140-6736(15)00774-6

19. Chae EY, Kim HH, Cha JH, Shin HJ, Kim H. Evaluation of screening whole-breast sonography as a supplemental tool in conjunction with mammography in women with dense breasts. *J Ultrasound Med*. 2013;32(9):1573-1578. doi:10.7863/ultra.32.9.1573
20. Corsetti V, Houssami N, Ferrari A, et al. Breast screening with ultrasound in women with mammography-negative dense breasts: evidence on incremental cancer detection and false positives, and associated cost. *Eur J Cancer*. 2008;44(4):539-544. doi:10.1016/j.ejca.2008.01.009
21. Kolb TM, Lichy J, Newhouse JH. Comparison of the performance of screening mammography, physical examination, and breast US and evaluation of factors that influence them: an analysis of 27,825 patient evaluations. *Radiology*. 2002;225(1):165-175. doi:10.1148/radiol.2251011667
22. Nothacker M, Duda V, Hahn M, et al. Early detection of breast cancer: benefits and risks of supplemental breast ultrasound in asymptomatic women with mammographically dense breast tissue: a systematic review. *BMC Cancer*. 2009;9:335. doi:10.1186/1471-2407-9-335
23. Scheel JR, Lee JM, Sprague BL, Lee CI, Lehman CD. Screening ultrasound as an adjunct to mammography in women with mammographically dense breasts. *Am J Obstet Gynecol*. 2015;212(1):9-17. doi:10.1016/j.ajog.2014.06.048
24. Sprague BL, Stout NK, Schechter C, et al. Benefits, harms, and cost-effectiveness of supplemental ultrasonography screening for women with dense breasts. *Ann Intern Med*. 2015;162(3):157-166. doi:10.7326/M14-0692
25. Mann RM, Cho N, Moy L. Breast MRI: state of the art. *Radiology*. 2019;292(3):520-536. doi:10.1148/radiol.2019182947
26. Kuhl CK. The current status of breast MR imaging, I: choice of technique, image interpretation, diagnostic accuracy, and transfer to clinical practice. *Radiology.* 2007;244(2):356-378. doi:10.1148/radiol.2442051620
27. Kuhl CK. Current status of breast MR imaging, II: clinical applications. *Radiology.* 2007;244(3):672-691. doi:10.1148/radiol.2443051661
28. Ikeda DM, Baker DR, Daniel BL. Magnetic resonance imaging of breast cancer: clinical indications and breast MRI reporting system. *J Magn Reson Imaging.* 2000;12(6):975-983. doi:10.1002/1522-2586(200012)12:6<975::aid-jmri24>3.0.co;2-y
29. Houssami N, Hayes DF. Review of preoperative magnetic resonance imaging (MRI) in breast cancer: should MRI be performed on all women with newly diagnosed, early stage breast cancer?. *CA Cancer J Clin*. 2009;59(5):290-302. doi:10.3322/caac.20028
30. Saadatmand S, Tilanus-Linthorst MM, Rutgers EJ, et al. Cost-effectiveness of screening women with familial risk for breast cancer with magnetic resonance imaging. *J Natl Cancer Inst*. 2013;105(17):1314-1321. doi:10.1093/jnci/djt203
31. Tollens F, Baltzer PAT, Dietzel M, et al. Economic potential of abbreviated breast MRI for screening women with dense breast tissue for breast cancer. *Eur Radiol*. 2022;32(11):7409-7419. doi:10.1007/s00330-022-08777-5
32. Marcon M, Fuchsjäger MH, Clauser P, Mann RM. ESR essentials: screening for breast cancer, general recommendations by EUSOBI. *Eur Radiol*. 2024;34(10):6348-6357. doi:10.1007/s00330-024-10740-5
33. Hylton NM, Blume JD, Bernreuter WK, et al. Locally advanced breast cancer: MR imaging for prediction of response to neoadjuvant chemotherapy, results from ACRIN 6657/I-SPY trial. *Radiology*. 2012;263(3):663-672. doi:10.1148/radiol.12110748

34. Marinovich ML, Houssami N, Macaskill P, et al. Meta-analysis of magnetic resonance imaging in detecting residual breast cancer after neoadjuvant therapy. *J Natl Cancer Inst*. 2013;105(5):321-333. doi:10.1093/jnci/djs528
35. Marinovich ML, Macaskill P, Irwig L, et al. Agreement between MRI and pathologic breast tumor size after neoadjuvant chemotherapy, and comparison with alternative tests: individual patient data meta-analysis. *BMC Cancer*. 2015;15:662. doi:10.1186/s12885-015-1664-4
36. Sardanelli F, Boetes C, Borisch B, et al. Magnetic resonance imaging of the breast: recommendations from the EUSOMA working group. *Eur J Cancer*. 2010;46(8):1296-1316. doi:10.1016/j.ejca.2010.02.015
37. Lindfors KK, Boone JM, Nelson TR, Yang K, Kwan AL, Miller DF. Dedicated breast CT: initial clinical experience. *Radiology*. 2008;246(3):725-733. doi:10.1148/radiol.2463070410
38. Aminololama-Shakeri S, Boone JM. Dedicated breast CT: getting ready for prime time. *J Breast Imaging*. 2024;6(5):465-475. doi:10.1093/jbi/wbae043
39. Siddall K, Zhang X, O'Connell A. Emerging clinical applications for cone beam breast CT: changing the breast imaging paradigm. *Curr Breast Cancer Rep.* 2024;16(2):134-141. doi:10.1007/s12609-024-00535-4
40. Zhu Y, O'Connell AM, Ma Y, et al. Dedicated breast CT: state of the art, II: clinical application and future outlook. *Eur Radiol*. 2022;32(4):2286-2300. doi:10.1007/s00330-021-08178-0
41. Zhu Y, O'Connell AM, Ma Y, et al. Dedicated breast CT: state of the art, I: historical evolution and technical aspects. *Eur Radiol*. 2022;32(3):1579-1589. doi:10.1007/s00330-021-08179-z
42. Sarno A, Mettivier G, Russo P. Dedicated breast computed tomography: basic aspects. *Med Phys*. 2015;42(6):2786-2804. doi:10.1118/1.4919441
43. O'Connell A, Conover DL, Zhang Y, et al. Cone-beam CT for breast imaging: radiation dose, breast coverage, and image quality. *AJR Am J Roentgenol*. 2010;195(2):496-509. doi:10.2214/AJR.08.1017
44. Sechopoulos I, Feng SS, D'Orsi CJ. Dosimetric characterization of a dedicated breast computed tomography clinical prototype. *Med Phys*. 2010;37(8):4110-4120. doi:10.1118/1.3457331
45. Boone JM, Nelson TR, Lindfors KK, Seibert JA. Dedicated breast CT: radiation dose and image quality evaluation. *Radiology*. 2001;221(3):657-667. doi:10.1148/radiol.2213010334
46. Kalender WA, Beister M, Boone JM, Kolditz D, Vollmar SV, Weigel MC. High-resolution spiral CT of the breast at very low dose: concept and feasibility considerations. *Eur Radiol*. 2012;22(1):1-8. doi:10.1007/s00330-011-2169-4
47. Prionas ND, Lindfors KK, Ray S, et al. Contrast-enhanced dedicated breast CT: initial clinical experience. *Radiology*. 2010;256(3):714-723. doi:10.1148/radiol.10092311
48. Prionas ND, Aminololama-Shakeri S, Yang K, Martinez SR, Lindfors KK, Boone JM. Contrast-enhanced dedicated breast CT detection of invasive breast cancer preceding mammographic diagnosis. *Radiol Case Rep*. 2015;10(2). doi:10.2484/rcr.v10i2.936
49. Seifert P, Conover D, Zhang Y, et al. Evaluation of malignant breast lesions in the diagnostic setting with cone beam breast computed tomography (Breast CT): feasibility study. *Breast J*. 2014;20(4):364-374. doi:10.1111/tbj.12285
50. Gazi PM, Aminololama-Shakeri S, Yang K, Boone JM. Temporal subtraction contrast-enhanced dedicated breast CT. *Phys Med Biol*. 2016;61(17):6322-6346. doi:10.1088/0031-9155/61/17/6322
51. D'Orsi CJ, Sickles EA, Mendelson EB, Morris EA. *ACR BI-RADS® Atlas: Breast Imaging Reporting and Data System*. 5th ed. American College of Radiology; 2013.
52. Liberman L, Abramson AF, Squires FB, Glassman JR, Morris EA, Dershaw DD. The breast imaging reporting and data system: positive predictive value of mammographic features and final assessment categories. *AJR Am J Roentgenol*. 1998;171(1):35-40. doi:10.2214/ajr.171.1.9648759

53. Gutierrez RL, DeMartini WB, Eby PR, Kurland BF, Peacock S, Lehman CD. BI-RADS lesion characteristics predict likelihood of malignancy in breast MRI for masses but not for nonmasslike enhancement. *AJR Am J Roentgenol*. 2009;193(4):994-1000. doi:10.2214/AJR.08.1983

54. Mahoney MC, Gatsonis C, Hanna L, DeMartini WB, Lehman C. Positive predictive value of BI-RADS MR imaging. *Radiology*. 2012;264(1):51-58. doi:10.1148/radiol.12110619

55. Ma Y, Liu A, O'Connell AM, et al. Contrast-enhanced cone beam breast CT features of breast cancers: correlation with immunohistochemical receptors and molecular subtypes. *Eur Radiol. 2021;*31(4):2580-2589. doi:10.1007/s00330-020-07277-8

56. Kuhl CK. MRI of breast tumors. *Eur Radiol*. 2000;10(1):46-58. doi:10.1007/s003300050006

57. Caballo M, Michielsen K, Fedon C, Sechopoulos I. Towards 4D dedicated breast CT perfusion imaging of cancer: development and validation of computer simulated images. *Phys Med Biol*. 2019;64(24):245004. doi:10.1088/1361-6560/ab55ac

58. Niu T, Zhu L. Overview of x-ray scatter in cone-beam computed tomography and its correction methods. *Curr Med Imaging*. 2010;6(2):82-89. doi:10.2174/157340510791268515

59. Rührnschopf EP, Klingenbeck K. A general framework and review of scatter correction methods in x-ray cone-beam computerized tomography. Part 1: scatter compensation approaches. *Med Phys.* 2011;38(7):4296-4311. doi:10.1118/1.3599033

60. Ruhrnschopf And EP, Klingenbeck K. A general framework and review of scatter correction methods in cone beam CT. Part 2: scatter estimation approaches. *Med Phys*. 2011;38(9):5186-5199. doi:10.1118/1.3589140

61. Maier J, Eulig E, Vöth T, et al. Real-time scatter estimation for medical CT using the deep scatter estimation: method and robustness analysis with respect to different anatomies, dose levels, tube voltages, and data truncation. *Med Phys*. 2019;46(1):238-249. doi:10.1002/mp.13274

62. Chang J, Kim S, Jang DY, Suh TS. A static multi-slit collimator system for scatter reduction in cone-beam CT. *J Appl Clin Med Phys.* 2010;11(4):3269. doi:10.1120/jacmp.v11i4.3269

63. Stankovic U, Ploeger LS, van Herk M, Sonke JJ. Optimal combination of anti-scatter grids and software correction for CBCT imaging. *Med Phys*. 2017;44(9):4437-4451. doi:10.1002/mp.12385

64. Altunbas C, Kavanagh B, Alexeev T, Miften M. Transmission characteristics of a two dimensional antiscatter grid prototype for CBCT. *Med Phys*. 2017;44(8):3952-3964. doi:10.1002/mp.12346

65. Zhu L, Xie Y, Wang J, Xing L. Scatter correction for cone-beam CT in radiation therapy. *Med Phys*. 2009;36(6):2258-2268. doi:10.1118/1.3130047

66. Roser P, Birkhold A, Preuhs A, et al. X-ray scatter estimation using deep splines. *IEEE Trans Med Imaging.* 2021;40(9):2272-2283. doi:10.1109/TMI.2021.3074712

67. Siewerdsen JH, Daly MJ, Bakhtiar B, et al. A simple, direct method for x-ray scatter estimation and correction in digital radiography and cone-beam CT. *Med Phys*. 2006;33(1):187-197. doi:10.1118/1.2148916

68. Jiang Y, Yang C, Yang P, et al. Scatter correction of cone-beam CT using a deep residual convolution neural network (DRCNN). *Phys Med Biol*. 2019;64(14):145003. doi:10.1088/1361-6560/ab23a6

69. Cai W, Ning R, Conover D. Scatter correction for clinical cone beam CT breast imaging based on breast phantom studies. *J Xray Sci Technol*. 2011;19(1):91-109. doi:10.3233/XST-2010-028000280

70. Li H, Mohan R, Zhu XR. Scatter kernel estimation with an edge-spread function method for cone-beam computed tomography imaging. *Phys Med Biol*. 2008;53(23):6729-6748. doi:10.1088/0031-9155/53/23/006

71. Nomura Y, Xu Q, Shirato H, Shimizu S, Xing L. Projection-domain scatter correction for cone beam computed tomography using a residual convolutional neural network. *Med Phys*. 2019;46(7):3142-3155. doi:10.1002/mp.13583

72. van der Heyden B, Uray M, Fonseca GP, et al. A Monte Carlo based scatter removal method for non-isocentric cone-beam CT acquisitions using a deep convolutional autoencoder. *Phys Med Biol*. 2020;65(14):145002. doi:10.1088/1361-6560/ab8954

73. Lee H, Lee J. A deep learning-based scatter correction of simulated x-ray images. *Electronics.* 2019;8(9):944. doi:10.3390/electronics8090944

74. Maspero M, Houweling AC, Savenije MHF, et al. A single neural network for cone-beam computed tomography-based radiotherapy of head-and-neck, lung and breast cancer. *Phys Imaging Radiat Oncol*. 2020;14:24-31. doi:10.1016/j.phro.2020.04.002

75. O'Connell A, Conover DL, Zhang Y, et al. Cone-beam CT for breast imaging: radiation dose, breast coverage, and image quality. *AJR Am J Roentgenol*. 2010;195(2):496-509. doi:10.2214/AJR.08.1017

76. Kwan AL, Boone JM, Shah N. Evaluation of x-ray scatter properties in a dedicated cone-beam breast CT scanner. *Med Phys*. 2005;32(9):2967-2975. doi:10.1118/1.1954908

77. Chen Y, Liu B, O'Connor JM, Didier CS, Glick SJ. Characterization of scatter in cone-beam CT breast imaging: comparison of experimental measurements and Monte Carlo simulation. *Med Phys*. 2009;36(3):857-869. doi:10.1118/1.3077122

78. Kontson K, Jennings RJ. Characterization of scatter magnitude and distribution in dedicated breast computed tomography with bowtie filters. *J Med Imaging (Bellingham)*. 2014;1(3):033505. doi:10.1117/1.JMI.1.3.033505

79. Reiser I, Nishikawa RM, Giger ML, Boone JM, Lindfors KK, Yang K. Automated detection of mass lesions in dedicated breast CT: a preliminary study. *Med Phys*. 2012;39(2):866-873. doi:10.1118/1.3678991

80. Ning R, Tang X, Conover D. X-ray scatter correction algorithm for cone beam CT imaging. *Med Phys*. 2004;31(5):1195-1202. doi:10.1118/1.1711475

81. Glick SJ, Didier CS. Can anti-scatter grids improve image quality in breast CT? In: Dössel O, Schlegel WC, eds. *World Congress on Medical Physics and Biomedical Engineering, September 7–12, 2009; Munich, Germany.* IFMBE Proceedings. Vol 25/2. Springer; 2009. doi:10.1007/978-3-642-03879-2_243

82. Yang K, Burkett G, Boone JM. A breast-specific, negligible-dose scatter correction technique for dedicated cone-beam breast CT: a physics-based approach to improve Hounsfield Unit accuracy. *Phys Med Biol*. 2014;59(21):6487-6505. doi:10.1088/0031-9155/59/21/6487

83. Sechopoulos I. X-ray scatter correction method for dedicated breast computed tomography. *Med Phys*. 2012;39(5):2896-2903. doi:10.1118/1.4711749

84. Ramamurthy S, D'Orsi CJ, Sechopoulos I. X-ray scatter correction method for dedicated breast computed tomography: improvements and initial patient testing. *Phys Med Biol*. 2016;61(3):1116-1135. doi:10.1088/0031-9155/61/3/1116

85. Ghazi P, Youssefian S, Ghazi T. A novel hardware duo of beam modulation and shielding to reduce scatter acquisition and dose in cone-beam breast CT. *Med Phys.* 2022;49(1):169-185. doi:10.1002/mp.15374

86. Shi L, Vedantham S, Karellas A, Zhu L. Library based x-ray scatter correction for dedicated cone beam breast CT. *Med Phys*. 2016;43(8):4529. doi:10.1118/1.4955121

87. Shi L, Vedantham S, Karellas A, Zhu L. X-ray scatter correction for dedicated cone-beam breast CT using a forward-projection model. *Med Phys.* 2017;44(6):2312-2320. doi:10.1002/mp.12213

88. Caballo M, Boone JM, Mann R, Sechopoulos I. An unsupervised automatic segmentation algorithm for breast tissue classification of dedicated breast computed tomography images. *Med Phys*. 2018;45(6):2542-2559. doi:10.1002/mp.12920

89. Caballo M, Fedon C, Brombal L, Mann R, Longo R, Sechopoulos I. Development of 3D patient-based super-resolution digital breast phantoms using machine learning. *Phys Med Biol*. 2018;63(22):225017. doi:10.1088/1361-6560/aae78d

90. Sechopoulos I, Vedantham S, Suryanarayanan S, D'Orsi CJ, Karellas A. Monte Carlo and phantom study of the radiation dose to the body from dedicated CT of the breast. *Radiology*. 2008;247(1):98-105. doi:10.1148/radiol.2471071080

91. Agostinelli S, Allison J, Amako K, et al. Geant4—a simulation toolkit. *Nucl Instrum Methods Phys Res A*. 2003;506(3):250-303. doi:10.1016/S0168-9002(03)01368-8

92. Hernandez AM, Seibert JA, Nosratieh A, Boone JM. Generation and analysis of clinically relevant breast imaging x-ray spectra. *Med Phys*. 2017;44(6):2148-2160. doi:10.1002/mp.12222

93. Sempau J, Sánchez-Reyes A, Salvat F, ben Tahar HO, Jiang SB, Fernández-Varea JM. Monte Carlo simulation of electron beams from an accelerator head using PENELOPE. *Phys Med Biol*. 2001;46(4):1163-1186. doi:10.1088/0031-9155/46/4/318

94. Ronneberger O, Fischer P, Brox T. U-Net: convolutional networks for biomedical image segmentation. In: Navab N, Hornegger J, Wells WM, Frangi AF, eds. *Medical Image Computing and Computer-Assisted Intervention - MICCAI 2015*. Lecture Notes in Computer Science. Vol 9351. Springer; 2015:234-241. doi:10.1007/978-3-319-24574-4_28

95. Caballo M, Hernandez AM, Lyu SH, et al. Computer-aided diagnosis of masses in breast computed tomography imaging: deep learning model with combined handcrafted and convolutional radiomic features. *J Med Imaging (Bellingham)*. 2021;8(2):024501. doi:10.1117/1.JMI.8.2.024501

96. Hammerstein GR, Miller DW, White DR, Masterson ME, Woodard HQ, Laughlin JS. Absorbed radiation dose in mammography. *Radiology*. 1979;130(2):485-491. doi:10.1148/130.2.485

97. Byng JW, Mainprize JG, Yaffe MJ. X-ray characterization of breast phantom materials. *Phys Med Biol*. 1998;43(5):1367-1377. doi:10.1088/0031-9155/43/5/026

98. De Man B, Nuyts J, Dupont P, Marchal G, Suetens P. Reduction of metal streak artifacts in x-ray computed tomography using a transmission maximum a posteriori algorithm. *IEEE Trans Nucl Sci*. 2000;47(3):977-981. doi:10.1109/23.856534

99. Herman GT. Correction for beam hardening in computed tomography. *Phys Med Biol*. 1979;24(1):81-106. doi:10.1088/0031-9155/24/1/008

100. Poletti ME, Gonçalves D, Mazzaro I. X-ray scattering from human breast tissues and breast-equivalent materials. *Phys Med Biol*. 2002;47(1):47-63. doi:10.1088/0031-9155/47/1/304

101. Engel KJ, Herrmann C, Zeitler G. X-ray scattering in single- and dual-source CT. *Med Phys*. 2008;35(1):318-332. doi:10.1118/1.2820901

102. Zhu L, Wang J, Xing L. Noise suppression in scatter correction for cone-beam CT. *Med Phys*. 2009;36(3):741-752. doi:10.1118/1.3063001

103. Badal A, Badano A. Accelerating Monte Carlo simulations of photon transport in a voxelized geometry using a massively parallel graphics processing unit. *Med Phys*. 2009;36(11):4878-4880. doi:10.1118/1.3231824

104. Badal A, Sharma D, Graff CG, Zeng R, Badano A. Mammography and breast tomosynthesis simulator for virtual clinical trials. *Comput Phys Commun*. 2021;261:107779. doi:10.1016/j.cpc.2020.107779

105. Huang SY, Boone JM, Yang K, et al. The characterization of breast anatomical metrics using dedicated breast CT. *Med Phys*. 2011;38(4):2180-2191. doi:10.1118/1.3567147

106. Yaffe MJ, Boone JM, Packard N, et al. The myth of the 50-50 breast. *Med Phys*. 2009;36(12):5437-5443. doi:10.1118/1.3250863

107. Hernandez AM, Seibert JA, Boone JM. Breast dose in mammography is about 30% lower when realistic heterogeneous glandular distributions are considered. *Med Phys*. 2015;42(11):6337-6348. doi:10.1118/1.4931966

108. Gurrola-Ramos J, Dalmau O, Alarcón TE. A residual dense U-Net neural network for image denoising. *IEEE Access*. 2021;9:31742-31754. doi:10.1109/ACCESS.2021.3061062

109. Siegel RL, Giaquinto AN, Jemal A. Cancer statistics, 2024. *CA Cancer J Clin*. 2024;74(1):12-49. doi:10.3322/caac.21820

110. Mandelblatt J, van Ravesteyn N, Schechter C, et al. Which strategies reduce breast cancer mortality most? Collaborative modeling of optimal screening, treatment, and obesity prevention. *Cancer*. 2013;119(14):2541-2548. doi:10.1002/cncr.28087

111. Humphrey LL, Helfand M, Chan BK, Woolf SH. Breast cancer screening: a summary of the evidence for the U.S. Preventive Services Task Force. *Ann Intern Med*. 2002;137(5):347-360. doi:10.7326/0003-4819-137-5_part_1-200209030-00012

112. Wilkinson AN, Ellison LF, Billette JM, Seely JM. Impact of Breast Cancer Screening on 10-Year Net Survival in Canadian Women Age 40-49 Years. *J Clin Oncol*. 2023;41(29):4669-4677. doi:10.1200/JCO.23.00348

113. Berg WA, Zhang Z, Lehrer D, et al. Detection of breast cancer with addition of annual screening ultrasound or a single screening MRI to mammography in women with elevated breast cancer risk. *JAMA*. 2012;307(13):1394-1404. doi:10.1001/jama.2012.388

114. Wienbeck S, Fischer U, Luftner-Nagel S, Lotz J, Uhlig J. Contrast-enhanced cone-beam breast-CT (CBBCT): clinical performance compared to mammography and MRI. *Eur Radiol*. 2018;28(9):3731-3741. doi:10.1007/s00330-018-5376-4

115. Mandelblatt JS, Cronin KA, Bailey S, et al. Effects of mammography screening under different screening schedules: model estimates of potential benefits and harms. *Ann Intern Med*. 2009;151(10):738-747. doi:10.7326/0003-4819-151-10-200911170-00010

116. Yang L, Zhou Z, Wang J, et al. Head-to-head comparison of cone-beam breast computed tomography and mammography in the diagnosis of primary breast cancer: A systematic review and meta-analysis. *Eur J Radiol*. 2024;171:111292. doi:10.1016/j.ejrad.2024.111292

117. Li H, Yin L, He N, et al. Comparison of comfort between cone beam breast computed tomography and digital mammography. *Eur J Radiol*. 2019;120:108674. doi:10.1016/j.ejrad.2019.108674

118. Brombal L, Arfelli F, Delogu P, et al. Image quality comparison between a phase-contrast synchrotron radiation breast CT and a clinical breast CT: a phantom based study. *Sci Rep*. 2019;9(1):17778. doi:10.1038/s41598-019-54131-z

119. Chen B, Ning R. Cone-beam volume CT breast imaging: feasibility study. *Med Phys*. 2002;29(5):755-770. doi:10.1118/1.1461843

120. Benítez RB, Ning R, Conover D, Liu S. NPS characterization and evaluation of a cone beam CT breast imaging system. *J Xray Sci Technol*. 2009;17(1):17-40. doi:10.3233/XST-2009-0213

121. Siddall K, Zhang X, O'Connell A. Emerging clinical applications for cone beam breast CT: changing the breast imaging paradigm. Curr Breast Cancer Rep. 2024;16(2):134-141. doi:10.1007/s12609-024-00535-4

122. Samei E, Flynn MJ, Reimann DA. A method for measuring the presampled MTF of digital radiographic systems using an edge test device. *Med Phys*. 1998;25(1):102-113. doi:10.1118/1.598165

123. Samei E, Ranger NT, Dobbins JT 3rd, Chen Y. Intercomparison of methods for image quality characterization. I. Modulation transfer function. *Med Phys*. 2006;33(5):1454-1465. doi:10.1118/1.2188816

124. Donini B, Rivetti S, Lanconelli N, Bertolini M. Free software for performing physical analysis of systems for digital radiography and mammography. *Med Phys*. 2014;41(5):051903. doi:10.1118/1.4870955

125. Dobbins JT 3rd, Samei E, Ranger NT, Chen Y. Intercomparison of methods for image quality characterization. II. Noise power spectrum. *Med Phys*. 2006;33(5):1466-1475. doi:10.1118/1.2188819

126. Bujila R, Omar A, Poludniowski G. A validation of SpekPy: A software toolkit for modelling X-ray tube spectra. *Phys Med*. 2020;75:44-54. doi:10.1016/j.ejmp.2020.04.026

127. Pautasso JJ, Michielsen K, Sechopoulos I. Technical note: Characterization, validation, and spectral optimization of a dedicated breast CT system for contrast-enhanced imaging. *Med Phys*. 2024;51(5):3322-3333. doi:10.1002/mp.17069

128. Beutel J, Kundel HL, Van Metter RL, eds. Handbook of medical imaging. Vol 1. Physics and psychophysics. SPIE Press; 2000.

129. Hubbell JH, Seltzer SM. Tables of x-ray mass attenuation coefficients and mass energy-absorption coefficients from 1 keV to 20 MeV for elements Z = 1 to 92 and 48 additional substances of dosimetric interest. NIST Standard Reference Database 126. National Institute of Standards and Technology; 2004. Accessed March 28, 2025. doi:10.18434/T4D01F

130. Gisvold JJ, Reese DF, Karsell PR. Computed tomographic mammography (CTM). *AJR Am J Roentgenol*. 1979;133(6):1143-1149. doi:10.2214/ajr.133.6.1143

131. O'Connell AM, Marini TJ, Kawakyu-O'Connor DT. Cone-Beam Breast Computed Tomography: Time for a New Paradigm in Breast Imaging. *J Clin Med*. 2021;10(21):5135. Published 2021 Oct 31. doi:10.3390/jcm10215135

132. Caballo M, Mann R, Sechopoulos I. Patient-based 4D digital breast phantom for perfusion contrast-enhanced breast CT imaging. *Med Phys*. 2018;45(10):4448-4460. doi:10.1002/mp.13156

133. Siewerdsen JH. Image quality models for 2D and 3D x-ray imaging systems: A perspective vignette. *Med Phys*. 2023;50 Suppl 1:109-116. doi:10.1002/mp.16051

134. Antonuk LE, Jee KW, El-Mohri Y, et al. Strategies to improve the signal and noise performance of active matrix, flat-panel imagers for diagnostic x-ray applications. *Med Phys*. 2000;27(2):289-306. doi:10.1118/1.598831

135. Cunningham IA. Linear-systems modeling of parallel cascaded stochastic processes: the NPS of radiographic screens with reabsorption of characteristic x-radiation. In: Medical Imaging 1998: Physics of Medical Imaging. Proc SPIE. Vol 3336. SPIE; 1998. doi:10.1117/12.317021

136. Cunningham IA, Moschandreu T, Subotic V. Detective quantum efficiency of fluoroscopic systems: the case for a spatial-temporal approach (or, does the ideal observer have infinite patience?). In: Medical Imaging 2001: Physics of Medical Imaging. Proc SPIE. Vol 4320. SPIE; 2001. doi:10.1117/12.430871

137. Cunningham IA, Yao J, Subotic V. Cascaded models and the DQE of flat-panel imagers: noise aliasing, secondary quantum noise, and reabsorption. In: Medical Imaging 2002: Physics of Medical Imaging. Proc SPIE. Vol 4682. SPIE; 2002. doi:10.1117/12.465610

138. Cunningham IA, Westmore MS, Fenster A. A spatial-frequency dependent quantum accounting diagram and detective quantum efficiency model of signal and noise propagation in cascaded imaging systems. Med Phys. 1994;21(3):417-427. doi:10.1118/1.597401

139. Yao J, Cunningham IA. Parallel cascades: new ways to describe noise transfer in medical imaging systems. *Med Phys*. 2001;28(10):2020-2038. doi:10.1118/1.1405842

140. Vedantham S, Karellas A, Suryanarayanan S. Solid-state fluoroscopic imager for high-resolution angiography: parallel-cascaded linear systems analysis. *Med Phys*. 2004;31(5):1258-1268. doi:10.1118/1.1689014

141. Rabbani M, Shaw R, Van Metter R. Detective quantum efficiency of imaging systems with amplifying and scattering mechanisms. *J Opt Soc Am A*. 1987;4(5):895-901. doi:10.1364/josaa.4.000895

142. Siewerdsen JH, Antonuk LE, el-Mohri Y, Yorkston J, Huang W, Cunningham IA. Signal, noise power spectrum, and detective quantum efficiency of indirect-detection flat-panel imagers for diagnostic radiology. *Med Phys*. 1998;25(5):614-628. doi:10.1118/1.598243

143. Richard S, Siewerdsen JH. Cascaded systems analysis of noise reduction algorithms in dual-energy imaging. *Med Phys*. 2008;35(2):586-601. doi:10.1118/1.2826556

144. Siewerdsen JH. *Signal, Noise, and Detective Quantum Efficiency of a-Si:H Flat-Panel Imagers*. PhD diss. University of Michigan; 1998.

145. Zhao W, Ristic G, Rowlands JA. X-ray imaging performance of structured cesium iodide scintillators. Med Phys. 2004;31(9):2594-2605. doi:10.1118/1.1782676

146. Evans DS, Workman A, Payne M. A comparison of the imaging properties of CCD-based devices used for small field digital mammography. *Phys Med Biol*. 2002;47(1):117-135. doi:10.1088/0031-9155/47/1/309

147. Suryanarayanan S, Karellas A, Vedantham S, Sechopoulos I. Theoretical analysis of high-resolution digital mammography. *Phys Med Biol*. 2006;51(12):3041-3055. doi:10.1088/0031-9155/51/12/003

148. Williams MB, Simoni PU, Smilowitz L, Stanton M, Phillips W, Stewart A. Analysis of the detective quantum efficiency of a developmental detector for digital mammography. *Med Phys*. 1999;26(11):2273-2285. doi:10.1118/1.598741

149. Zhao W, Ji WG, Debrie A, Rowlands JA. Imaging performance of amorphous selenium–based flat-panel detectors for digital mammography: characterization of a small-area prototype detector. Med Phys. 2003;30(2):254-263. doi:10.1118/1.1538233

150. Zhao B, Zhao W. Three-dimensional linear system analysis for breast tomosynthesis. *Med Phys*. 2008;35(12):5219-5232. doi:10.1118/1.2996014

151. Gang GJ, Lee J, Stayman JW, et al. Analysis of Fourier-domain task-based detectability index in tomosynthesis and cone-beam CT in relation to human observer performance. *Med Phys*. 2011;38(4):1754-1768. doi:10.1118/1.3560428

152. Gang GJ, Zbijewski W, Webster Stayman J, Siewerdsen JH. Cascaded systems analysis of noise and detectability in dual-energy cone-beam CT. *Med Phys*. 2012;39(8):5145-5156. doi:10.1118/1.4736420

153. Cao Q, Sisniega A, Brehler M, Stayman JW, Yorkston J, Siewerdsen JH, Zbijewski W. Modeling and evaluation of a high-resolution CMOS detector for cone-beam CT of the extremities. Med Phys. 2018;45(1):114-130. doi:10.1002/mp.12654

154. Sheth NM, Zbijewski W, Jacobson MW, et al. Mobile C-Arm with a CMOS detector: Technical assessment of fluoroscopy and Cone-Beam CT imaging performance. *Med Phys*. 2018;45(12):5420-5436. doi:10.1002/mp.13244

155. Prionas ND, Huang SY, Boone JM. Experimentally determined spectral optimization for dedicated breast computed tomography. *Med Phys*. 2011;38(2):646-655. doi:10.1118/1.3537077

156. Hernandez AM, Abbey CK, Ghazi P, Burkett G, Boone JM. Effects of kV, filtration, dose, and object size on soft tissue and iodine contrast in dedicated breast CT. Med Phys. 2020. doi:10.1002/mp.14159

157. Glick SJ, Makeev A. Investigation of x-ray spectra for iodinated contrast-enhanced dedicated breast CT. *J Med Imaging (Bellingham)*. 2017;4(1):013504. doi:10.1117/1.JMI.4.1.013504

158. Glick SJ, Thacker S, Gong X, Liu B. Evaluating the impact of X-ray spectral shape on image quality in flat-panel CT breast imaging. *Med Phys*. 2007;34(1):5-24. doi:10.1118/1.2388574

159. Weigel M, Vollmar SV, Kalender WA. Spectral optimization for dedicated breast CT. *Med Phys*. 2011;38(1):114-124. doi:10.1118/1.3523599

160. Teledyne DALSA. Xineos-3030HS. Accessed March 31, 2025. https://www.teledynedalsa.com/en/products/imaging/medical-x-ray-detectors/xineos-large-area/xineos-3030hs/

161. Siewerdsen JH, Antonuk LE, el-Mohri Y, et al. Empirical and theoretical investigation of the noise performance of indirect detection, active matrix flat-panel imagers (AMFPIs) for diagnostic radiology. *Med Phys*. 1997;24(1):71-89. doi:10.1118/1.597919

162. Newville M. XrayDB, release 4.5.6. Published January 8, 2025. Accessed March 31, 2025. https://xraypy.github.io/XrayDB/index.html

163. Askeland DR, Fulay PP, Wright WJ. *The Science and Engineering of Materials.* 6th ed. Cengage Learning; 2011.

164. Chan HP, Doi K. Energy and angular dependence of x-ray absorption and its effect on radiographic response in screen-film systems. *Phys Med Biol. 1983;28*(5):565-579. doi:10.1088/0031-9155/28/5/009

165. Jacques SL. Light distributions from point, line and plane sources for photochemical reactions and fluorescence in turbid biological tissues. *Photochem Photobiol. 1998;67*(1):23-32. doi:10.1111/j.1751-1097.1998.tb05161.x

166. Chantler CT, Olsen K, Dragoset RA, Kishore AR, Kotochigova SA, Zucker DS. *X-ray form factor, attenuation, and scattering tables.* National Institute of Standards and Technology; Physical Measurement Laboratory. Accessed March 31, 2025. https://www.nist.gov/pml/x-ray-form-factor-attenuation-and-scattering-tables

167. Jacques SL, Prahl SA. *ECE532 biomedical optics: Monte Carlo simulation lectures.* Oregon Graduate Institute; 1998. Accessed March 31, 2025. https://omlc.org/classroom/ece532/class4/index.html

168. Vedantham S. *Design and Characterization of a High-Resolution Cardiovascular Imager*. PhD diss. Worcester Polytechnic Institute; 2002.

169. Metz CE, Vyborny CJ. Wiener spectral effects of spatial correlation between the sites of characteristic x-ray emission and reabsorption in radiographic screen-film systems. *Phys Med Biol*. 1983;28(5):547-564. doi:10.1088/0031-9155/28/5/008

170. Pautasso JJ, Caballo M, Mikerov M, Boone JM, Michielsen K, Sechopoulos I. Deep learning for x-ray scatter correction in dedicated breast CT. *Med Phys*. 2023;50(4):2022-2036. doi:10.1002/mp.16185

171. International Commission on Radiation Units and Measurements. *Tissue Substitutes in Radiation Dosimetry and Measurement*. ICRU Report 44. 1989. Accessed March 31, 2025. https://www.icru.org/report/tissue-substitutes-in-radiation-dosimetry-and-measurement-report-44/

172. Richard S, Siewerdsen JH. Optimization of dual-energy imaging systems using generalized NEQ and imaging task. *Med Phys*. 2007;34(1):127-139. doi:10.1118/1.2400620

173. Richard S, Siewerdsen JH, Jaffray DA, Moseley DJ, Bakhtiar B. Generalized DQE analysis of radiographic and dual-energy imaging using flat-panel detectors. *Med Phys*. 2005;32(5):1397-1413. doi:10.1118/1.1901203

174. Hill ML, Mainprize JG, Carton AK, et al. Anatomical noise in contrast-enhanced digital mammography. Part I. Single-energy imaging. *Med Phys*. 2013;40(5):051910. doi:10.1118/1.4801905

175. Hill ML, Mainprize JG, Carton AK, et al. Anatomical noise in contrast-enhanced digital mammography. Part II. Dual-energy imaging. *Med Phys*. 2013;40(8):081907. doi:10.1118/1.4812681

176. Hu YH, Scaduto DA, Zhao W. Optimization of contrast-enhanced breast imaging: analysis using a cascaded linear system model. *Med Phys*. 2017;44(1):101-113. doi:10.1002/mp.12004

177. Day JA, Tanguay J. Monte-Carlo study of contrast-enhanced spectral mammography with cadmium telluride photon-counting x-ray detectors. *Med Phys*. 2024;51(4):2479-2498. doi:10.1002/mp.16837

178. Tward DJ, Siewerdsen JH. Noise aliasing and the 3D NEQ of flat-panel cone-beam CT: effect of 2D/3D apertures and sampling. *Med Phys*. 2009;36(8):3830-3843. doi:10.1118/1.3166933

179. Kijewski MF, Judy PF. The noise power spectrum of CT images. *Phys Med Biol*. 1987;32(5):565-575. doi:10.1088/0031-9155/32/5/003

180. Wilkinson AN, Billette JM, Ellison LF, Killip MA, Islam N, Seely JM. The Impact of Organised Screening Programs on Breast Cancer Stage at Diagnosis for Canadian Women Aged 40-49 and 50-59. *Curr Oncol*. 2022;29(8):5627-5643. doi:10.3390/curroncol29080444

181. Broglio KR, Quintana M, Foster M, et al. Association of Pathologic Complete Response to Neoadjuvant Therapy in HER2-Positive Breast Cancer With Long-Term Outcomes: A Meta-Analysis. *JAMA Oncol*. 2016;2(6):751-760. doi:10.1001/jamaoncol.2015.6113

182. van Uden DJP, van Maaren MC, Bult P, et al. Pathologic complete response and overall survival in breast cancer subtypes in stage III inflammatory breast cancer. *Breast Cancer Res Treat*. 2019;176(1):217-226. doi:10.1007/s10549-019-05219-7

183. Golshan M, Loibl S, Wong SM, et al. Breast Conservation After Neoadjuvant Chemotherapy for Triple-Negative Breast Cancer: Surgical Results From the BrighTNess Randomized Clinical Trial. *JAMA Surg*. 2020;155(3):e195410. doi:10.1001/jamasurg.2019.5410

184. Cortazar P, Zhang L, Untch M, et al. Pathological complete response and long-term clinical benefit in breast cancer: the CTNeoBC pooled analysis. *Lancet*. 2014;384(9938):164-172. doi:10.1016/S0140-6736(13)62422-8

185. Kuerer HM, Newman LA, Buzdar AU, et al. Residual metastatic axillary lymph nodes following neoadjuvant chemotherapy predict disease-free survival in patients with locally advanced breast cancer. *Am J Surg*. 1998;176(6):502-509. doi:10.1016/s0002-9610(98)00253-0

186. Tadros AB, Yang WT, Krishnamurthy S, et al. Identification of Patients With Documented Pathologic Complete Response in the Breast After Neoadjuvant Chemotherapy for Omission of Axillary Surgery. *JAMA Surg*. 2017;152(7):665-670. doi:10.1001/jamasurg.2017.0562

187. Volders JH, Negenborn VL, Spronk PE, et al. Breast-conserving surgery following neoadjuvant therapy-a systematic review on surgical outcomes. *Breast Cancer Res Treat*. 2018;168(1):1-12. doi:10.1007/s10549-017-4598-5

188. Turnbull LW. Dynamic contrast-enhanced MRI in the diagnosis and management of breast cancer. *NMR Biomed*. 2009;22(1):28-39. doi:10.1002/nbm.1273

189. Alvarez RE, Macovski A. Energy-selective reconstructions in x-ray computerized tomography. *Phys Med Biol*. 1976;21(5):733-744. doi:10.1088/0031-9155/21/5/002

190. Chen GH, Tang J, Leng S. Prior image constrained compressed sensing (PICCS): a method to accurately reconstruct dynamic CT images from highly undersampled projection data sets. *Med Phys*. 2008;35(2):660-663. doi:10.1118/1.2836423

191. De Man B, Nuyts J, Dupont P, Marchal G, Suetens P. An iterative maximum-likelihood polychromatic algorithm for CT. *IEEE Trans Med Imaging*. 2001;20(10):999-1008. doi:10.1109/42.959297

192. Menzel HG, Clement C, DeLuca P. ICRP Publication 110: realistic reference phantoms, an ICRP/ICRU joint effort. *Ann ICRP*. 2009;39(2):1-164. doi:10.1016/j.icrp.2009.09.001

193. Lauzier PT, Tang J, Chen GH. Prior image constrained compressed sensing: implementation and performance evaluation. *Med Phys*. 2012;39(1):66-80. doi:10.1118/1.3666946

194. Qi Z, Chen GH. Performance studies of four-dimensional cone beam computed tomography. *Phys Med Biol*. 2011;56(20):6709-6721. doi:10.1088/0031-9155/56/20/013

195. Richard S, Husarik DB, Yadava G, Murphy SN, Samei E. Towards task-based assessment of CT performance: system and object MTF across different reconstruction algorithms. *Med Phys*. 2012;39(7):4115-4122. doi:10.1118/1.4725171

196. Boone JM, Shah N, Nelson TR. A comprehensive analysis of DgN(CT) coefficients for pendant-geometry cone-beam breast computed tomography. *Med Phys*. 2004;31(2):226-235. doi:10.1118/1.1636571

197. Volterrani L, Gentili F, Fausto A, et al. Dual-Energy CT for Locoregional Staging of Breast Cancer: Preliminary Results. *AJR Am J Roentgenol*. 2020;214(3):707-714. doi:10.2214/AJR.18.20953

198. Nett BE, Brauweiler R, Kalender W, Rowley H, Chen GH. Perfusion measurements by micro-CT using prior image constrained compressed sensing (PICCS): initial phantom results. *Phys Med Biol*. 2010;55(8):2333-2350. doi:10.1088/0031-9155/55/8/014

199. Mikerov M, Michielsen K, Moriakov N, Sechopoulos I. Non-rigid motion compensation for breast CT. In: *Proceedings of the 2022 IEEE Nuclear Science Symposium and Medical Imaging Conference (NSS/MIC)*; 2022; Italy. IEEE; 2022:1-2. doi:10.1109/NSS/MIC44845.2022.10399275

200. Goris LC, Mikerov M, Pautasso JJ, Sechopoulos I. In-line spectroscopy for iodine quantification in dynamic contrast-enhanced dedicated breast CT. *Med Phys*. 2025;52(2):1037-1044. doi:10.1002/mp.17497

201. Guo L, Kong D, Liu J, et al. Breast cancer heterogeneity and its implication in personalized precision therapy. *Exp Hematol Oncol*. 2023;12(1):3. doi:10.1186/s40164-022-00363-1

202. Santos JM, Wright GA, Pauly JM. Flexible real-time magnetic resonance imaging framework. In: *Proceedings of the 26th Annual International Conference of the IEEE Engineering in Medicine and Biology Society*; 2004; San Francisco, CA. IEEE; 2004:1048-1051. doi:10.1109/IEMBS.2004.1403343

203. Keenan KE, Ainslie M, Barker AJ, et al. Quantitative magnetic resonance imaging phantoms: A review and the need for a system phantom. *Magn Reson Med*. 2018;79(1):48-61. doi:10.1002/mrm.26982

204. Mikerov M, Pautasso JJ, Goris L, Michielsen K, Sechopoulos I. 4D Dynamic contrast-enhanced breast CT: Phantom-based reconstruction parameter optimization for iodine quantification. *Med Phys*. 2025;52(4):2212-2223. doi:10.1002/mp.17658

205. Jong RA, Yaffe MJ, Skarpathiotakis M, et al. Contrast-enhanced digital mammography: initial clinical experience. *Radiology*. 2003;228(3):842-850. doi:10.1148/radiol.2283020961

206. Hill ML, Mainprize JG, Yaffe MJ. System calibration for quantitative contrast-enhanced digital breast tomosynthesis (CEDBT). In: Tingberg A, Lång K, Timberg P, eds. *Breast Imaging*. Lecture Notes in Computer Science. Vol 9699. Springer; 2016:669-676. doi:10.1007/978-3-319-41546-8_80

207. Leithner R, Knogler T, Homolka P. Development and production of a prototype iodine contrast phantom for CEDEM. *Phys Med Biol*. 2013;58(3):N25-N35. doi:10.1088/0031-9155/58/3/N25

208. Hu YH, Scaduto DA, Zhao W. Optimization of clinical protocols for contrast-enhanced breast imaging. In: *Proceedings of SPIE: Medical Imaging 2013: Physics of Medical Imaging*. Vol 8668. SPIE; 2013:86680G. doi:10.1117/12.2008028

209. Skarpathiotakis M, Yaffe MJ, Bloomquist AK, et al. Development of contrast digital mammography. *Med Phys*. 2002;29(10):2419-2426. doi:10.1118/1.1510128

210. Hill ML, Mainprize JG, Mawdsley GE, Yaffe MJ. A solid iodinated phantom material for use in tomographic x-ray imaging. *Med Phys*. 2009;36(10):4409-4420. doi:10.1118/1.3213516

211. Hasse FC, Giannakis A, Wehrse E, et al. Improvement of Breast Cancer Detection Using Dual-Layer Spectral CT. *Diagnostics (Basel)*. 2024;14(14):1560. doi:10.3390/diagnostics14141560

212. Chen L, Xiao Z, Fu J, Huang J, Lan Y. The diagnostic performance of dual-layer spectral detector CT for distinguishing breast cancer biomarker expression and molecular subtypes. *Sci Rep*. 2024;14(1):1500. doi:10.1038/s41598-024-51285-3

213. Huang SY, Boone JM, Yang K, Kwan AL, Packard NJ. The effect of skin thickness determined using breast CT on mammographic dosimetry. *Med Phys*. 2008;35(4):1199-1206. doi:10.1118/1.2841938

214. Saito M. Dual-energy approach to contrast-enhanced mammography using the balanced filter method: spectral optimization and preliminary phantom measurement. *Med Phys*. 2007;34(11):4236-4246. doi:10.1118/1.2790841

215. Goris LC, Gouma S, Pautasso JJ, Michielsen K, Sechopoulos I. Modular breast and tumor perfusion phantoms for 4D dynamic contrast-enhanced dedicated breast CT. *Med Phys*. 2025;52(10):e70004. doi:10.1002/mp.70004

216. Pacheco G, Pautasso JJ, Michielsen K, Sechopoulos I. Software article: a generalized cascaded linear system model implementation for x-ray detectors. *Med Phys*. 2025;52(9):e18079. doi:10.1002/mp.18079

217. Chen X, Benveniste H, Tannenbaum AR. Unbalanced regularized optimal mass transport with applications to fluid flows in the brain. *Sci Rep*. 2024;14(1):1111. doi:10.1038/s41598-023-50874-y

218. Nassi M. *Generative 3D Breast Shape Modeling and Deep Learning for X-ray Scatter Correction in Dedicated Breast CT: Towards 4D Dynamic Contrast-Enhanced Breast CT Imaging*. MS thesis. Politecnico di Torino; 2023.

219. Gao Y, Ventura-Diaz S, Wang X, et al. An explainable longitudinal multi-modal fusion model for predicting neoadjuvant therapy response in women with breast cancer. *Nat Commun*. 2024;15(1):9613. doi:10.1038/s41467-024-53450-8

Summary

This thesis presents the technical development and experimental validation of four-dimensional dynamic contrast-enhanced breast computed tomography (4D DCE-bCT) as an imaging modality for breast cancer assessment, with the goal of supporting personalized treatment strategies. The limitations of current imaging methods, particularly in evaluating tumor response to neoadjuvant chemotherapy, underscore the need for alternatives that combine high spatial and temporal resolution with quantitative accuracy.

Chapter 2 introduces a deep learning-based scatter correction method trained on Monte Carlo-simulated data. The approach improves image uniformity and signal fidelity, enabling more reliable tissue characterization.

Chapter 3 compares first- and second-generation bCT systems. The newer system shows improved resolution, better detection of fine details, and reduced radiation dose, enhancing its suitability for diagnostic and monitoring applications.

Chapter 4 details the implementation of a cascaded systems model for spectral optimization. This model identifies acquisition settings that enhance iodine contrast visibility, thereby improving functional imaging and contrast quantification.

Chapter 5 describes the optimization of reconstruction parameters using a combination of IMPACT and PICCS algorithms. The method supports low-dose acquisition while maintaining accurate iodine concentration measurements over time, enabling evaluation of tumor perfusion dynamics without substantially increasing patient risk.

Chapter 6 presents the experimental validation of the proposed 4D DCE-bCT protocol using a dynamic perfusion phantom. The results confirm the accuracy and temporal consistency of iodine concentration measurements, demonstrating the feasibility of the approach for functional imaging under realistic acquisition conditions.

This work advances 4D DCE-bCT toward clinical application by addressing core technical challenges. Its capacity for quantitative, high-resolution functional imaging may support more accurate response monitoring and individualized treatment planning in breast cancer care.

Samenvatting

Deze thesis beschrijft de technische ontwikkeling en experimentele validatie van vierdimensionale dynamisch contrast versterkte borstcomputertomografie (4D DCE-bCT) als beeldvormingstechniek voor de beoordeling van borstkanker, met als doel gepersonaliseerde behandelstrategieën te ondersteunen. De beperkingen van bestaande beeldvormingstechnieken, met name bij het evalueren van de tumorrespons op neoadjuvante chemotherapie, benadrukken de noodzaak van alternatieven die een hoge ruimtelijke en temporele resolutie combineren met kwantitatieve nauwkeurigheid.

Hoofdstuk 2 introduceert een op deep learning gebaseerde methode voor strooistralingscorrectie, getraind op Monte Carlo-gesimuleerde gegevens. Deze aanpak verbetert de beelduniformiteit en signaalgetrouwheid, waardoor een betrouwbaardere weefselkarakterisering mogelijk wordt.

Hoofdstuk 3 vergelijkt eerste- en tweede-generatie bCT-systemen. Het nieuwere systeem toont verbeterde resolutie, betere detectie van fijne details en een lagere stralingsdosis, wat de geschiktheid vergroot voor diagnostische en monitoringstoepassingen.

Hoofdstuk 4 beschrijft de implementatie van een cascaded-systeem model voor spectrale optimalisatie. Dit model identificeert acquisitie-instellingen die de zichtbaarheid van jodiumcontrast verbeteren en draagt zo bij aan een betere functionele beeldvorming en contrastkwantificatie.

Hoofdstuk 5 behandelt de optimalisatie van reconstructieparameters met behulp van een combinatie van de IMPACT- en PICCS-algoritmen. De methode ondersteunt acquisitie bij lage dosis terwijl de nauwkeurigheid van jodiumconcentratiemeting in de tijd behouden blijft, waardoor evaluatie van tumorperfusiedynamiek mogelijk is zonder het risico voor de patiënt aanzienlijk te verhogen.

Hoofdstuk 6 presenteert de experimentele validatie van het voorgestelde 4D DCE-bCT-protocol met behulp van een dynamisch perfusiephantoom. De resultaten bevestigen de nauwkeurigheid en temporele consistentie van de jodiumconcentratiemetingen en tonen de haalbaarheid van de methode aan voor functionele beeldvorming onder realistische acquisitieomstandigheden.

Dit werk brengt 4D DCE-bCT dichter bij klinische toepassing door fundamentele technische uitdagingen aan te pakken. De mogelijkheid tot kwantitatieve, functionele beeldvorming met hoge resolutie kan bijdragen aan een nauwkeurigere responsmonitoring en geïndividualiseerde behandelplanning bij borstkanker.

Appendix

Research Data Management
List of Publications
PhD Portfolio
Curriculum Vitae
Acknowledgments

Research Data Management

Ethical Considerations and Privacy

This thesis includes data acquired through original experiments and simulations, as well as limited data from anonymized patients and patient-based digital phantoms. All procedures involving patient data were approved by the appropriate medical ethics committee and conducted in accordance with applicable guidelines and regulations.

Data Sources and Storage

The majority of the data used in this work was collected or generated by the author. This includes experimental breast CT scans acquired at Radboudumc, synthetic datasets created using patient-based digital phantoms, and simulation outputs produced for model development and validation. All data were securely stored on institutional servers, following Radboudumc's policies for data integrity and access control. Where necessary, data transfers to and from collaborators were covered by appropriate data transfer agreements.

Accessibility and Availability

To support reproducibility and transparency, selected datasets and accompanying metadata have been deposited in the Radboud Data Repository. These can be accessed via the following DOIs:

- Chapter 2: https://doi.org/10.34973/swg6-xy60
- Chapter 3: https://doi.org/10.34973/75cs-7r75
- Chapter 4: https://doi.org/10.34973/0q6g-mb22
- Chapter 5: https://doi.org/10.34973/4ptk-ez10

Due to the inclusion of limited patient data and sensitive imaging details, full access may be subject to restrictions as outlined in the repository documentation.

Documentation and Reusability

All datasets were organized with structured folder hierarchies and documented using readme files and parameter descriptions. Imaging data were stored in standardized formats (e.g., TIFF, CSV or HDF5), and simulation data were exported in interoperable formats compatible with common analysis tools. Where relevant, analysis scripts and configuration files were included to allow for reuse or reproduction of the presented results.

List of Publications

Peer-reviewed articles

Pautasso JJ, Caballo M, Mikerov M, Boone JM, Michielsen K, Sechopoulos I. Deep learning for x-ray scatter correction in dedicated breast CT. *Med Phys.* 2023;50(4):2022-2036. doi:10.1002/mp.16185.

Pautasso JJ, Michielsen K, Sechopoulos I. Technical note: Characterization, validation, and spectral optimization of a dedicated breast CT system for contrast-enhanced imaging. *Med Phys.* 2024;51(5):3322-3333. doi:10.1002/mp.17069.

Pautasso JJ, Van Speybroeck CDE, Michielsen K, Sechopoulos I. Comparative image quality and dosimetric performance of two generations of dedicated breast CT systems. *Med Phys.* 2025;52(4):2191-2200. doi:10.1002/mp.17623.

Pautasso JJ, Mikerov M, Goris L, Michielsen K, Sechopoulos I. 4D dynamic contrast-enhanced breast CT: Phantom-based reconstruction parameter optimization for iodine quantification. *Med Phys.* 2025;52(4):2212-2223. doi:10.1002/mp.17658.

Goris LC, Mikerov M, **Pautasso JJ**, Sechopoulos I. In-line spectroscopy for iodine quantification in dynamic contrast-enhanced dedicated breast CT. *Med Phys.* 2025;52(2):1037-1044. doi:10.1002/mp.17497.

Mikerov M, Michielsen K, Moriakov N, **Pautasso JJ**, et al. Empirical motion-artifact reduction for nonrigid motion in dedicated breast CT. *IEEE Trans Biomed Eng.* 2025;72(10):3133-3145. doi:10.1109/TBME.2025.3562610.

Pacheco G, **Pautasso JJ**, Michielsen K, Sechopoulos I. A generalized cascaded linear system model implementation for x-ray detectors. *Med Phys.* 2025;52(9):e18079. doi:10.1002/mp.18079.

Goris LC, Gouma S, **Pautasso JJ**, Michielsen K, Sechopoulos I. Modular breast and tumor perfusion phantoms for 4D dynamic contrast-enhanced dedicated breast CT. Med Phys. 2025;52(10):e70004. doi:10.1002/mp.70004.

Contributions to conferences

Pautasso, J. J., Michielsen, K., & Sechopoulos, I. (2021). *Task-based filter optimization for a dual-energy breast CT system*. *European Congress of Medical Physics.* Abstract published in *Physica Medica: European Journal of Medical Physics,* 92(Suppl), S225.

Pautasso, J. J., Caballo, M., Michielsen, K., & Sechopoulos, I. (2021). *Deep learning model for scatter correction in dedicated breast CT*. In *AAPM 63rd Annual Meeting & Exhibition*, Vol. 48. Wiley.

Sarno, A., Mettivier, G., Michielsen, K., **Pautasso, J. J.**, Sechopoulos, I., & Russo, P. (2022). *Noise and spatial resolution characteristics of a clinical computed tomography scanner dedicated to the breast*. In *16th International Workshop on Breast Imaging (IWBI2022)* (Vol. 12286, pp. 297–304). SPIE.

Sarno, A., Mettivier, G., Michielsen, K., **Pautasso, J. J.**, Sechopoulos, I., & Russo, P. (2022). *Empirical detector model for simulated breast exams with a dedicated breast CT scanner*. In *IWBI2022* (Vol. 12286, pp. 23–28). SPIE.

Pautasso, J. J., Caballo, M., Mikerov, M., Michielsen, K., & Sechopoulos, I. (2022). *X-ray scatter correction in breast CT images using deep learning*. In *ECR 2022*. European Congress of Radiology.

Pautasso, J. J., Tunissen, S. A. M., Michielsen, K., & Sechopoulos, I. (2023). *Cascaded linear system-based model for simulation and optimization of a dedicated breast CT system*. In *ECR 2023*. European Congress of Radiology.

Nassi, M., Michielsen, K., Sechopoulos, I., & **Pautasso, J. J.** (2024). *Generation of an unlimited number of uncompressed digital breast phantoms from breast CT images*. In *ECR 2024*. European Congress of Radiology.

Goris, L., **Pautasso, J. J.**, Mikerov, M., Michielsen, K., & Sechopoulos, I. (2024). *Phantom setup for the optimization of dynamic contrast-enhanced breast CT: iodine contrast curves in a simplified breast phantom*. In *ECR 2024*. European Congress of Radiology.

Pacheco, G., **Pautasso, J. J.**, Michielsen, K., & Sechopoulos, I. (2024). *CASYMIR: A generalized cascaded linear system model implementation for X-ray detectors*. In *Medical Imaging 2024: Physics of Medical Imaging* (Vol. 12925, pp. 45–48). SPIE.

Pautasso, J. J., Mikerov, M., Goris, L., Michielsen, K., & Sechopoulos, I. (2024, May). *4D dynamic contrast-enhanced breast CT: evaluation of quantitative accuracy*. In *IWBI 2024* (Vol. 13174, pp. 208–212). SPIE.

Nassi, M., Michielsen, K., Sechopoulos, I., & **Pautasso, J. J.** (2024). *Generation of digital breast phantoms with patient-based internal structures from breast CT images*. In *VITM 2024*. Virtual Imaging Trials in Medicine.

Goris, L., Gouma, S., **Pautasso, J. J.**, Michielsen, K., & Sechopoulos, I. (2025). *Modular breast and tumor perfusion phantoms for validation of 4D dynamic contrast-enhanced dedicated breast CT*. In *Medical Imaging 2025: Physics of Medical Imaging*. SPIE.

Tomal, A., Michielsen, K., **Pautasso, J. J.**, & Sechopoulos, I. (2025). *Monte Carlo simulation of photon-counting breast CT system: from implementation to image quality evaluation*. In *Medical Imaging 2025: Physics of Medical Imaging*. SPIE.

PhD portfolio of Juan José Pautasso

Department: Imaging

PhD period: 01/06/2020 – 15/12/2025

PhD Supervisors: Prof. Dr. I. Sechopoulos

Dr. R.M. Mann

PhD Co-supervisor: Dr. K.J.M. Michielsen

Training activities	Hours
Courses	
• RIHS - Introduction course for PhD candidates (2020)	15.00
• RU - Project management for PhD candidates (2021)	52.00
• Radboudumc - Scientific integrity (2021)	20.00
• Machine Learning (2022)	60.00
• RU - Statistics for PhD's by using SPSS (2022)	60.00
• Geant4 (2023)	20.00
• Geant4 advanced (2023)	20.00
Seminars	
• RIHS PhD retreat (2022)	16.00
• Radboud Data Repository (2025)	2.00
Conferences	
• European Congress of Medical Physics (2021, Poster)	24.00
• AAPM 63rd Annual Meeting & Exhibition (2021, Poster)	32.00
• AI in Cancer Diagnosis (2021)	16.00
• European Congress of Radiology 2022 (2022, Poster)	40.00
• International Workshop on Breast Imaging 2022 (2022, Poster)	40.00
• European Congress of Radiology 2023 (2023, Oral)	40.00
• Cancer Research Retreat (2023, Poster)	36.00
• International Workshop on Breast Imaging 2024 (2024, Oral)	40.00
Other	
• Weekly AXTI Research Meeting (2025)	200.00
• Weekly Research Meeting (2025)	200.00
• Monthly Breast Impact Meeting (2025)	50.00
TEACHING ACTIVITIES	
Lecturing	
• Breast CT for radiographers (2023)	2.00
• Biomedical imaging: seeing is understanding (BMS23) (2024)	5.00
• Fysica voor Klinisch Fysici (2025)	10.00
Supervision	
• Supervision of Master Student (2023)	50.00
• Co-supervision of Bachelor Thesis (2024)	20.00
• Co-supervision of Master Thesis (2025)	30.00
TOTAL	**1100.00**

About the author

Juan José Pautasso was born on July 29, 1992, in San Basilio, Córdoba, Argentina. In 2012, he earned a bachelor's degree in Mechatronics from the National Technological University in Córdoba, and in 2017 he earned a Bachelor of Engineering in Biomedical Engineering from the National University of Córdoba.

In September 2018, he pursued and earned a Master of Science in Biomedical Engineering from the Polytechnic University of Madrid. His master's thesis, titled *Design and Development of a Novel Pipeline for Resting-State Functional Magnetic Resonance Imaging Processing*, was conducted at the Spanish National Center for Cardiovascular Research (CNIC) and focused on neuroimaging and data processing techniques.

In June 2020, he joined the Advanced X-ray Tomographic Imaging (AXTI) group as a PhD candidate in the Department of Imaging at Radboud University Medical Center in Nijmegen. His research, supervised by Koen Michielsen, Ritse Mann, and Ioannis Sechopoulos, focuses on the development of a novel 4D breast imaging modality, aiming to provide functional imaging capabilities for personalized breast cancer treatment.

Acknowledgments

In October 2019, I returned to Argentina after completing a master's degree in Madrid, where my family warmly welcomed me back. I believe life rarely offers certainties, and most things are in constant change. Still, knowing they will always be there whenever I return makes it easier to dream big and go abroad to explore the world. That sense of comfort and safety keeps me moving forward.

To my mother, who taught me to advance with dedication, instilled in me a love for literature, and encouraged me to cherish the process. To my father, whose determination, perseverance, and commitment to seeing things through continue to inspire me.

To my grandparents and godparents, for their support. To my siblings and Joaquín, for always offering a shoulder to lean on and a place to stay. To my niece Olivia and nephew Bastian, for showing me how to love, even from afar. You are my foundation, and I love you all.

In February 2020, I learned that I would start my PhD at the AXTI lab in June. The idea of moving from my hometown, San Basilio, to the Netherlands felt like a distant dream, but my childhood friends supported me and encouraged me. I love and miss you all every day: Favio, Andi, Carlin, Javi, Giuli, Pulp, Joa, Bechu, Gabi, Fredy, and Fran. Thank you for always being there for me.

I had planned to travel in May, but COVID-19 and Argentina's total lockdown made it impossible. When the Dutch embassy finally contacted me, the journey truly began. Getting to Buenos Aires was no small feat. Sofi arranged transportation, and Ele kindly offered her apartment when all accommodations were closed. Rochi greeted me at 4 a.m. with Ele's apartment keys. A few weeks later, my visa was ready.

Traveling during the pandemic was an adventure in itself. At every stop, I had to present permits to travel and negative tests, hoping for no last-minute complications. Each moment was filled with adrenaline. To Romi, Sofi, Peter, Pablo, Maurito, Barbi, Vir, Eze, Tincho, Lau, Rochi, and Ele, thank you for your kindness and generosity. I could not have done it without you.

Once in the Netherlands, Rodri met me at Schiphol and helped me reach Nijmegen. Melisa and Ema gave me the keys to Sofi's apartment. Soon after, I moved into

my new place, arranged by Marjolein. A few weeks later, Ioannis welcomed me to Radboudumc, marking the start of my PhD journey.

This journey taught me that scientific progress is never linear, but moves in bursts, with periods of growth and reflection. There are no shortcuts, only patience and persistence. In the end, it seems an inner game, more about understanding than knowledge. Like personal growth, science unfolded best for me in its own time, even though reality often tries to hurry it along.

We cannot always control our goals, as external factors often play a role. But we can choose how we navigate the path. One of the most valuable lessons I learned during my PhD is how to break down complex problems into manageable steps. That skill will stay with me far beyond research.

Ioannis, thank you for your guidance and for helping me grow. You taught me to approach challenges with purpose and to strive for quality in everything we do. The opportunity you gave me truly changed my life. I carry with me all the conversations we had and am grateful for your support both at work and beyond. Gracias, Jefe!

Koen, I truly enjoyed those moments when we worked out why something was not working, and watching the very first 4D DCE-bCT sequence on loop. Since one of your favorite sayings is 'I would have written a shorter letter, but I did not have the time,' I will keep it brief: thank you for always making the effort to make things work.

Ritse, thank you for being part of this journey. Based on your published work, I imagine breast MRI remains your favorite, but I am grateful for your generosity toward the developed modality and for your insightful contributions. I like to think that breast CT has earned a small place in your heart as well.

A good supervisor is essential for navigating a PhD. Finding good mentors is almost like running a successful experiment on the first try. It is rare, incredibly satisfying, and hard not to talk about. Dear reader, if you consider this thesis a success, give them credit. If not, blame them anyway. They are strong enough to handle it.

Beyond the academic milestones, this PhD journey was deeply shaped by my colleagues, who shared the ups and downs, the long coding and writing days, the coffee breaks, and the countless walks that made the experience not only bearable but truly memorable.

Marta, thank you for always counting on me and including me in your plans, which were usually great ones (epa, é sério!?). It was very nice to be part of your wedding, and even more special to witness the chaotic yet beautiful moments you and Miguel have created together.

Sjoerd, my very first Dutch friend. Honestly, that should be a line on my CV. Thank you for all the deep talks during our endless walks and long workdays. I still laugh every time I tell people about the morning when we somehow decided, mid-joke, to sign up for the Vierdaagse. An unforgettable experience. And thank you, and Sophie too, for letting me be part of your life, jokes and all.

Jessie, it was a pleasure to share so many hours with you at the office and at conferences. Every time I opened the door and saw you at your desk, I knew the day would be all right. Calm and steady, you were a kind of Brabant Buddha. Thank you for always being there.

Luuk, when I started at AXTI, I had no idea you were both Iron-ing Man and ready to fly like Superman. On top of that, you were a great PhD colleague, even if I always called you 'professor'. Thank you for sharing both knowledge and laughs.

Sarah, what a pleasure it has been to be your colleague and friend. We danced through parties and conferences. I hope I will never forget that life talk in your mom's car on the way to the AXTI weekend, the one with the banana peel in the glove compartment. Thank you for all the moments and for inviting me to share them with you and your people. I wish you and Olaf all the best, and I know you will succeed in whatever you pursue.

Martina, I still vividly remember our very first interview. Supervising your master's thesis was one of the highlights of my PhD and one of the best decisions I made. I have enjoyed seeing your growth, and I am proud of you not only as an colleague but also as a friend. Thank you very much for the opportunity.

Leo, even before I start writing, a smile appears on my face as so many anecdotes come to mind. It is amazing to think that the first time we met, you had only a yellow backpack and a very yellow suitcase. Now you have built a full life here with Luis. I hope we do not end up in another Dutch course, we have had too many already. Thank you for being such a good friend and for always offering me your shoulder when I needed it.

Marjolein, when I was still in Argentina, I kept asking myself who was this kind person who answered all my emails with such care and organized everything so efficiently. Later, I found myself sitting next to you in your car on the way to AXTI activities, watching F1 with you and Yuri, and having nice talks. Thank you for being such a good friend.

Gustavo, I still remember meeting you at that conference in Leuven. We had no idea life would later bring us together to face one of the most intricate challenges of our time: organizing the lab at -1. It was a battle, but we made it. I wish you all the very best and many more hours of sleep.

Joana, thank you for being so generous from the very beginning of my time at the lab. Music and books were always reasons for us to talk, and it has been a joy to be your friend. I enjoyed pestering you as much as needed, and sometimes a little more, right up until the Portuguese came out and I knew I should stop.

Daan, you were always the one looking out for the group and trying to keep our collective PhD experience enjoyable. I genuinely appreciate it and will carry those lessons with me, along with the image of the sharpest-dressed postdoc I have ever met.

Jim, funny to think we have probably shared more hours outside the office than at work, and easily a few liters of wine. I look forward to the rematch at *Ticket to Ride* and many more dinners with you and Melina.

Mikhail, from arriving in the Netherlands during a pandemic to cycling through Germany and the Netherlands, we have certainly had a long PhD journey. I wish you the best in whatever comes next!

Liselot, the queen of iodine. Thank you for always being ready to dive into yet another experiment (I honestly lost count somewhere around number 57), for pushing our images to publication-worthy perfection, and for all the good talks in between. Working with you truly enhanced my PhD in every sense. It has been a real pleasure, and I am very grateful for it.

Noemi, working with you definitely sharpened my night vision skills, thanks to all those times the lights were off for your radiology work. You joined our team and, quite literally, multiplied. Big hugs to you and your kids, and thank you for the talks in Spanish and the good times.

Hanne, thank you for being my mentor in Dutch words and for sharing your surprisingly impressive frisbee skills. When I think of our time at the office, I can still hear your laughter. I am really glad we shared that time. Thank you for being part of it.

Lian, what a battle it was to get the paperwork right. Thank you for your commitment to the project and for making it happen. In two weeks, we will definitely have more news. No doubt about that.

Maranda, Stevensloop, Dutch sayings, pursuing a PhD, few parties, the Vierdaagse, quite the adventure, hè? And as the Dutch say, 'met twee vingers in de neus.' We both know it was far from that. Honestly, I am glad it was not. Thank you for all the good moments.

Noelia, every time you visited the lab, it felt like an old friend coming home. Our time together was short but filled with dinners, runs, talks and plenty of laughter. I have truly enjoyed sharing this chapter with you. Let's find an excuse to meet again soon, preferably somewhere with good food and no Monte Carlo simulations.

Wendelien, when I started at AXTI, I heard stories about the woman who would pause meetings to drive a tractor and help her family. I was not sure what to expect, but I was happy to discover that behind those stories was a warm and generous person, always ready to help and organize whatever was needed. It has been a real pleasure to be your colleague and to witness your journey.

Raneim, I hope that at the end of your PhD, you will look back on all your hard work with pride. You should. Sometimes, the outcome does not reflect the journey, and no paragraph can capture the weight of the effort behind it. I am glad we got to share this part of the road.

Olga, thank you for your friendship and for always knowing exactly what to say, whether it was a piece of deep Polish wisdom or a perfectly timed dark joke. I have always admired your intense energy. From living like royalty in a hotel during the pandemic to conquering Harvard, you always manage to reach exactly where you want to be.

Franziska, some time ago I shared with you a page from *Letters to a Young Poet* because it reminded me of your patience with life's unfolding. Rilke's words speak of trust, of carrying the questions, and of creating from inner necessity. I hope they continue to resonate with you in moments of uncertainty. I am grateful that we shared this part of the journey.

Marco, our time working together at the office felt short. I sometimes wonder what more I could have learned if we had continued working closely. I am grateful for the time we shared and for everything you taught me. I wish you all the very best.

Alma, we spent more time together outside the office than during working hours, but it was time well spent. Thank you for being part of the journey.

Pim, I could always tell you were in the office by the sound of your keyboard. It could probably be classified as heavy artillery. I will miss the familiar soundtrack of your typing, the good company along the way, and your generosity in sharing knowledge about good programming practices.

Sven, it was great to witness your growth at work and how you became increasingly confident in the steps you are taking. I admire your courage because you made that very hard decision when you needed to. That says more about you than anything else. I am happy to have met you. Thank you for the good moments.

Ou, I was impressed when I saw the paths you explored in China. I hope you will have plenty of time to chase more adventures. And I hope finding parking in the Netherlands for your 4×4 truck will not be one of them. Thank you for sharing these stories.

To those who made my time abroad easier, thank you.

Carlota and Rodri, thank you for always opening your home to me and making me feel truly welcome every time. I really appreciate every moment we have shared together.

Luchi, Ani, Juanjo, and Flori, it is a gift knowing I can find you anywhere in the world. You are the best thing Madrid gave me, and I love seeing how we have grown. Here is to more memories, wherever life takes us.

Cufa, Eze, Diego and Angie, thank you for helping me to keep the spark of inventiveness burning bright.

Sofi, it was amazing to find you in Nijmegen without even planning it. I am grateful for your friendship over all these years. I love those mornings when I found you preparing your mate at the coffee corner, or when I was preparing mine and you appeared, and we shared a few together like good Argentinians. You were always

ready to share a great meal and guide me in the kitchen as my cooking mentor. Every time we talk, Argentina feels a little closer.

To Mili, Mariano, Juanma, Ana, Sancho, Nacho, Nicky, Meli, Ema, and Pau, thank you for making me feel like I had a piece of Argentina right here with me.

To Anneloes, thank you for being a beautiful serendipity in my life, for your support, the laughter, the conversations, the trips, and for always encouraging me. Thank you for welcoming me into your life, your family, and your friends. You invited me in and made me feel like one of your own. I love you very much.

I believe community is the thread that weaves our lives together. It shapes our well-being through shared values, rituals, and deep connections. Sometimes it is a steady presence when everything feels impossibly difficult. Other times, it lingers quietly in the background. But it is always there, grounding us through change and lifting us in times of need. I am proud of what this journey became.

Thank you all, for being part of it.

Los abrazo.
With gratitude,
JP

Radboudumc
university medical center
IN DEI NOMINE FELICITER
Radboud University